Some Studies on the Use of Curvelet and Wavelet Transforms for Medical Image Processing

Thesis submitted by

Manas Saha

Doctor of Philosophy (Engineering)

Department of Electronics and Telecommunication Engineering

Faculty Council of Engineering & Technology

Jadavpur University

Kolkata, India

2016

JADAVPUR UNIVERSITY
KOLKATA-700 032, INDIA

INDEX NO. 278/12/E

1. Title of the Thesis:

Some Studies on the Use of Curvelet and Wavelet Transforms for Medical Image Processing

2. Name, Designation & Institution of the Supervisor/s:

Prof. M. K. Naskar
Professor
Department of Electronics and Telecommunication Engineering
Jadavpur University
Kolkata-700 032

Prof. Biswa Nath Chatterji
Professor
Dean (Academic Affairs)
B. P. Poddar Institute of Management and Technology
Poddar Vihar, V. I. P Road,
Kolkata- 700 052

3. List of Publications:

International Conferences

1] M. Saha, M. K. Naskar, B. N. Chatterji, "Poisson Noise Removal from Mammogram Using Poisson Unbiased Risk Estimation Technique," in Proceedings of the Second International Conference on Information Systems Design and Intelligent Applications- 2015 (INDIA 2015), Kalyani, West Bengal, 8-9 January 2015, vol. 2, pp. 327-335, DOI 10.1007/978-81-322-2247-7_34

2] M. Saha, M. K. Naskar, B. N. Chatterji, "Mammogram denoising by curvelet transform based on the information of neighbouring coefficients," in Proceedings of the 2015 Third International Conference on Computer, Communication, Control and Information Technology (C3IT), Hoogly, West Bengal, 7-8 February 2015, pp.1-6. Also available at IEEE Xplore Digital Library, DOI 10.1109/C3IT.2015.7060180

3] M. Saha, M. K. Naskar, B. N. Chatterji, "Detection of Diabetic Retinopathy Using the Wavelet Transform and Feedforward Neural Network" in Proceedings of the 2nd

International Doctoral Symposium on Applied Computation And Security Systems, Vol. 1, pp. 101-109, Kolkata, 23-25 May 2015, DOI:10.1007/978-81-322-2650-5_7

4] M. Saha, M. K. Naskar, B. N. Chatterji, "Human Ringworm Detection using Wavelet Energy Signature," in Proceedings of the 2015 IEEE 2nd International Conference on Recent Trends in Information Systems (ReTIS), Jadavpur University, Kolkata, 9-11 July 2015, pp. 178-182. Also available at IEEE Xplore Digital Library, DOI 10.1109/ReTIS.2015.7232874

Journals

1] M. Saha, M. K. Naskar, B. N. Chatterji, "Soft, Hard and Block Thresholding Techniques for Denoising of Mammogram Images," IETE Journal of Research, vol.61, No.2, pp.186-191, February 2015, DOI: 10.1080/03772063.2015.1009394

2] M. Saha, M. K. Naskar, B. N. Chatterji, "Darier Disease – A Genetic Disorder Detection in the Light of Computer Vision," International Journal of Enhanced Research in Science, Technology & Engineering, Vol. 5, No. 2, pp. 149-155, February 2016

Book Chapter

1] M. Saha, M. K. Naskar, B. N. Chatterji, "Wavelet and Curvelet Transforms for Biomedical Image Processing," IGI Global (communicated and under review)

4. List of Patents

Nil

5. List of Presentations in National/International/Conferences/Workshops

1] "Poisson Noise Removal from Mammogram Using Poisson Unbiased Risk Estimation Technique," in Second International Conference on Information Systems Design and Intelligent Applications- 2015 (INDIA 2015), Kalyani, West Bengal, 8-9 January 2015.

2] "Mammogram denoising by curvelet transform based on the information of neighbouring coefficients," in 2015 Third International Conference on Computer, Communication, Control and Information Technology (C3IT), Hoogly, West Bengal, 7-8 February 2015.

3] "Detection of Diabetic Retinopathy Using the Wavelet Transform and Feedforward Neural Network," in 2nd International Doctoral Symposium on Applied Computation And Security Systems, Kolkata, 23-25 May 2015.

4] “Human Ringworm Detection using Wavelet Energy Signature,” in 2015 IEEE 2nd International Conference on Recent Trends in Information Systems (ReTIS), Jadavpur University, Kolkata, 9-11 July 2015.

CERTIFICATE FROM THE SUPERVISOR/S

This is to certify that the thesis entitled "Some Studies on the Use of Curvelet and Wavelet Transforms for Medical Image Processing" submitted by Shri Manas Saha, who got his name registered on 27th February 2012 for the award of Ph.D (Engg.) degree of Jadavpur University is absolutely based upon his own work under the supervision of Prof. M. K. Naskar and Prof. Biswa Nath Chatterji and that neither his thesis nor any part of the thesis has been submitted for any degree/diploma or any other academic award anywhere before.

1. _____

Prof M. K. Naskar

2. _____

Prof. Biswa Nath Chatterji

Dedicated to the lotus feet of holy mother, Sarada

Acknowledgements

I like to express heartfelt thanks to my teachers, Prof. M. K. Naskar and Prof. Biswa Nath Chatterji for guiding this research work. It is really very difficult to express their research contribution within a frame of few words. I am deeply obliged for their creativeness, motivation, accessibility and generosity. Prof. Naskar is one of the nicest persons that I have come across in life. The height of knowledge, wisdom and selflessness of Prof. Chatterji inspires me to follow him as a role model in life. I always wish their good health and prosperity.

I feel privileged to have friends like Rajarshi Middya of Jadavpur University, Dr. Sudipta Chattopadhyay of Mizoram University, Dr. Gautam Das of Siliguri Institute of Technology who helped me a lot during study period. I owe special thanks to Mr. Tapan Kumar Ghosh, Director, Techno India Group for the moral support that I got from the very first day of Ph.D registration.

I am really blessed to have loveable parents – Mr. Kamdeb Saha and Mrs. Maya Saha, brother – Mr. Tapash Saha and sister – Mrs. Tanusri Bagchi Saha for the education and culture they imparted me. My sincere gratitude goes to Mrs. Kyamelia Roy for her constant support and encouragement to complete the thesis.

Jadavpur University Manas Saha

October 2016

Abstract

Over the last few decades there is a rapid development in the field of medical image processing. Scientists and engineers all over the world have developed advanced diagnostic tools to detect the diseases at any level of complicacy. Keeping pace with fast and accurate diagnosis, this thesis aims at exploring the use of two multiresolution mathematical transforms called wavelet and curvelet in medical image processing. A survey on fifteen different advanced wavelets including curvelet is performed. The two transforms (wavelet and curvelet) are comprehensively studied and selected as the medical image analyzing tools. The different investigating areas of this thesis are the detection of human skin ringworm, Darier disease detection, diabetic retinopathy (DR) detection and denoising of mammogram. Three different approaches on denoising of mammogram are presented in this thesis.

The human skin ringworm is investigated in the light of computer vision. Two independent methodologies are developed for its detection. The first methodology implements three level multi-wavelet decomposition of the skin images and subsequent evaluation of the approximation and detail subband energies which act as the texture characterizing features. The second methodology incorporates the curvelet to segment the circular protrusion of the skin images especially associated with ringworm images followed by statistical texture investigation. After feature extraction by both the methodologies, binary classifier called the support vector machine (SVM) recognizes the images as ringworm with detection accuracy of around 87% and 80% for the first and second methodologies respectively. In addition, the performance indexing parameters obtained from SVM classification like sensitivity, specificity, Positive Predictive Value (PPV) and Negative Predictive Value (NPV) are evaluated. Both the methodologies are comprehensively demonstrated and compared to select the better one. The selected method is then compared with the available techniques and commented upon.

This thesis also deals with the detection of a genetic disorder called Darier disease manifested as dermal changes. It incorporates three methodologies. They are - 1) gray level co-occurrence matrix (GLCM), 2) local binary pattern (LBP) and 3) wavelet energy feature for skin texture recognition. The feedforward neural network (FNN) is implemented for Darier disease detection. All the methodologies are thoroughly compared to find the most suitable one as skin texture screening tool. The GLCM, LBP and wavelet based methodologies attain Darier disease detection accuracy of about 82%, 82% and 89% respectively. Though the GLCM based methodology provides inferior detection accuracy than wavelet based methodology, but it addresses the presence and location of typical skin textural abnormalities.

The early detection of DR and its subsequent medication is of prime importance to the medical practitioners. This thesis focuses on the implementation of the curvelet transform to segment the blood vessels from the retina images. The blood vessel characterizing features of curvelet filtered images are quantified by the retinal image analyzer. The computed vessel features of DR and non-diabetic retinopathy (NDR) images are used to tabulate databases which are provided to a FNN for DR detection. The DR is detected with sensitivity of 83.9%, specificity of 77.4% and accuracy of 80.6% which is better than the results obtained by other researchers.

Mammogram is an easy and affordable means of diagnosis of breast cancer. Like other medical data acquisitions, it is also commonly affected by noise. Therefore it is a challenge for the researchers to denoise the mammograms for clear data extraction. This thesis targets at denoising of mammogram by wavelet and curvelet transforms with a focus to investigate the role of an “embedded” thresholding algorithm. As the thresholding technique helps to compress the transform generated coefficients, an effort is made to find how the change of the thresholding algorithm coded within either the wavelet/curvelet transform produces different signal to noise ratio (SNR) of the denoised image. The scientific exploration also goals at finding the dependence of SNR of the output image on the type and depth of the noise. A standard mammogram is selected and different types of noise are added. Next, the noisy mammogram is denoised by the wavelet and the curvelet transforms. The commonly used thresholding techniques called hard, soft and block are implemented for noise reduction. Finally, a comparison table is drawn to find the applicability of the transforms with the incorporated thresholding algorithms.

Generally a mammogram is denoised by curvelet transform based on conventional thresholding called hard thresholding (HT). Therefore, the motive of this investigation is to denoise mammogram with the same transform but with efficient thresholding technique. This thresholding technique is based on the information of the neighbouring curvelet coefficients which are generated after the application of fast discrete curvelet transform. It is also known as block thresholding. It is found that the curvelet transform applied with three different block thresholding techniques is visually and statistically better than the conventional approach.

It has also been found that the denoising performance of wavelet, contourlet and curvelet implemented on mammogram with Poisson noise is unique in the sense that SNR of denoised mammogram by wavelet is better than that of by contourlet which in turn is better than that of by curvelet. The first part of this investigation deals with the confirmation of the above exceptional denoising performance (trend) with the result obtained by our approach. The later part of our investigation implements the recently developed denoising approach called the Poisson Unbiased Risk Estimation–Linear Expansion of Thresholds (PURE-LET) to the Poisson noise corrupted mammogram with an objective to improve the SNR. The PURE-LET successfully removes Poisson noise in a way better than the traditional mathematical transforms mentioned above.

Contents

List of Figures

List of Tables

List of Abbreviations

ANN	Artificial Neural Network
ARIA	Automated Retinal Image Analyzer
BCT	Block Complex Thresholding
BO	Biorthogonal
CAD	Computer Aided Diagnosis
CBIR	Content Based Image Retrieval
CF	Coiflet
CT	Computer Tomography
DALR	Diameter to Length Ratio of Vessel Segment
DB	Daubechies
DCT	Diagonal Complex Thresholding
DFB	Directional Filter Bank
DM	Discrete Meyer
DR	Diabetic Retinopathy
DRT	Diagonal Real Thresholding
DT-CWT	Dual-Tree Complex Wavelet Transform
FDCT	Fast Discrete Curvelet Transform
FNN	Feedforward Neural Network
GLCM	Gray Level Co-occurrence Matrix

HT	Hard Thresholding
IUWT	Isotropic Undecimated Wavelet Transform
kNN	k-nearest neighbor
L	Length of Vessel Segment
LBP	Local Binary Pattern
LOOCV	Leave-one-out Cross Validation
LP	Laplacian Pyramid
LSGR	Local Seed Region Growing
MDA	Mean Diameter
MNDA	Minimum Diameter
MRI	Magnetic Resonance Imaging
MSE	Mean Square Error
MXDA	Maximum Diameter
NDA	Number of Selected diameter
NDR	Non-diabetic Retinopathy
NPV	Negative Predictive Value
PET	Positron Emission Tomography
PPV	Positive Predictive Value
PURE-LET	Poisson Unbiased Risk Estimation Technique – Linear Expansion of Thresholds
RBVF	Retinal Blood Vessel Features
SDA	Standard Deviation of Diameter
SNR	Signal to Noise Ratio
SURE	Stein's Unbiased Risk Estimate
SVM	Support Vector Machine
SY	Symlet
TOR	Tortuosity

USFFT	Unequally Spaced Fast Fourier Transform
2D-DWT	Two Dimensional Discrete Wavelet Transform
2D FFT	Two Dimension Fast Fourier transform
5FCV	5 Fold Cross Validation
10FCV	10 Fold Cross Validation

Chapter 1

Introduction

1.1 Background

The efficient feature extraction and representation have always been a great challenge to the researchers of image processing. There has been a long way of development of Fourier transform, discrete Fourier transform, fast Fourier transform, short time Fourier transform to the wavelet transform. The basis functions of the Fourier transform are sinusoids. But wavelet transforms are based on small waves called wavelets which have varying frequency and fixed duration. This allows them to present the equivalent of a musical score of an image, enlightening not only what notes (frequencies) to play but also when to play. In contrary, Fourier transform provides only the frequency information of a signal. It does not provide the temporal information of the frequency components present in a signal. So far, innumerable applications of wavelet have been proposed on image coding, image compression, image denoising, image segmentation, content based image retrieval (CBIR), etc. But traditional wavelet is good at representing only the point singularities (discontinuities) of images. It neither considers the geometric properties of structures nor exploit the regularity of edges. So wavelet based image applications as mentioned above become computationally inefficient for geometric features having line-like or curve singularities.

1.2 From Classical Wavelet Transform to Advanced Wavelet Transforms

The limitation of the 2-D separable wavelet in representing images with smooth curves can be clearly understood by the famous example of two painters – "wavelet" style painter and "X-let" (henceforth X-let stands for advanced wavelet) style painter mentioned by Do *et al.* [22] and Do [23].

Suppose we want to represent the leaf edge shown in Figure 1.1 by the two style painters mentioned above. The "wavelet" style painter is limited to the use of brush stroke of only square shape along a given curve as illustrated in Figure 1.2 (a). The limitation of "wavelet" style painter gradually becomes prominent with the increase of resolution from coarse (red) to fine (blue) and even to finer as pictured in Figure 1.2 (a). As resolution is increased, the wavelet style painter requires more number of squares than X-let style painter shown in Figure 1.2 (b) to represent a given curve. This painting phenomenon is analogous to the generation of more number of discrete wavelet coefficients than discrete X-let coefficients. So wavelet based curve representation is not sparse (optimum) as X-let. Therefore, X-lets are often efficient than wavelets in representing the images with smooth curves.

In this context, Do *et al.* [22] had also pointed out the "wish list" for representing an image faithfully. The five features of his "wish list" are multiresolution, localization, critical sampling, directionality, anisotropy. The first three are addressed by the wavelet transform while the last two remain unaddressed.

Figure 1.1 Flower image with focus on leaf edge for representation [127].

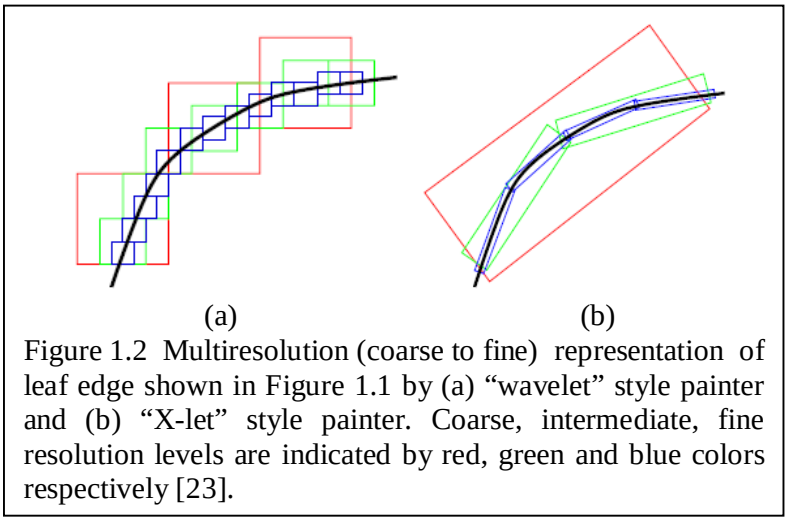

(a) (b)

Figure 1.2 Multiresolution (coarse to fine) representation of leaf edge shown in Figure 1.1 by (a) "wavelet" style painter and (b) "X-let" style painter. Coarse, intermediate, fine resolution levels are indicated by red, green and blue colors respectively [23].

Thus, the example of the two painters along with the proposed "wish list" [22] motivated the researchers to develop X-lets like curvelet, contourlet, ranklet etc. for optimal image representation.

1.3 Literature Survey

Here classification of X-let into 15 "lets" is presented in Figure 1.3 and discussed one by one with their applications. A very limited survey of some of the aspects of X-let is available (vide [93], [98]). Hence, we thought that a survey of X-lets will be useful to the research workers of signal and image processing.

1.3.1 Ridgelet Transform

Though the wavelet transform is a very promising tool for sparse representation of objects with point singularities but its efficiency is greatly challenged by the objects with line singularities. Therefore, ridgelet transform was developed by Candes and Donoho in 1999 to break the limitation of the wavelet transform in higher dimensions [11, 12]. The ridgelet analysis is related to the theory of approximation by the superposition of ridge functions mentioned by Candes *et al.* [12]. This proposal is not new and it dates back to 1970's suggesting alternatives of standard methods of multivariate approximation. Later on during 1980's this theory of superposition of the ridge functions became popular in the name of single-hidden–layer feedforward neural network (FNN) where the consideration of the m-term approximation is mentioned [12]. The theory of ridgelet analysis gives a stable and

constructive method to provide theoretical insights to objects antecedently unavailable.

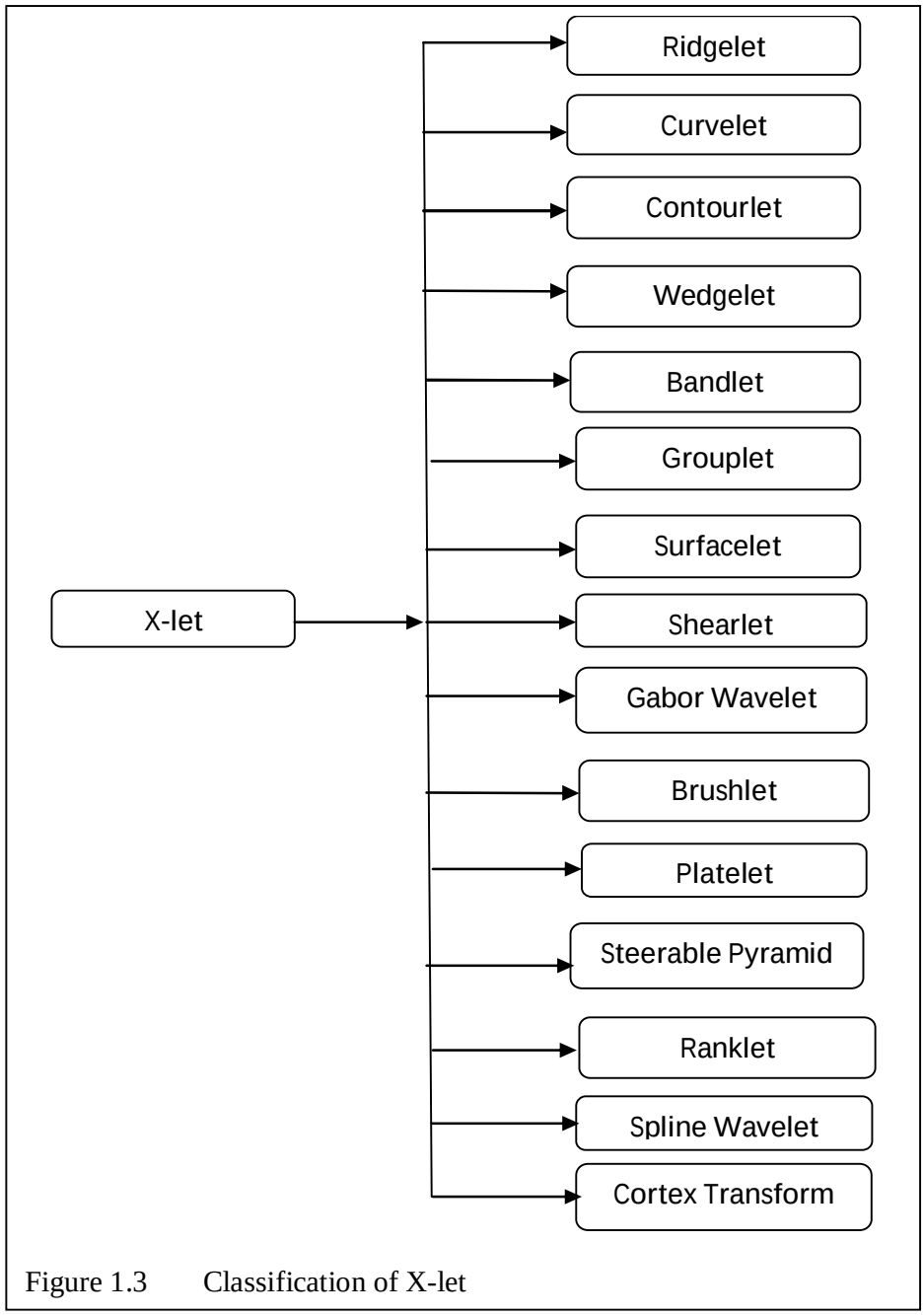

Figure 1.3 Classification of X-let

Reviewing the fundamentals and the flowgraph of the ridgelet transform demonstrated by Starck *et al.* [129], it can be concluded that the ridgelet transform can resolve the problem of sparse representation of smooth objects with straight edges. But in practice the edges of the images are typically curved instead of being straight and

ridgelet alone fails to yield satisfactory representation. Therefore, to represent curve edges one should consider the image at sufficiently fine scale where curve edge becomes almost straight. One can then capture a curve edge by applying ridgelet transform locally [24].

Another important feature of ridgelet support is its constant length but variable width. This limits the variability of its anisotropy. On the other hand, curvelet support has both variable length and variable width to give a higher degree of anisotropy especially suited for curvy images.

The ridgelet transform finds many applications in image processing like image representation, image denoising, image compression, space weather monitoring, characterization of nanostructures and pattern recognition.

1.3.2 Curvelet Transform

The curvelet transform was pioneered by Candes and Donoho [13, 14] as a new multiscale directional transform. In two dimensions (2-D), this transform provides nearly optimal sparse representation of objects having singularities along smooth curves. The first generation curvelet [13] was developed in the continuous domain by multiscale filtering and "embedded" ridgelet transform. One can find the flowgraph of the curvelet transform in [129]. The close relation of the two transforms, i.e., the first generation curvelet transform and the ridgelet transform is shown in Figure 1.4.

Unfortunately, the redundancy and the slow computation of the first generation curvelet motivated its founders to develop the second generation curvelet transform [14, 15]. The essence of the second generation is that it is directly determined by the frequency plane partitioning technique without the use of the ridgelet transform; thereby making it a more robust and faster image analysis tool.

The several applications of the curvelet transform are image denoising, color and contrast enhancement, image restoration, image compression, image fusion, CBIR, remote sensing, fluid turbulence analysis, pattern recognition, solving of partial differential equations, medical image processing and so on. A review of contemporary curvelet applications is presented by Ma *et al.* [93].

1.3.3 Contourlet Transform

Using the perception mentioned in Section 1.3.2, Do and Vetterli [22] proposed a double filter bank based transform called the contourlet transform for

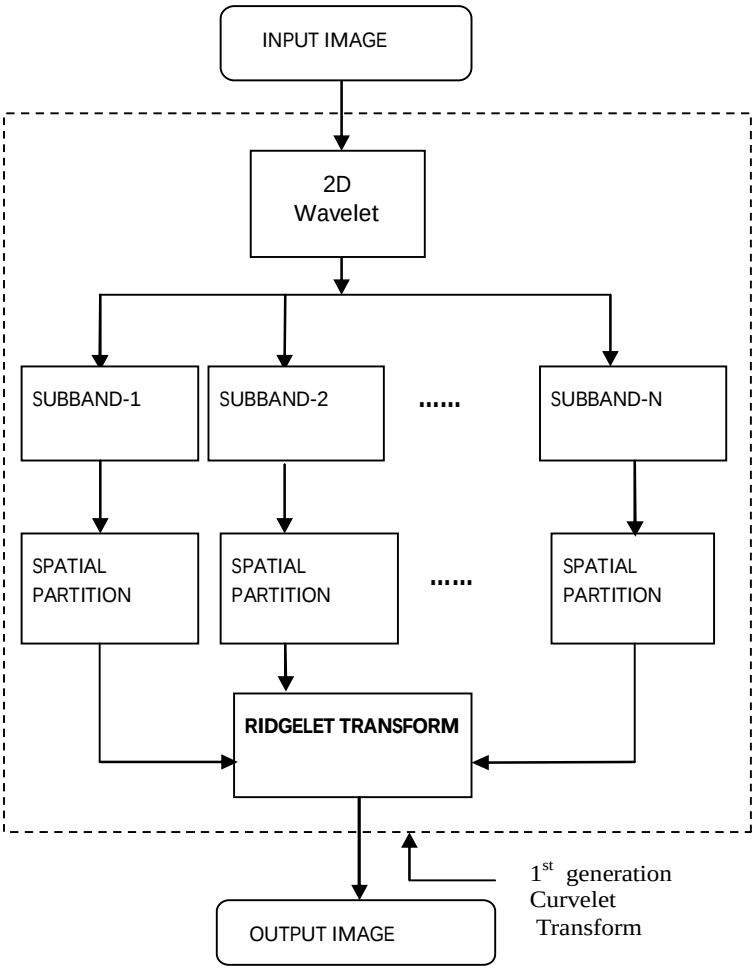

Figure 1.4 Block diagram representation of the first generation curvelet transform with "embedded" ridgelet transform.

obtaining sparse representation of images. It provides a variable multiresolution and directional decomposition of images. In the pyramidal filter bank [22], the first stage is the multiscale decomposition by the Laplacian Pyramid (LP) which is followed by a directional decomposition by 2-D directional filter bank (DFB). The LP captures the point discontinuities and DFB helps to link the point discontinuities into linear structure or contour segments.

The contourlet transform bears several novel features which help it to grow as a distinct and almost independent X-let. Though it closely resembles curvelet to attain the common goal of highly defined image representation but the fundamental difference is that the contourlet kernel functions are different for different directions instead of being found by the rotation of a single function in curvelet transform.

The efficient filter bank and low redundancy make the contourlet transform a popular computational framework for image processing. But Lu *et al.* [88] found that the major drawback of this transform is that its basis images are not localized in the frequency domain. As a solution, they suggested the replacement of LP by a new multiscale decomposition defined in frequency domain. As a result the basis images are sharply localized in the frequency domain, displaying smoothness along their main ridges in the spatial domain.

The applications of contourlet transform are image representation, image denoising, image compression, vehicle tracking, palm print recognition and so on.

1.3.4 Wedgelet, Bandlet and Grouplet Transforms

The importance of exploiting the geometry of complex edge structures was rightly pointed out by Mallat *et al.* [98]. A careful observation through the geometrically varying edges as shown in Figures 1.5 (a-f) reveals that the "shape" of an edge may vary from simple straight line (Figure 1.5 (a)) to very a complex geometry (Figure 1.5 (f)). The wedgelet, bandlet and grouplet have been addressed together in this section because they share a common goal of edge analysis. Instead of focusing them individually, their role and limitation in resolving the complex image boundaries with typical shapes and conditions have been discussed below. The relevant flowchart is given in Figure 1.6.

It is known that the curvelet transform attempts to exploit the geometrical regularity of an image. But its limitation is best explained by Yang *et al.* [143]. The geometrically regular functions can be described as a piecewise C^{α} (α times continuously differentiable) regular functions which are outside a set of regular edges. But the curvelet transform has the optimal image representation for only $\alpha = 2$. In practice, the images have irregular geometry with either $\alpha < 2$ or $\alpha > 2$ [143]. Therefore, when the question of regularity along the singularities of a surface arises,

the failure of the curvelet transform is overcome by a novel approximation scheme called the wedgelet [25]. The wedgelet divides the support of the image in dyadic adapted squares. But this approach is suitable for edges without blur and simple

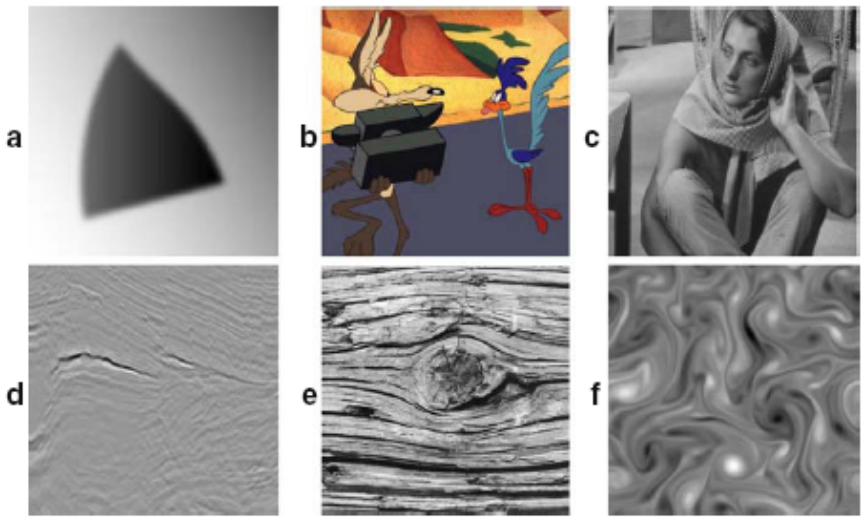

Figure 1.5 Image edges with different geometrical complexities, a) simple geometric image, b) cartoon image, c) natural mage, d) seismic image, e) texture of wood, f) vorticity field of a fluid [98].

geometry images. So the quest for finding the better X-let goes on and one such approximation based adaptive technique called the bandlet was introduced by Pennec and Mallat [110]. It can suitably capture the geometric regularity along the edges in an image by implementing an adaptive approximation of the image geometry when α is unknown and can fruitfully represent images because each bandlet atom is represented by a geometric flow showing the directions of regular variations of the gray level [143]. The geometry of the bandlet is suitable for analyzing geometrically regular images. But the key drawback of bandlet is that it cannot faithfully represent the complex geometry of textures as that of a wooden fibre.

The bandlet transform cannot draw the advantage of long range regularity of fine elongated structures like the texture of long hair. At this juncture, researchers came up with another novel approach called the Grouplet [99, 143]. The grouplet was developed on the basis of Gestalt theory [28]. The Gestalt theory suggests the recursive use of a set of grouping laws during the human perception of a natural scene

[98]. It helps to model the edges of images with long range of monotonic turbulent geometry as that of a wooden texture.

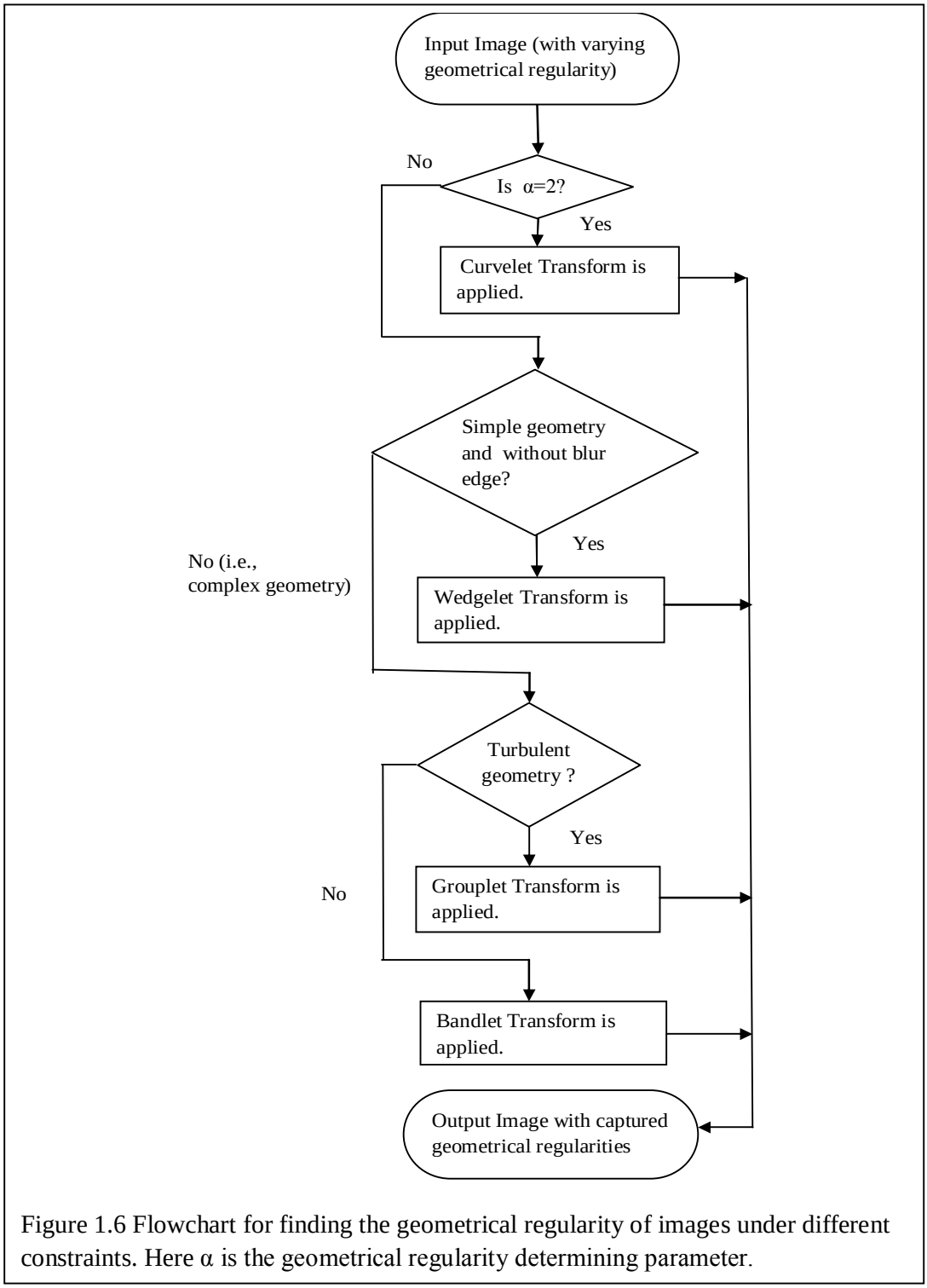

Figure 1.6 Flowchart for finding the geometrical regularity of images under different constraints. Here α is the geometrical regularity determining parameter.

The wedgelet transform is very much suitable for image enhancement. Bandlet can be used for image compression, image restoration and image denoising. The grouplet finds use in image denoising, texture analysis and image inpainting.

1.3.5 Surfacelet Transform

The DFB [6] was introduced by Bamberger and Smith in the year 1992. Do and Vetterli [22] suggested the combination of DFB and LP to formulate the contourlet transform, already discussed in Section 1.3.3. Lu and Do [89] proposed the extension of 2D DFB to higher dimensions resulting in a new type of filter bank called three dimensional (3-D) DFB which retains the wonderful capacity of directional decomposition of 3-D signals. The 3-D directional filter bank when combined with the LP gives rise to another new transform called the 3-D surfacelet or surface transform. It has the capacity to capture and represent the signal singularities located on smooth surfaces noticed in 3-D medical and video images. These signal singularities are often called surface singularities. The block diagram representation of the surfacelet transform is found in [90].

The surfacelet transform finds applications in numerous fields involving the processing of multidimensional volumetric data like seismic imaging, medical imaging and video clips. One interesting application of the surfacelet transform is the denoising of video signal which incorporates the motion selective subband decomposition of video signals.

1.3.6 Shearlet Transform

Shearlet introduced by Labate *et al*. [83] is a new class of multidimensional image representation tool. It is popular due to its ability to represent bivariate functions sparsely. So far various directional transforms like curvelets, contourlets, surfacelets have been demonstrated to resolve the edge representation of images. But none of these X-lets provides a unified treatment of both the continuous and digital setting [41]. This major drawback of these multiresolution methods is overcome by the shearlet due to its uniting capacity of the continuous and digital domain.

Shearlets are basically functions with orientation. The orientation of this function or waveform can be regulated by a parameter called shear parameter. These

can be obtained by using dilation, translation and shear transformation of a given function. The frequency support of this transform becomes much elongated with finer scale.

The applications of shearlet are sparse multidimensional representation of signal, adaptive multiresolution analysis of structures.

1.3.7 Gabor Wavelet Filter

In image processing, the octave based decomposition of the Fourier plane by the wavelet transform results in a poor angular resolution. But the wavelet packets can decompose the Fourier plane optimally at the cost of the four symmetric peaks in the frequency plane. Thus it is difficult to selectively tune and trace an unique frequency. Directionally oriented filter banks, steerable pyramid resolve the random partitioning of the Fourier plane. A Gabor filter [21, 76] resembles a wavelet filter bank where an individual filter produces an estimate of the local frequency content. This gabor filter is a local bandpass filter with joint localization of the spatial and frequency domain. The remarkable feature of gabor wavelet is that the Gabor basis is not only frequency tunable but also orientation selective. In practice many Gabor filters are often combined to form a filter bank covering the total frequency spectrum.

Gabor wavelet filters are widely used in computer vision, modeling of biological vision, estimation of head position, face recognition, iris identification, fingerprint matching and so on. It is also used for the classification of the facial expressions. This X-let also plays a significant role in texture classification of the images obtained from remote sensing and medical imaging.

1.3.8 Brushlet Transform

The computation load increases abruptly due to the convolution of the original image with so many filters of the bulky Gabor filter bank. Therefore, the search of better angular resolution motivated Meyer *et al.* [103] to expand the Fourier plane into windowed Fourier bases to develop a new X-let called Brushlet. This is a well localized complex valued function bearing a unique peak in frequency domain. As it is a complex valued function therefore it is associated with a phase which gives the knowledge about the orientation of the same. The size and locations of the brushlets

can be adaptively selected in order to obtain the most precise representation of an image in terms of oriented features with all possible directions and low computation load as compared to Gabor filters.

The brushlets are suitable for texture segmentation, directional image analysis and image compression. Another very promising application of the brushlet is the retrieval of color image using adaptive feature weight which is utilized in CBIR.

1.3.9 Platelet Transform

Willett and Nowak [141, 142] described platelet as the localized functions at different locations, scales and orientations which are capable of producing piecewise linear approximations of images containing smooth regions separated by smooth boundaries. It is well known that wavelets can be easily applied to Gaussian data for image analysis. But wavelets and even the members of the X-let family namely steerable pyramid [123], curvelet [13] cannot be applied to Poisson data; however Haar wavelet [80] is an exception. Platelet is well suited to handle Poisson data. The platelet is also better than the wedgelets in terms of image denoising and image reconstruction.

Platelet is a very promising tool for photon-limited medical imaging applications like Single Photon Emission Computed Tomography, Positron Emission Tomography, Confocal Microscopy and photon-limited astronomical imaging applications.

1.3.10 Steerable Pyramid Transform

A steerable pyramid [122] is a linear multi-scale, multi-orientation image representation transform where an image is decomposed into a number of subbands which are localized at various scales and orientations. The subbands are both translation and rotation invariant. One can see the structure of the steerable pyramid in [87]. One of the merits of steerable pyramid is the removal of aliasing effect of the orthogonal wavelets. Another interesting feature is the ease of invaluable design of steerable filters in quadrature pairs allowing adaptive control of both the phase and orientation [34]. There is also a choice to design the pyramid with random number of

orientation bands. The resulting demerit is an overcomplete transform by a factor of 4k/3 where k represents the number of orientation bands.

Applications of steerable pyramids are image denoising, texture classification, image fusion and face recognition.

1.3.11 Ranklet Transform

The ranklet transform is a novel orientation selective multiresolution transform. This was introduced in 2002 by F. Smeraldi for face detection [125]. Its non-parametric characteristic is due to the fact that this transform deals with the rank of pixel instead of its gray-level intensity. The ranklet transform of an image with N number of pixels is defined by the division of N pixels into two groups say, P and Q such that the pixel content of individual group is $P = Q = N/2$. Here the two groups are defined with the concept of the Haar Wavelet support which serves as the platform of the ranklet transform. The pictorial view of the Haar wavelet support can be seen in the work of Smeraldi [125]. The three sets of ranklet supports corresponding to the three types of Haar wavelet support namely vertical, horizontal, and diagonal are (R_v, S_v), (R_H, S_H), (R_D, S_D) respectively. The next step is the computation and normalization of the number of pixel pairs on the basis of greater pixel intensity as addressed by Angelini *et al.* [4]. This process is similarly followed for vertical, horizontal and diagonal directions.

The various applications of the ranklet transform range from texture classification, digital mammography, face detection, multispectral image classification, tracking points on distorted objects and so on. Earlier texture classification was done using texture anisotropy, Gabor filter and wavelet based filter. But later ranklet transform is used as a novel technique for texture classification.

1.3.12 Spline Wavelet

The spline wavelets were first reported by Schoenberg [120] in the year 1946. They can be thought as the connection of piecewise polynomials which are joined together by knots. The splines are regular functions which are either symmetric or anti-symmetric. These wavelets can be divided into four groups. They are orthogonal,

bi-orthogonal, semi-orthogonal and shift-orthogonal splines. The semi orthogonal spline also known as B-spline (the letter "B" probably stands for basis or basic according to the author, Unser [136]) wavelet was introduced by Schoenberg. The B-spline wavelets are very popular because they are tightly supported and act as the basic building block of the splines.

The spline wavelets also differ from the other wavelets in an unique way. The construction of the spline wavelets requires the specification of the polynomial splines instead of indirect specification of the scaling functions required for wavelet construction. This relieves the concern of the converging iterated banks of filter [137].

Splines are very much used in computer aided design, face recognition, image registration and image wrapping.

1.3.13 Cortex Transform

This is an old transform and it dates back to 1987. The cortex transform was pioneered by Goresnic *et al*. [37]. Here the input image is decomposed into a group of sub-images. The sub-images so formed not only change in orientation but also in resolution. The behavior of the visual cells of human being has been modeled in this transform. Basher *et al.* [8] had rightly pointed out that the cortex filter represents the bandpass nature of the visual cells. The Cortex filter is obtained by the multiplication of two Gaussian functions called the radial band filter and the orientation filter in the frequency domain. The frequency spectrum of the radial, orientation and cortex filters can be seen in [8].

The applications of the cortex transform may be enlisted as machine intelligence, texture classification, processing of modeled neural images, object identification in natural background.

1.4 Motivation

After discussing the 15 different X-lets, the major areas of their applications are pictorially represented in Figure 1.7. We are going to concentrate on medical image processing in this thesis. In image processing, the wavelet and curvelet have numerous applications. Despite scope of wavelet and curvelet transforms in medical image processing (discussed in Section 1.6), their applications are limited. So the

purpose of this investigation is to apply wavelet and curvelet transforms to certain medical images to detect the human diseases. It indirectly helps to develop

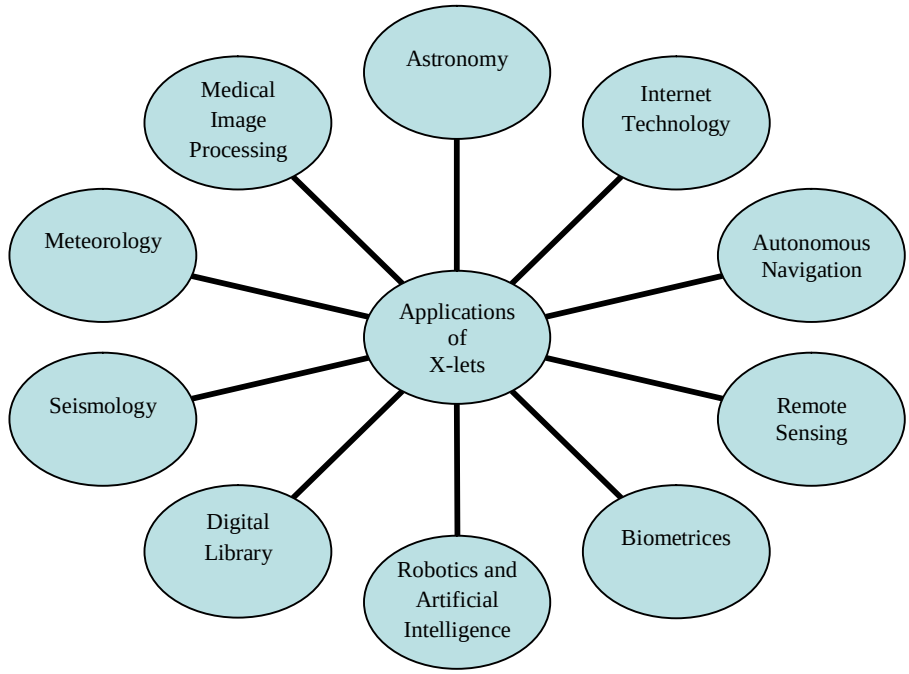

Figure 1.7 Some applications of X-let (advanced wavelet) in image processing.

sophisticated computer aided diagnosis/detection (CAD) system so that the doctors, medical personnel and ultimately the patients are benefitted.

In this thesis, wavelet and curvelet, a combination of a time tested tool and newly developed tools are selected for medical image processing. The wavelet is selected since it is a standard multiresolution mathematical transform which also provides a constant experimental guidance while working with the same and curvelet transform. The software is available in Matlab. In contrast to wavelet, curvelet is comparatively new with less available bio-medical applications. The software is also not readily available in Matlab. So wavelet transform inspires to go ahead with its firm grip in image processing and curvelet transform gives an opportunity to explore and compare its versatility with the former. Apart from wavelet and curvelet transforms, other transforms like contourlet, pure-let are also used in this thesis for medical imaging.

1.5 Some Typical Medical Imaging Modalities

Medical image processing is one of the important application areas of image processing. Over the last few decades there is a rapid development in this field. It deals with the quantitative analysis, enhancement and visual representation of the medical images of different parts, organs, tissues of a body which are captured for diagnostic and therapeutic purposes. The primary objective of this field is to assist the medical personnel with accurate and fast medical data processing so that the human diseases are detected easily and quickly. Some of the medical imaging modalities are 1) Gamma–ray imaging, 2) X-ray imaging, 3) Ultraviolet band imaging 4) Radio band imaging, 5) Ultrasound imaging. They are briefly outlined to develop an overall idea of medical image processing.

1.5.1 Gamma-ray Imaging

Gamma ray imaging is widely used in nuclear medicine. In nuclear imaging, a radioactive isotope is injected in a patient's body. The isotope emits radiation as it decays. The radiation is collected by a gamma ray detector to develop an image. Positron emission tomography (PET) is an example of gamma ray imaging. It is shown in Figure 1.8. The patient injected with radioactive isotope emits positron. When a positron meets an electron, they are annihilated and emit gamma rays.

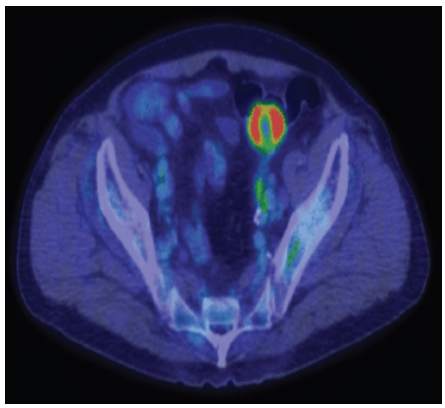

Figure 1.8 PET image showing sigmoid colon tumour [75].

1.5.2 X-ray Imaging

The X-ray imaging is a very old means of medical imaging technique. The X-rays are generated in a X-ray tube. The X-ray tube is a vacuum tube with cathode and anode located at the opposite ends. The cathode is heated to release free electrons. The electrons are accelerated with high speed and get collected at the positive anode. When electrons strike nucleus, radiation is generated in the form of X-rays. The different types of X-ray imaging are a) angiography, b) digital mammogram, c) computer tomography (CT) scan.

Angiography is a very popular method of obtaining images of blood vessels located at the retina, heart etc. This test is often followed before heart operations like angioplasty or by-pass surgery. Here a catheter which is a small, flexible and hollow tube is inserted into an artery or vein at the groin. The catheter is passed very delicately through the blood to the site of investigation. An X-ray contrast medium is injected through the hollow tube. This increases the contrast of the blood vessels. The radiologist notices any blockage or irregularities in the blood vessel. A coronary angiogram image is shown in Figure 1.9.

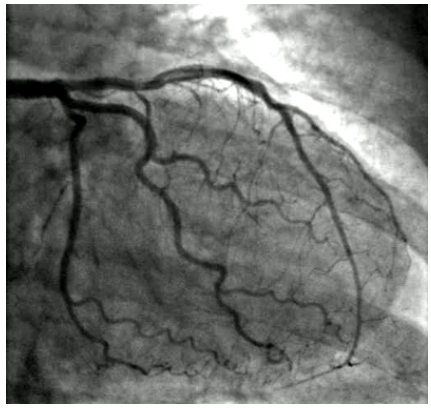

Figure 1.9 Coronary angiogram [72].

Digital mammography is a non-invasive, low energy X-ray imaging technique to detect breast cancer. A digital mammogram is shown in Figure 1.10. The breast is placed between two parallel plates; flattened and compressed to take the images. The

X-ray film is replaced by digital receptors and computers to investigate the breast tissues. It is an easy and economic mode of breast examination.

Computer tomography scan is a fast, non-invasive, painless and accurate X-ray imaging technique. The word “tomography” is derived from two Greek words, “tomos” and “graphe”. The word, “tomos” means “slice” or “section” and “graphe” means “drawing”. So it is a cross-sectional (“slice”) imaging (“drawing”) technique based on computer. It generates sliced images of human anatomy like the slices in a loaf of bread. One such CT scan image is provided in Figure 1.11.

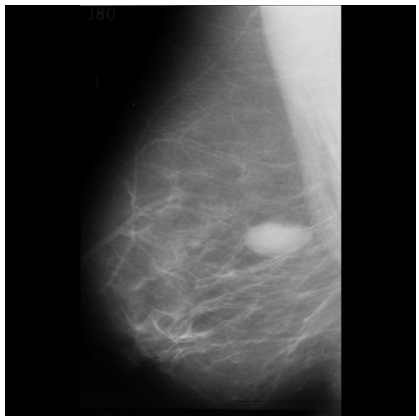

Figure 1.10 Digital mammogram [132].

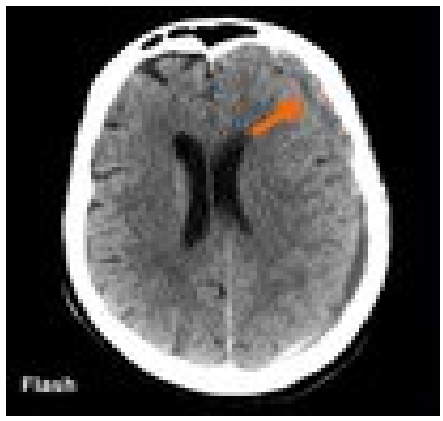

Figure 1.11 CT scan of human brain [64].

1.5.3 Ultraviolet Band Imaging

One of the fastest emerging areas of microscopy is the fluorescence microscopy. Fluorescence is the phenomenon where the material fluorspar fluoresces at the incidence of ultraviolet (UV) light. The UV light itself is invisible. When a photon of UV radiation collides with an atom of a fluorescent material, it elevates an electron to a higher energy level. When this electron transits from the higher to the lower energy level, it results in the emission of low energy photon in the visible (red) light region. The primary task of fluorescence microscope is to irradiate a prepared specimen with an excitement light. The weaker radiating fluorescent light is separated from the brighter excitation light. Thus only the emitted light reaches the eye. As a result, the fluorescing areas shine against dark background so that they can be easily detected. Pollen grain is a seasonal problem for people who suffer from allergenic reactions to the antigens embedded on the outer casing of these microscopic grains. The image presented in Figure 1.12 reveals green autofluorescence of tiny pollen grains visualized utilizing wide-field fluorescence microscopy.

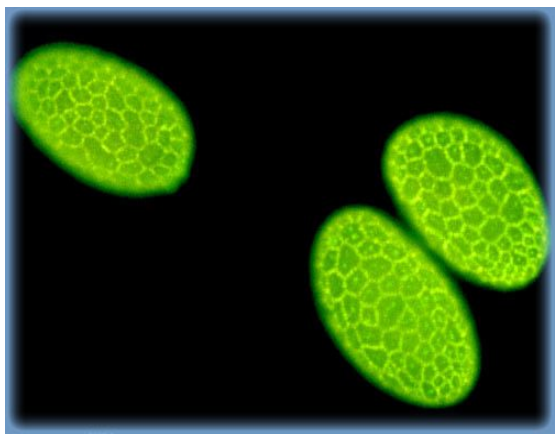

Figure 1.12 Pollen grain autofluorescence [70].

1.5.4 Ultrasound Imaging

Ultrasound imaging is a safe, non-invasive technique which produces images of the internal organs of a body with the help of high frequency sound waves. Using a transducer or probe, the sound wave is passed through the gel placed over the body to the interior of the body. The reflected sound wave is received to construct the image

of the body parts. It does not use any ionic radiation like X-ray. This technique also displays the structure and movement of the internal parts of human body. The blood flow through the vessels can also be monitored with this technique. An example of ultrasound imaging showing the development of foetus is pictured in Figure 1.13.

1.5.5 Magnetic Resonance Imaging

Magnetic resonance imaging (MRI) is a test which uses a magnetic field and radio waves for imaging. The radio waves are passed through the patient's body in short pulses. Each pulse produces a responding radio pulse which is emitted by the tissues of a particular organ of the body. The location and strength of the responding

Figure 1.13 Ultrasound image of foetus [49].

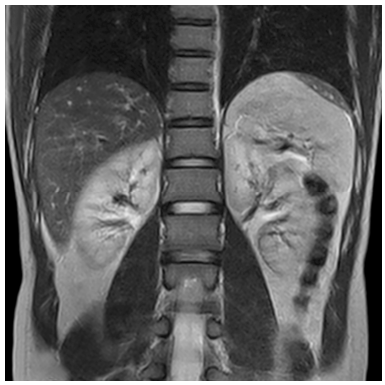

Figure 1.14 MRI scan of abdomen [65].

radio pulses are determined by a computer that generates a two dimensional image of the interested organ of the body. MRI often provides different information than other imaging modalities like X-ray and CT scan. For a MRI test, the selected part of the body is placed in a machine with a strong magnet. MRI scan result in digital images and are saved in computer. An example of a MRI scan is displayed in Figure 1.14.

Even now we find medical image processing is not much in use in the detection of human skin ringworm, darier disease, diabetic retinopathy and denoising of mammogram. Hence, effort is made to study these aspects.

1.6 Scope of the Thesis

The primary goal of the thesis is to investigate the applications of wavelet and curvelet transforms in some medical images. The investigation includes i) feature extraction of medical images, ii) feature analysis, iii) detection of various diseases like human skin ringworm, Darier disease, diabetic retinopathy (ophthalmic disease). The thesis also aims at denoising of mammograms with the help of various algorithms. Before implementing the transforms in medical imaging, they are reviewed. Their significance, developmental history, mathematical formulation, interrelationship, applications are studied as a broader perspective of this thesis. As wavelet transform is already a time tested transform with vast available literature, so it is briefly discussed at the beginning of Section 1.1. The different properties of wavelet transform are available in standard text books [Refer [36]: R. C. Gonzalez, R. E. Woods, Digital Image Processing, Pearson Education India, Second Edition 2002]. However a separate chapter–Chapter 2 is dedicated to the curvelet transform.
The major research contributions of this thesis are as follows:

- The thesis includes a survey of 15 X-lets.
- An intensive study on curvelet transform for applications in medical images for disease detection is performed in this research work. It focuses on different properties of curvelet transform, curvelet in continuous and discrete domain, fast curvelet transform and its mathematical interpretation.
- In this thesis, a common human skin disease called ringworm is detected with the help of two different methodologies. One methodology is based on wavelet

transform and the other is based on curvelet transform. Then a comparative study is done between them.

- This thesis also includes the method of detection of a genetic disease called Darier disease which gets expressed as dermal changes with the help of wavelet transform and other methods.
- In this thesis, curvelet transform is used to segment the non-linear blood vessels of the retina images. The blood vessels are examined by automated retina analyzer (a retina image analyzing software). And finally the diabetic retinopathy (DR) images are detected with the help of neural network.
- This thesis also presents a compendium of works on mammogram denoising using wavelet, curvelet and other related transforms. The transforms are based on different thresholding techniques applied for different types of noise.

1.7 Thesis Organization

Reviewing 15 X-lets at the beginning of the chapter, classical wavelet and nonclassical curvelet are selected as the implementing tools for medical image processing. A brief idea on medical image processing is presented. The different types of medical imaging techniques are also demonstrated with suitable images.

The rest part of the thesis is organized as below.

Chapter 2. The curvelet transform is comprehensively studied. The fundamentals of curvelet transform and its properties are introduced in this chapter. The curvelet transform in continuous time domain and discrete domain are systematically presented with mathematical background. Then the fast discrete curvelet transform based on two different approaches are exemplified with related algorithms.

Chapter 3. In this chapter, the common human skin disease called ringworm is investigated. Two independent methodologies are developed for its detection. The first methodology implements three level multi-wavelet decomposition of the skin images and subsequent evaluation of the approximation and detail sub-band energies

which act as the texture characterizing features. The second methodology incorporates the curvelet to segment the circular protrusion of the skin images especially with ringworms followed by statistical texture investigation. After feature extraction by both the methodologies, binary classifier called the support vector machine (SVM) recognizes the images as ringworm with detection accuracy of around 87% and 80% for the first and second methodologies respectively. In addition, the performance indexing parameters of SVM classification like sensitivity, specificity, Positive Predictive Value (PPV) and Negative Predictive Value (NPV) are evaluated. Both the methodologies are comprehensively demonstrated and compared to select the better one.

Chapter 4. This chapter deals with the detection of a genetic disorder called Darier disease manifested as dermal changes. The clinical diagnosis of the said disease motivates its recognition in the light of computer vision which incorporates three methodologies based on 1) gray level co-occurrence matrix (GLCM), 2) local binary pattern (LBP) and 3) wavelet energy feature for skin texture feature extraction. The FNN is implemented for Darier disease detection. All the methodologies are thoroughly compared to find the most suitable one as skin texture screening tool. The GLCM, LBP and wavelet based methodologies attain Darier disease detection accuracy of about 82%, 82% and 89% respectively. The other aspect of this work is that GLCM based methodology addresses the presence and location of several typical skin texture abnormalities by statistical plots.

Chapter 5. The early detection of diabetic retinopathy (DR) and its subsequent medication is of prime importance to the ophthalmologists. This chapter demonstrates the implementation of the curvelet transform to segment the retinal blood vessels. The vessel characterizing features of curvelet filtered images are quantified by the retinal image analyzer. The computed vessel features of DR and non-diabetic retinopathy (NDR) images are used to tabulate databases. The FNN is implemented to detect DR images with sensitivity of 83.9%, specificity of 77.4% and accuracy of 80.6% which is better than the previous works. Since our proposal is based on only three steps, it is simple, convenient and also easy to implement.

Chapter 6. Mammogram, a popular means of detecting breast cancer often gets affected by various types of noise during its acquisition. This chapter deals with the mammogram denoising. The total work is divided into three parts as i) Mammogram Denoising I, ii) Mammogram Denoising II, and iii) Mammogram Denoising III.

In Mammogram Denoising I, the mammogram is denoised by the wavelet and curvelet transforms which are based on soft, hard and block thresholding techniques. Then a comparative study is done between the wavelet and curvelet based mammogram denoising using the above mentioned thresholding techniques. In Mammogram Denoising II, curvelet transform based on three types of block thresholding are applied to noisy mammogram to find superior performance than traditional technique of hard thresholding. Mammogram Denoising III deals exclusively with Poisson noise filtration from mammogram by wavelet, curvelet, contourlet and pure-let transforms.

Chapter 7. A brief summary of the complete thesis is presented in this chapter. This chapter is dedicated to sum up the major contributions and findings of the thesis. The challenges of the complete work are highlighted. The probable future directions of this research work are enlightened. Lastly, the contribution of this research work to medical and scientific community is addressed.

Chapter 2

Curvelet Transform

2.1 Introduction

There are many image processing applications where images exhibit edges or discontinuities along curves. Such discontinuities are represented by Lagrangian or Eulerian representation [13]. A Lagrangian representation is constructed with complete knowledge of the edge curves. The representation adapts itself to the structure of edge curves. In contrast, Eulerian representation is non-adaptive. It is constructed once and for all types of discontinuities. It does nothing with the known or hypothesized details of underlying object. So it is quite natural to think that Lagrangian representation is more powerful than Eulerian one. In fact, many ongoing research works are based on the common belief that Lagrangian method of object discontinuity representation is simply the best [13]. In order to verify this common belief, the performance of object discontinuity representation by different schemes is quantified.

Suppose there is a smooth object supported in $[0,1]^2$. It has a discontinuity along a curve Γ. Then with the standard Fourier representation, and approximation having $\tilde{f}_m^F$ obtained from the best m nonzero Fourier terms, we get

$$\left\| f - \tilde{f}_m^F \right\|_2^2 \equiv m^{-1/2}, \qquad (2.1)$$

for $m \to \infty$.

Equation (2.1) is a slow rate of approximation. It is improved by wavelet representation. The approximant $\tilde{f}_m^W$ obtained from the best m nonzero wavelet coefficients satisfies

$$\left\| f - \tilde{f}_m^W \right\|_2^2 \equiv m^{-1}, \qquad (2.2)$$

for $m \to \infty$.

This fixed non-adaptive rate of approximation (Eulerian approach) is better than the rate of Fourier approximation.

Now we discuss below an approach which adapts to the object of interest. It provides superior approximate rate than non-adaptive approach. This adaptive approach selects terms from an overcomplete dictionary and is able to obtain

$$\left\| f - \tilde{f}_m^A \right\|_2^2 \equiv m^{-2}, \qquad (2.3)$$

for $m \to \infty$.

The result of adaptive representation given by Equation (2.3) is better than the rate of m-term approximation obtained from the fixed non-adaptive representation given by Equation (2.2).

But it is a matter of great surprise that the performance almost equivalent to Equation (2.3) can be attained by a non-adaptive scheme; thereby defying the traditional belief that Lagrangian approach of curve representation is always better than Eulerian approach. The non-adaptive scheme has a fixed and tight frame – a frame of curvelets (discussed below). It competes astonishingly well with the ideal adaptive rate given by Equation (2.3). Adding the m biggest terms present in the curvelet series, the m term approximation can achieve

$$\left\| f - \tilde{f}_m^C \right\|_2^2 \le C.m^{-2}(\log m)^3, \qquad (2.4)$$

for $m \to \infty$.

Equation (2.4) is almost as good as Equation (2.3) from asymptotic viewpoint.

In brief, the conventional concept of adaptive representation of curve edges (singularities) of an object being more powerful than fixed non-adaptive approach no longer remains valid. Instead, a new fixed non-adaptive representation is equally efficient as adaptive representation in the context of asymptotic m-term

approximation errors. This non-adaptive sparse representation of objects having edges is accomplished by the multiresolution mathematical transform called curvelet.

Curvelet is a two dimensional waveform. In two dimensions, the curvelet transform provides almost sparse representation of objects which have discontinuities along C^2 (twice differentiable) curves. It gives a new architecture for multiscale analysis. In spatial (planar) domain, a curvelet at scale j is an "oriented" needle. The effective support of the needle is a 2^{-j} by $2^{-j/2}$ rectangle. The needle shaped curvelet elements posses high directional sensitivity and anisotropy than isotropic wavelet elements [94] as pictured in Figure 2.1. On the contrary, in frequency domain, a curvelet at scale j is a "wedge" whose frequency support is also a rectangle but of size 2^j by $2^{j/2}$. Such a wedge is shown in Figure 2.3 and discussed in Section 2.3. The unique feature of curvelet is that the curvelet is not only localized in the spatial and frequency domains, but also in orientation.

There are two generations of curvelet transform. They are the first generation and the second generation curvelet transforms. The first generation curvelet transform is based on ridgelet transform which can represent the straight line like singularities very well. But absolute straight line singularities are rarely found in images. For example, let us consider an object, $f(x,y)$ with an edge as shown in Figure 2.2. When $f(x,y)$ undergoes subband filtering, it results in fine scale subband output images. Each subband output image, $\Delta_s f(x,y)$ retains a map of the original edge present in $f(x,y)$. The edge map is thickened to a width of 2^{-2s} depending upon the scale, s of the subband filter operator. Partitioning each susband into "squares" as shown in Figure 2.2, each square is isolated and renormalized. Each square is either empty or contains a line or a ridge segment. The ridge segments are then provided to the

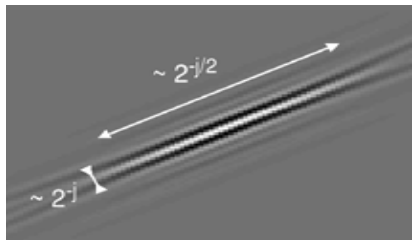

Figure 2.1 Needle shaped curvelet elements in spatial domain [58].

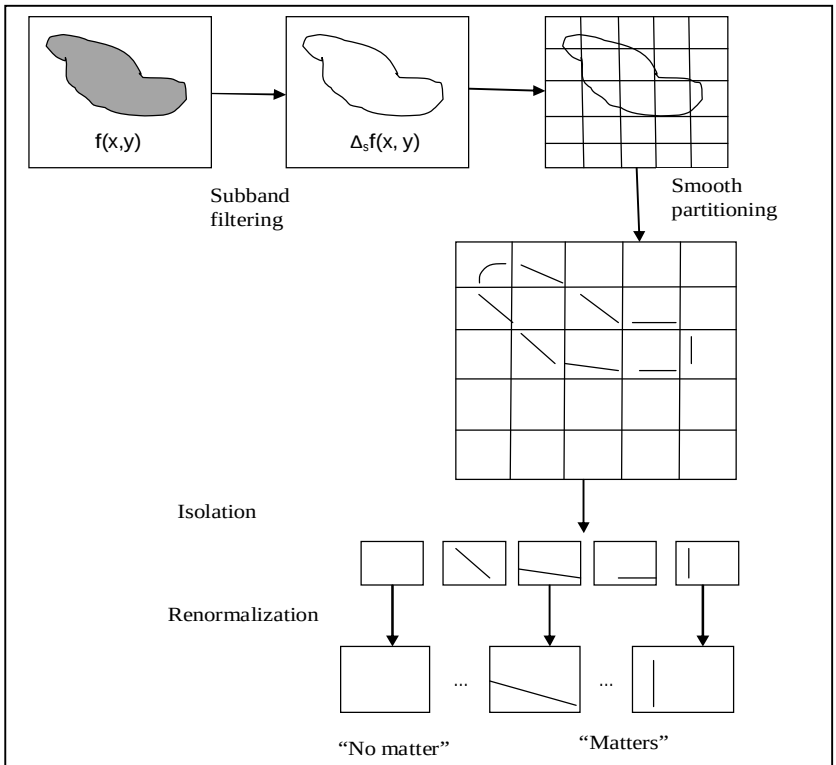

Figure 2.2 Subband decomposition of image, f(x,y) in spatial domain [24].

ridgelet transform for further computation and evaluation of curvelet coefficients. The first generation curvelet transform using ridgelet transform is unpopular because the ridgelet lacks a clear geometry due to the unavailability of true ridge functions. The computation speed is also low. This motivated the development of second generation curvelet transform using frequency partitioning technique which is discussed in Section 2.3.

Now, we build new tight frame of curvelet to address the difficulty of finding almost sparse representation of objects having discontinuities along C^2 edges. The tight frames are defined as follows. Let, μ denote the triple (j,l,k); where $j = 0,1,2...$ represents a scale parameter; $l = 0,1,.....2^j$ represents an orientation parameter; and $k = (k_1, k_2), k_1, k_2 \in Z$ represents a translational parameter. Now according to Candès et al. [14], the other parameters are introduced as

i) parabolic scaling matrix, D_j expressed as

$$D_j = \begin{pmatrix} 2^{2j} & 0 \\ 0 & 2^j \end{pmatrix} \tag{2.5}$$

ii) rotation angle

$$\theta_J = 2\pi . 2^{-j} . l \tag{2.6}$$

with J indexing the scale /angle pair $J = (j, l)$ and

iii) and translational parameter

$$k_\delta = (k_1 . \delta_1, k_2 . \delta_2) \tag{2.7}$$

where $\delta_1, \delta_2 \rangle 0$.

Using the above notations, curvelets are defined as functions of $x \in R^2$ by

$$\gamma_\mu (x) = 2^{3j/2} \gamma (D_j R_{\theta J} x - k_\delta) \tag{2.8}$$

The waveform γ is smooth and oscillatory along the horizontal direction. It is non-oscillatory along the vertical direction. So γ can be approximately considered as

$$\gamma (x_1, x_2) = \psi (x_1) . \varphi (x_2) \tag{2.9}$$

where ψ is a smooth wavelet and φ is a smooth scaling function. Therefore, curvelet frame elements are obtained by i) anisotropic dilation, ii) rotation and iii) translation of a group of unit scale oscillatory blobs from where we get some immediate properties of curvelet discussed in the next section. The profile φ and γ are selected so that $(\gamma_\mu)_\mu$ satisfies Parseval relation [14] given by

$$\sum_\mu \left| \langle f, \gamma_\mu \rangle \right|^2 = \| f \|^2_{L_2(R^2)}, \tag{2.10}$$

where $\forall f \in L_2 (R^2)$.

It can be said from the above equation, "that $(\gamma_\mu)_\mu$ is a tight frame and standard arguments give the reconstruction formula

$$f = \sum_\mu \langle f, \gamma_\mu \rangle \gamma_\mu \tag{2.11}$$

with equality holding in an L_2-sense" [14]. Thus, the above formula signifies that any square integrable function can be analyzed and synthesized as a superposition of curvelet elements.

2.2 Some Properties of Second Generation (Advanced) Curvelet Transform

2.2.1 Anisotropy Scaling Law

The parabolic scaling matrix already given by Equation (2.5) leads to anisotropy scaling law. The system is properly localized in space. It roughly obeys the following relations.

$$length \approx 2^{-j}, \tag{2.12}$$

$$width \approx 2^{-2j} \tag{2.13}$$

So the length and the width of a curvelet satisfy the anisotropy scaling law, i.e.,

$$width \approx length^2 \tag{2.14}$$

2.2.2 Directional Sensitivity

The curvelet elements are oriented along $\theta_J = \pi.l.2^{-j}$. According to Candès [14], "Identifying the curvelet width 2^{-2j} with the scale, there are 2^j directions at scale 2^{-2j}; that is

$$\#orientations = 1/\sqrt{scale}\ ." \tag{2.15}$$

2.2.3 Spatial Localization

For a known scale and orientation, curvelet is obtained by two dimensional translations. With the help of these translations a Cartesian grid is formed. The spacing of the grid is proportional to the length along the direction θ_J and width in the normal direction.

2.2.4 Oscillatory Nature

Curvelet elements exhibit oscillations across the "ridges" (straight line edges). Just like wavelet theory, coarse scale elements are of the form

$$\varphi_{k_1,k_2}(x) = \varphi(x - k_\delta), \quad \text{for } k_1, k_2 \in Z. \tag{2.16}$$

That means "coarse scale curvelets are translates of a waveform $\varphi(x_1, x_2)$" [4].

2.3 Continuous Time Curvelet Transform as a Mathematical Foundation for Discrete Curvelet Transform

In two dimensions, that is $(\mathbf{R}^2)$, let the spatial and frequency domain variables be represented by x and ω respectively. As frequency domain variable ω is a complex quantity, so it is convenient to analyze complex variable in polar coordinates. The polar coordinates are represented by r and θ. Two windows given by $W(r)$ and $V(t)$ are introduced and termed as "radial window" and "angular window" respectively [16]. The windows are smooth, positive and real valued. $W(r)$ takes positive real arguments while $V(t)$ takes only real arguments. In addition, $W(r)$ and $V(t)$ are supported on $r \in (1/2, 2)$ and $t \in [-1,1]$ respectively. The windows always satisfy the admissibility conditions [14]:

$$\sum_{j=-\infty}^{\infty} W^2(2^j r) = 1 \quad \text{for } r \in (3/4, 3/2) \tag{2.17}$$

and

$$\sum_{l=-\infty}^{\infty} V^2(t-1) = 1 \quad \text{for } t \in (-1/2, 1/2) \tag{2.18}$$

Now for each $j \geq j_0$, a frequency window $U_j(r,\theta)$ is introduced.

In frequency domain, $U_j(r,\theta)$ is defined as

$$U_j(r,\theta) = 2^{-3j/4} W(2^{-j} r) V\left(\frac{2^{\lfloor j/2 \rfloor}\theta}{2\pi}\right) \tag{2.19}$$

where $\lfloor j/2 \rfloor$ represents the integer part of $j/2$. Therefore, the support of $U_j(r,\theta)$ is a polar "wedge" which is defined by the supports of radial and angular windows given by $W(r)$ and $V(t)$ respectively as shown in Figure 2.3 which summarizes the curvelet tiling in frequency plane and spatial domain. In order to get real valued curvelets, the symmetrized form of Equation (2.19), i.e., $U_j(r,\theta)+U_j(r,\theta+\pi)$ is considered. Now we define the waveform $\varphi_j(x)$ with the help of its Fourier transform $\hat{\varphi}_j(\omega)=U_j(\omega)$ where the notations are slightly modified by assuming $U_j(\omega_1,\omega_2)$ as the window defined in the polar coordinate system given by Equation (2.19). The function φ_j is considered as the "mother" curvelet which implies that all curvelets at scale 2^{-j} are derived by a) rotation and b) translation of φ_j. Introducing the equally spaced order of rotation angles given by

$$\theta_l = 2\pi.2^{-\lfloor j/2 \rfloor}.l \qquad (2.20)$$

where $l = 0, 1,..$ so that $0 \le \theta_l \langle 2\pi$

(spacing between consecutive angle is scale dependent). Similarly, the sequence of introduced translational parameters is given by $k=(k_1,k_2)\in Z^2$.

Therefore, with the notations mentioned above, curvelet can be defined $(as\ a\ function\ of\ x=(x_1,x_2))$ at scale 2^{-j}, orientation θ_l and position $x_k^{(j,l)} = R_{\theta l}^{-1}\left(k_1.2^{-j}, k_2.2^{-j/2}\right)$ as

$$\varphi_{j,l,k}(x) = \varphi_j\left(R_{\theta l}\left(x - x_k^{(j,l)}\right)\right) \qquad (2.21)$$

where R_θ implies rotation by an angle of θ radians and R_θ^{-1} is the inverse or transpose of R_θ.

$$R_\theta = \begin{pmatrix} \cos\theta & \sin\theta \\ -\sin\theta & \cos\theta \end{pmatrix}, \qquad (2.22)$$

and $$R_\theta^{-1} = R_\theta^T = R_{-\theta} \qquad (2.23)$$

So a curvelet coefficient is the inner product of an element $f \in L^2\left(R^2\right)$ and a curvelet $\varphi_{j,l,k}$, which may be expressed as

$$c(j,l,k) := \left\langle f, \varphi_{j,l,k} \right\rangle = \int_{R^2} f(x)\,\overline{\varphi_{j,l,k}(x)}\,dx \qquad (2.24)$$

As the digital curvelet transform works in frequency domain, so using Plancherel's theorem [16] the inner product of Equation (2.24) can be expressed as the integration over frequency plane as

$$c(j,l,k) := \frac{1}{(2\pi)^2}\int \hat{f}(\omega)\overline{\hat{\varphi}_{j,l,k}(\omega)}d\omega = \frac{1}{(2\pi)^2}\int \hat{f}(\omega)U_j\left(R_{\theta l}\omega\right)e^{i\left\langle x_k^{(j,l)},\omega\right\rangle}d\omega \qquad (2.25)$$

Just like wavelet concept, coarse scale elements are also present. We introduce low pass window, W_0 satisfying the following equation.

$$\left|W_0(r)\right|^2 + \sum_{j\geq 0}\left|W\left(2^{-j}r\right)\right|^2 = 1, \qquad (2.26)$$

for $k_1, k_2 \in \mathbf{Z}$ the coarse curvelets are defined as

$$\varphi_{j_0,k}(x) = \varphi_{j_0}\left(x - 2^{-j_0}k\right) \qquad (2.27)$$

$$\hat{\varphi}_{j_0}(\omega) = 2^{-j_0}W_0\left(2^{-j_0}|\omega|\right) \qquad (2.28)$$

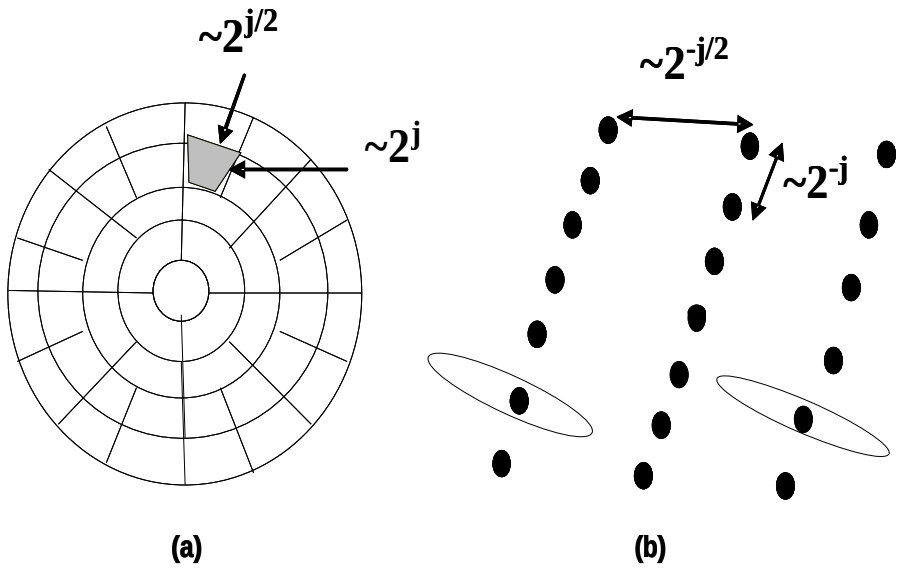

Figure 2.3 Curvelet tiling: (a) in frequency plane where shaded region represents a generic wedge $U_{j,l}(\omega)$ (b) in spatial domain. In spatial domain the bold dots represent the Cartesian grids. And the "needle" shaped elements are curvelets . The effective supports of each curvelet is a 2^{-j} by $2^{-j/2}$ rectangle [16].

So coarse curvelets are nondirectional. Hence, the "full" curvelet transform comprises of a) fine scale highly directional elements $\left(\varphi_{j,l,k}\right)_{j\geq j_0,l,k}$ and coarse scale wavelets $\left(\Phi_{j_0,k}\right)k$.

2.4 Discrete Curvelet Transform

The discrete curvelet transform (second generation) is implemented in two ways. One transform is the fast discrete curvelet transform (FDCT) based on the unequally spaced fast Fourier transform (USFFT). The other is FDCT based on the wrapping of specially selected Fourier samples. Both the transforms give the same output. But the wrapping based transform is easy to implement and takes less computation time. The two transforms differ by the selection of spatial grid which is utilized to translate curvelets at each scale and angle. The transforms generate a table of discrete curvelet coefficients which are characterized by scale, orientation and location. The transforms are simpler, faster and easily understandable as compared to 1st generation curvelet transform based on ridgelet.

As both the transforms share a common architecture of digital coronization, it is discussed before explaining individual transformation. Digital coronization [16] is a data transformation technique used to map the polar tiling of the frequency plane shown in Figure 2.3 to pseudopolar tiling of the same plane shown in Figure 2.4.

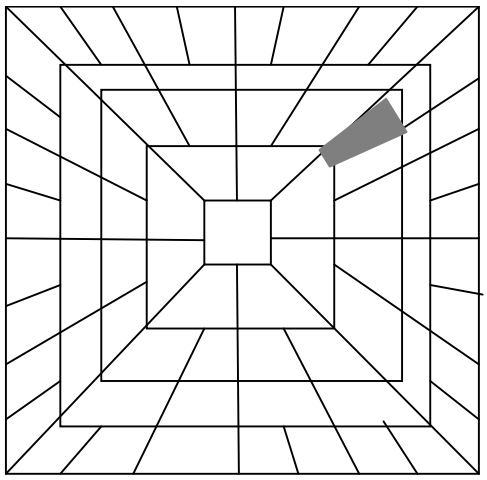

Figure 2.4 Pseudopolar digital tiling with shaded trapezoidal region representing a wedge [16].

In continuous time curvelet transform discussed in Section 2.3, window $U_j(r,\theta)$ shown by the shaded generic wedge in Figure 2.3 extracts frequencies near the dyadic corona (mathematically related concentric circles) given by $\left(2^j \le r \le 2^{j+1}\right)$ and also near the angle given by $\left(-\pi.2^{-j/2} \le \theta \le \pi.2^{-j/2}\right)$. Now the problem is that the coronae and rotations do not fit well (adapt) to Cartesian arrays. So it is better to substitute this idea by Cartesian equivalents which means the Cartesian concentric circles shown in Figure 2.3 is replaced by concentric squares and shear as shown in Figure 2.4. So the polar tiling of the frequency plane (Figure 2.3) is replaced by data friendly alternative called pseudopolar tiling (Figure 2.4). As an example it can be said that the Cartesian analog to family members $(W_j)_{j\ge 0,}\ W_j(\omega) = W\left(2^{-j}\omega\right)$ would result in a window

$$\tilde{W}_j(\omega) = \sqrt{\left(\Phi^2{}_{j+1}(\omega) - \Phi^2{}_j(\omega)\right)}, \qquad (2.29)$$

for $j \ge 0$

where Φ is the product of low pass 1D (dimension) windows given by

$$\Phi_j(\omega_1,\omega_2) = \varphi\left(2^{-j}\omega_1\right)\varphi\left(2^{-j}\omega_2\right). \qquad (2.30)$$

Here, the function φ satisfying $0 \le \varphi \le 1$, equals to 1 on $[-1/2, 1/2]$ and disappears outside the range $[-2, 2]$. So it is necessary to verify

$$\Phi_0(\omega)^2 + \sum_{j\ge 0} \tilde{W}_j^2(\omega) = 1 \qquad (2.31)$$

So the method of scale separation in a Cartesian friendly manner is understood. We now investigate the angular localization. To do so, we assume that V is as before; that is, it satisfies Equation (2.18).

$$V_j(\omega) = V\left(2^{\lfloor j/2 \rfloor}\omega_2/\omega_1\right) \qquad (2.32)$$

Now the Cartesian window can be defined with the help of $\tilde{W}_j(\omega)$ and $V(\omega)$ as

$$\tilde{U}_j(\omega) := \tilde{W}_j(\omega)V_j(\omega) \qquad (2.33)$$

It is understood that $\tilde{U}_j(\omega)$ isolates the frequencies near the wedge $\left\{(\omega_1,\omega_2): 2^j \le \omega_1 \le 2^{j+1}, -2^{-j/2} \le \omega_2/\omega_1 \le 2^{-j/2}\right\}$ and therefore it can be considered as the Cartesian equivalent to the "polar" window mentioned in Section 2.3. That is, the shaded wedge of pseudopolar tiling in Figure 2.4 is equivalent to the shaded wedge of

polar tiling in Figure 2.3. We now introduce the set of equispaced slopes given by $\tan\theta_l := l.2^{-\lfloor j/2 \rfloor}$, $l = -2^{\lfloor j/2 \rfloor},....2^{\lfloor j/2 \rfloor} - 1$, and define

$$\tilde{U}_{j,l}(\omega) := W_j(\omega) V_j\left(S_{\theta l}\omega\right) \tag{2.34}$$

where S_θ is the shear matrix given by

$$S_\theta := \begin{pmatrix} 1 & 0 \\ -\tan\theta & 1 \end{pmatrix}. \tag{2.35}$$

The angles given by θ_l are not spaced equally but the slopes are equispaced. Therefore, $\tilde{U}_{j,l}(\omega)$ signifying a concentric square based tiling as shown in Figure 2.4 is the Cartesian analog to $U_j\left(R_{\theta l w}\right)$."When completed by symmetry around the origin and rotation by $\pm \pi/2$ radians, the $\tilde{U}_{j,l}$ define the Cartesian analog to the family $U_j\left(R_{\theta l}\omega\right)$" [16] of Section 2.3. The $\tilde{U}_{j,l}(\omega)$ family denotes a concentric square tiling which is illustrated in Figure 2.4. By construction,

$$V_j\left(S_{\theta l}\omega\right) = V\left(2^{\lfloor j/2 \rfloor}\omega_2/\omega_1 - l\right) \tag{2.36}$$

and for each $\omega = (\omega_1, \omega_2)$ with $\omega_1 \rangle 0$, Equation (2.18) yields

$$\sum_{t=-\infty}^{\infty} \left|V_j\left(S_{\theta l}\omega\right)\right|^2 = 1 \tag{2.37}$$

Due to the support constraint on function V, Equation (2.37) limited to the angle of interest, i.e., $-1 \le \tan\theta_l \langle 1$, obeys

$$\sum_{all\ angles} \left|V_j\left(S_{\theta l}\omega\right)\right|^2 = 1 \tag{2.38}$$

$$\text{for } \omega_2/\omega_1 \in \left[-1+2^{-\lfloor j/2 \rfloor}, 1-2^{-\lfloor j/2 \rfloor}\right].$$

Therefore, it follows from Equation (2.31) that

$$\sum_{all\ scales} \sum_{all\ angles} \left|\tilde{U}_{j,l}(\omega)\right|^2 = 1 \tag{2.39}$$

"There is a way to define "corner" windows especially adapted to junctions over the four quadrants (east, south, west, north) so that" Equation 2.39 is true for every $\omega \in R^2$.

2.5 Fast Discrete Curvelet Transform Based on Unequispaced Fast Fourier Transform (USFFT)

According to digital coronization, the Cartesian curvelets can be expressed from [16] as

$$\tilde{\varphi}_{j,l,k}(x) = 2^{3j/4}\tilde{\varphi}_j\left(S_{\theta l}^{T}\left(x - S_{\theta l}^{-T}b\right)\right) \tag{2.40}$$

where b takes on the discrete values $b := \left(k_1.2^{-j}, k_2.2^{-j/2}\right)$. The aim is to evaluate "a digital analog of the coefficients" [16] given by

$$c(j,l,k) = \int \hat{f}(w)\tilde{U}_j\left(S_{\theta l}^{-1}\omega\right)e^{i\left\langle S_{\theta l}^{-T}b,w\right\rangle}d\omega \tag{2.41}$$

Let us assume that $\theta_l = 0$ for mathematical convenience. Now, Equation (2.41) can be easily solved by the following steps. (i) The two dimensional (2D) fast Fourier transform (FFT) of the object, $f(\omega)$ is taken to obtain $\hat{f}(\omega)$. (ii)The function $\hat{f}(\omega)$ is then multiplied with the localized window $\tilde{U}_j(\omega)$. (iii)The inverse Fourier transform is taken on proper Cartesian grid $b = \left(k_1.2^{-j}, k_2.2^{-j/2}\right)$. The difficulty arises when $\theta_l \neq 0$, and it is required to find the inverse discrete Fourier transform (DFT) on nonstandard sheared grid $S_{\theta l}^{-T}\left(k_1.2^{-j}, k_2.2^{-j/2}\right)$ where the classical FFT cannot be implemented. In order to recover suitable Cartesian grid, one can apply the shearing operation to $\hat{f}(\omega)$ and Equation (2.41) can be rewritten as

$$c(j,l,k) = \int \hat{f}(\omega)\tilde{U}_j\left(S_{\theta l}^{-1}\omega\right)e^{i\left\langle b,S_{\theta l}^{-1}\omega\right\rangle}d\omega = \int \hat{f}\left(S_{\theta l}\omega\right)\tilde{U}_j(\omega)e^{i\langle b,\omega\rangle}d\omega \tag{2.42}$$

Now if a Cartesian array $f[t_1,t_2]$ with $0 \le t_1, t_2 \langle n$, is provided and say, $\hat{f}[n_1,n_2]$ be its 2DFFT,

$$\hat{f}[n_1,n_2] = \sum_{t_1,t_2=0}^{n-1} f[t_1,t_2]e^{-i2\pi(n_1t_1+n_2t_2)/n} \tag{2.43}$$

where $-n/2 \le n_1,\ n_2 \langle n/2$

which are viewed below as samples $\hat{f}[n_1,n_2] = \hat{f}(2\pi n_1, 2\pi n_2)$ from the interpolating trigonometric polynomial denoted by $\hat{f}(\omega_1,\omega_2)$. It is defined by

$$\hat{f}(w_1,w_2) = \sum_{0 \le t_1,t_2 \langle n} f[t_1,t_2]e^{-i(\omega_1t_1+\omega_2t_2)/n} \tag{2.44}$$

Next, it is assumed that $\tilde{U}_j[n_1, n_2]$ is supported on a rectangle of $L_{1,j} \times L_{2,j}$ to result

$$P_j = \{(n_1, n_2): n_{1,0} \le n_1 \langle n_{1,0} + L_{1,j}\ ,\ n_{2,0} \le n_2 \langle n_{2,0} + L_{2,j} \}$$ (2.45)

where $(n_{1,0}, n_{2,0})$ is the index of the pixel present at the bottom left of the rectangle. Due to parabolic scaling, $L_{1,j}$ and L_{2j} are about 2^j and $2^{j/2}$ respectively. With the notations mentioned above, the FDCT via USFFT, simply computes

$$c^D(j,l,k) = \sum_{n_1, n_2 \in P_j} \hat{f}[n_1, n_2 - n_1 \tan\theta_l] \tilde{U}_j[n_1, n_2] e^{i2\pi\left(k_1 n_1 / L_{1,j} + k_2 n_2 / L_{2,j}\right)}$$ (2.46)

The complete process is summarized below.

2.5.1 Algorithm of Fast Discrete Curvelet Transform Based On USFFT

i) The 2DFFT is applied and Fourier samples $\hat{f}[n_1, n_2]$ for $-n/2 \le n_1, n_2 \langle n/2$ are obtained.

ii) The Fourier samples $\hat{f}[n_1, n_2]$ are resampled (interpolated) for each scale/angle (j,l) to get samples values as

$$\hat{f}[n_1, n_2 - n_1 \tan\theta_l] \text{ for } (n_1, n_2) \in P_j.$$

iii) The interpolated (sheared) object $\hat{f}[n_1, n_2]$is multiplied by the parabolic window $\tilde{U}_j[n_1, n_2]$ to get

$$\hat{f}_{j,l}[n_1, n_2] = \hat{f}[n_1, n_2 - n_1 \tan\theta_l] \tilde{U}_j[n_1, n_2]$$ (2.47)

iv) The inverse 2DFFT is then applied to each of $\hat{f}_{j,l}$ and the discrete curvelet coefficients $C^D(j,l,k)$ are obtained.

2.6 Fast Discrete Curvelet Transform Based On Wrapping

Like FDCT via USFFT, FDCT via wrapping is also based on the same digital coronization. But the spatial grid used to translate curvelets at different scales and angles is not tilted. Here the grid is rectangular as shown in Figure 2.5. Then the curvelets is defined in exactly the same way as FDCT via USFFT [16] as

$$c(j,l,k) = \int \hat{f}(\omega) \tilde{U}_j\left(S_{\theta l}^{-1}\, \omega\right) e^{i\langle b, \omega \rangle} d\omega$$ (2.48)

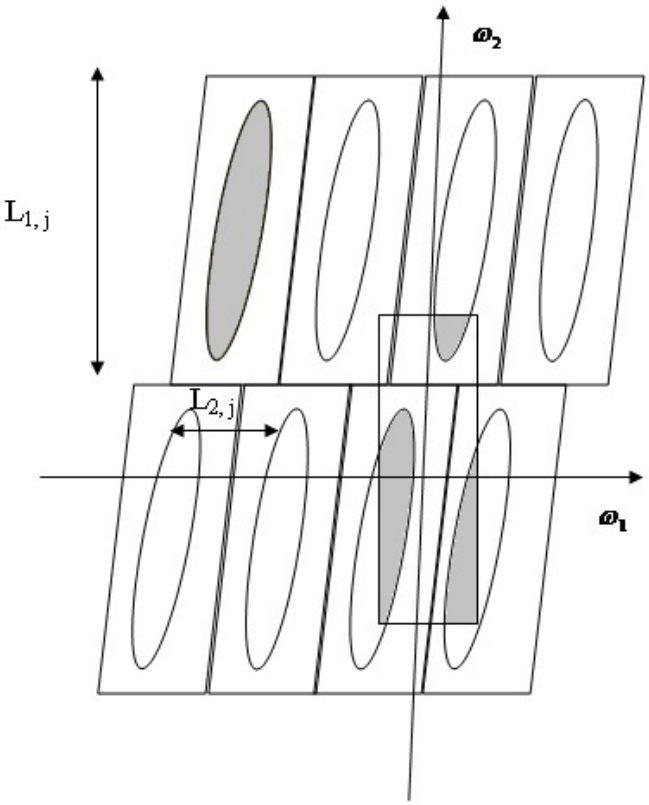

Figure 2.5 Data wrapping from a parallelogram into a rectangle by periodicity. The top and leftmost parallelogram is the tile $P_{j,l}$. It holds the frequency support of curvelet. The remaining parallelograms are the replicas formed by periodization. The rectangle with "wrapped" data (broken parts of ellipse) is centered at the origin [16].

where $b \cong \left(k_1.2^{-j}, k_2.2^{-j/2}\right)$. It is noted that $S_{\theta l}^{-T} b$ of Equation (2.41) has been substituted by $b \cong \left(k_1.2^{-j}, k_2.2^{-j/2}\right)$. The formula for b mentioned above is understood for $\theta \in \left(-\pi/4, \pi/4\right)$ or $\left(3\pi/4, 5\pi/4\right)$ else the sides of the supporting rectangle $L_{1,j}$ and $L_{2,j}$ shown in Figure 2.4 need to be exchanged.

"The difficulty behind this approach is that, in the frequency plane, the window $\tilde{U}_{j,l}[n_1, n_2]$ does not fit in a rectangle of size $\sim 2^j \times 2^{j/2}$, aligned with the axes, in which the 2D IFFT could be applied to compute" [16] Equation (2.48). Here

IFFT means inverse FFT. So the solution is to consider a parallelogram $P_{j,l}$ which contains the support of the discrete localizing window $\tilde{U}_{j,l}[n_1, n_2]$ as shown in Figure 2.5. It is assumed that for each scale j, there are two constants - $L_{1,j}$, $L_{2,j}$ so that, for each orientation θ_l, the two dimensional plane can be tiled with the translates of $P_{j,l}$ by multiples of $L_{1,j}$ along the horizontal direction and $L_{2,j}$ along vertical direction. "The corresponding periodization of the windowed data

$$d[n_1, n_2] = \tilde{U}_{j,l}[n_1, n_2]\, \hat{f}[n_1, n_2] \text{ reads} \tag{2.49}$$

$$Wd[n_1, n_2] = \sum_{m_1 \in Z} \sum_{m_2 \in Z} d[n_1 + m_1 L_{1,j}, n_2 + m_2 L_{2,j}]" \tag{2.50}$$

In this way the windowed data is "wrapped" around the rectangle centered at the origin. The complete process is summarized below.

2.6.1 Algorithm of Fast Discrete Curvelet Transform Based On Wrapping

i) The 2D FFT is applied and Fourier samples $\hat{f}[n_1, n_2]$ for $-n/2 \le n_1, n_2 < n/2$ are obtained.

ii) The product of $\tilde{U}_{j,l}[n_1, n_2]\, \hat{f}[n_1, n_2]$ is obtained for each scale j and angle l.

iii) The product is wrapped around the origin of the rectangle to get

$$\hat{f}_{j,l}[n_1, n_2] = W\left(\tilde{U}_{j,l}\, \hat{f}\right)[n_1, n_2] \tag{2.51}$$

for $0 \le n_1 < L_{1,j}$ and $0 \le n_2 < L_{2,j}$ with $\theta \in \left(-\pi/4, \pi/4\right)$.

iv) The inverse 2DFFT is applied to each $\hat{f}_{j,l}$ to get the discrete curvelet coefficients $C^D(j,l,k)$.

2.7 Conclusion

The theoretical foundation of the curvelet transform is presented in this chapter. The different properties, discrete form and practical (fast) curvelet transforms are systematically demonstrated. The concept of discrete coronization which lays the basis of both types of fast discrete curvelet transform- FDCT via USFFT and FDCT

via wrapping is thoroughly discussed. The mathematical treatment of the above transforms is followed by their respective algorithms. Most importantly, the idea and cause of polar and pseudopolar tiling of the frequency plane are exemplified with suitable illustrations.

Chapter 3

Human Skin Ringworm Detection Using Wavelet and Curvelet Transforms

3.1 Introduction

The computer vision plays a very important role in medical science. The integration of the medical imaging systems like magnetic resonance imaging, computerized tomography scan, ultrasonography with the advanced image processing software has enriched the diagnosis of human diseases. Even though the doctor gives the final decision of a patient's clinical condition, the computerized diagnosis helps him to take quick and accurate course of medication. The computer aided detection finds extensive use in the detection of colon, lung, breast and skin diseases some of which are mentioned below.

Sigurdsson *et al.* [121] proposed the detection of skin cancer based on Raman spectroscopy and feedforward neural network. The advantage of Raman spectroscopy based approach is that the molecular arrangement of the skin lesion can be investigated. Maglogiannis *et al.* [95] focused the role of the sophisticated computer vision systems to detect skin cancer at an early stage. They also highlighted the methodologies of feature extraction and skin lesion classification. The automated identification of the erthemato-squamous disease by the combined approach of the

neural network and the fuzzy logic was suggested by Ubeyli *et al.* [135]. The tree structured wavelet transform was used by Patwardhan *et al.* [109] for the sorting of malignant neoplasms. Walvick et al. [139] classified melanoma using wavelet transform based features. These features are combined to create a single feature set which is optimized by eliminating redundancies using principal component analysis. Lastly, neural network based on back propagation algorithm is used for classification. Nimunkar et al. [107] demonstrated the classification of melanoma using wavelet and statistical analysis. The skin lesion images are subjected to three level wavelet decomposition to obtain wavelet coefficients. A set of 34 features is obtained by computing statistical parameters (e.g., mean, variance) of the wavelet coefficients. These features are later utilized for melanoma classification using Mahalanobis distance. Garnavi et al. [35] addressed a computer aided diagnosis system for melanoma. The novelty of this approach is in the optimized selection and integration of features which are obtained from textural, border (boundary) based and geometrical properties of skin lesion. Das *et al.* [20] addressed the identification of skin diseases called Vitiligo, Leprosy and Tinea versicolor based on the local binary pattern (LBP) and support vector machine (SVM). The use of LBP for automatic detection of common skin disease called ringworm was proposed by Kundu *et al.* [82].

Ringworm is found in both human beings and animals. This chapter presents two approaches for the detection of human skin ringworm. The first approach deals with the 3-level decomposition of the ringworm and non-ringworm (skin disease other than ringworm) images by the Daubechies (DB), Coiflet (CF), Biorthogonal (BO) and Discrete Meyer (DM) wavelets and subsequent extraction of the corresponding energy features. Here DB represents Daubechies 1 i.e., db1 and BO represents Biorthogonoal 1.1 i.e., bior1.1 wavelets. Here 3 levels of decomposition of ringworm and non-ringworm image by a particular wavelet is selected in order to extract 4 features per wavelet. One wavelet results 4 energy features. Therefore, 4 wavelets result in 16 energy features resulting in accurate detection of ringworm images. The discriminatory energy features obtained from the wavelet decomposed approximation and detail subbands at each level of resolution are used to tabulate the training and testing databases. The binary classifier, SVM is then deployed to detect the ringworm images successfully. The second approach exploits the curvelet transform to extract the circular protrusion of ringworm images. The texture of the curvelet transformed

ringworm and non-ringworm images are statistically investigated by the gray-level co-occurrence matrix (GLCM) to generate databases with skin texture characterizing features. When these databases are provided to SVM, it classifies the skin images as ringworm and non-ringworm images. The result so obtained is promising since the image classification is based on three different cross validation techniques.

3.2 Human Skin Ringworm

The human skin diseases are of various types such as cancerous, viral, bacterial, allergic and fungal. Caused by the fungi called dermatophytes, ringworm also known as dermatophytosis [57] is found in people of all age groups. It is a highly infectious and spreads easily by direct contact between persons, pet animals, use of shaving kit, clothing, towels etc. According to Mandal [69], ringworm can be classified as Tinea corporis, Tinea capitis, Tinea barbae, Tinea pedis, Tinea cruris and Onychomycosis when the site of infection is at the skin surface, scalp region, beard area, foot, groin and nail respectively.

(a) (b) (c)

Figure 3.1 Human skin ringworm images (a) [73], (b) [73], (c) [61].

(a) (b) (c)

Figure 3.2 Human skin non-ringworm images: (a) Eczema (Dermatitis) [61], (b) Psoriasis [61], (c) Lepromatous Leprosy [61].

The prominent characteristic of ringworm as shown in Figure 3.1 is a circular red skin lesion with single or multiple outer edges [50], [57], [69], [71]. The centre of the round inflamed skin is generally pale with the outer edge being scaly and filled with oozing blisters [71]. As the ringworm is clinically diagnosed by its appearance [69], [73], its texture is analyzed here by wavelet and curvelet transforms. In order to perceive the visual variability in the texture, human skin ringworm and non-ringworm images are presented in Figure 3.1 and Figure 3.2 respectively.

3.3 SVM: An Overview

Developed by Vapnik [29], SVM is a machine learning tool which is formulated on the principle of Structural Risk Minimization Technique. The basic steps of classification are learning, testing and performance evaluation. The significant feature of SVM classification is its superior performance when tested with untrained data.

The mathematical analysis of SVM classification [29] is presented here. Suppose, vector $\mathbf{x} \in R^n$ represents a pattern which we want to classify. The class labels are represented by the scalar y such that $y \in (\pm 1)$. Also r training samples are represented by $\{(\mathbf{x}_i . y_i),\ i = 1, 2, ...r\}$. Now the challenge is to create an efficient classifier, $f(\mathbf{x})$ which can rightly segregate an input $\mathbf{x}$ which is not previously trained. The first classifier is the Linear SVM classifier where the training patterns are separated in a linear manner. It can be mathematically represented by the following linear function

$$f(\mathbf{x}) = \mathbf{w}^T \mathbf{x} + b \tag{3.1}$$

For each training sample $\mathbf{x}_i$, Equation (3.1) gives

$$f(\mathbf{x}_i) \geq 0 \text{ when } y_i = +1 \tag{3.2}$$

$$f(\mathbf{x}_i) < 0 \quad \text{when } y_i = -1 \tag{3.3}$$

This means the training samples belonging to two dissimilar classes are classified with the help of the hyperplane given by

$$f(\mathbf{x}) = \mathbf{w}^T x + \mathbf{b} = 0 \tag{3.4}$$

There can be more than one hyperplane for a given training set. But the SVM classifier considers that particular hyperplane which ensures maximum margin between the entities of the two classes as shown in Figure 3.3. This hyperplane can be determined by the minimization of the cost function given below

$$J(\mathbf{w}) = \frac{1}{2}\mathbf{w}^T\mathbf{w} = \frac{1}{2}\|\mathbf{w}\|^2 \tag{3.5}$$

and satisfying the following separability conditions

$$y_i(\mathbf{w}^T\mathbf{x}_i + b) \geq 1 \tag{3.6}$$

$$\text{for} \quad \xi_i \geq 0; \quad i = 1, 2, ...r$$

In practice, it is very difficult to completely separate the samples of training data by means of hyperplane. Under such a condition, the slack variables represented by ξ_i is put in Equation (3.6) to modify the separability constraint given by

$$y_i(\mathbf{w}^T\mathbf{x}_i + b) \geq 1 - \xi_i \tag{3.7}$$

$$\text{for } \xi_i \geq 0; \; i = 1, 2, ...r$$

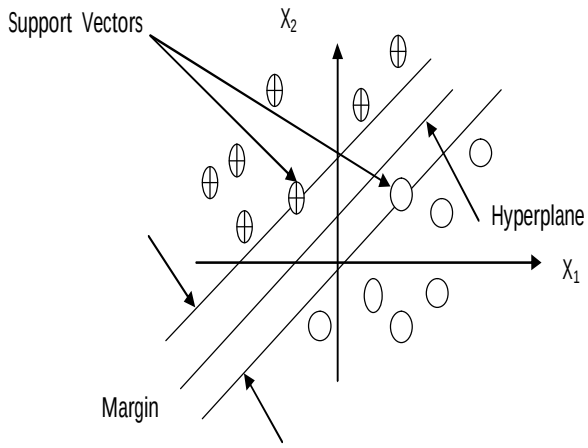

Figure 3.3 SVM classification where ⊕ and O represent the two types of data. Support vectors are the closet data points to the hyperplane [29].

As a result the cost function given by Equation (3.5) is modified as below

$$J(\mathbf{w}.\xi) = \frac{1}{2}\|\mathbf{w}\|^2 + C\sum_{i=1}^{l}\xi_i \tag{3.8}$$

where C is a positive parameter mentioned by the user with ξ being a vector comprising of all the slack variables $(\xi_i, i = 1, 2, ...r)$. The linear SVM discussed so far can also be extended to a nonlinear classifier. For this a non-linear operator $\phi(.)$ is required for mapping the input pattern into higher dimension. The non linear SVM can be written as

$$f(\mathbf{x}) = \mathbf{w}^T \phi(\mathbf{x}) + b \tag{3.9}$$

The above equation is linear with respect to the transformed data $\phi(x)$. But it is nonlinear in the context of the original data given by $x \in R^n$. The parameters of the classifier, $f(x)$ are evaluated as follows

$$\min J(\mathbf{w}.\xi) = \frac{1}{2}\|\mathbf{w}\|^2 + C\sum_{i=1}^{l} \xi_i \tag{3.10}$$

satisfying the following condition

$$y_i (\mathbf{w}^T \phi(\mathbf{x}_i) + b) \geq 1 - \xi_i \tag{3.11}$$

$$\text{for } \xi_i \geq 0;\ i = 1, 2, ...r$$

3.4 Proposed Methodology I: Human Skin Ringworm Detection using Wavelet Energy Feature

Figure 3.4 demonstrates the application of the wavelet transform to detect human skin ringworm images. The ringworm image is detected from a set of ringworm and non-ringworm images using the wavelet extracted energy features and SVM classification. The ringworm texture shown in Figure 3.1 has a scaly crusted rash on the surface. The skin images when subjected to DB, CF, BO and DM wavelets generate energy features. These wavelets are selected because all of these are compactly supported and can be implemented in discrete and continuous domains. As the wavelets are biorthogonal, they are invertible. The points mentioned above are the common attributes. However, different attributes amongst them is also the reason to implement them for mining image features [36]. Moreover, wavelets like DB, BO, symlets (sym3) are already put in practice for image classification [26]. The discrete wavelet transform of the skin image results in four frequency subbands. They are 1 approximation decomposed subband and 3 detail subbands. As the energy distribution of the wavelet is extensively used for texture classification, the energy related to the

approximate and detail subbands at 3 levels of resolution are obtained by two-dimensional wavelet decomposition [5], [46], [84]. The energy features of approximate subband and horizontal, diagonal, vertical detail subbands are used to tabulate the training and testing databases of ringworm and non-ringworm images.

According to the guideline of feature selection for any image classification problem [46], the features should be interdependent to ensure high degree of classification accuracy. Here, the dependence of the detail subband energy on the approximation subband energy for DB, CF, BO and DM wavelets applied to ringworm images is displayed in the scatter plots as shown in Figures 3.5 to 3.8 with correlation coefficients -0.8, -0.82, -0.83, -0.84 respectively. Similarly the dependence of the detail subband energy on the approximate subband energy for the same wavelets but applied to non-ringworm images is investigated and the correlation coefficients are -0.83, -0.83, -0.87, -0.81 respectively. The correlation coefficients obtained for the ringworm and non-ringworm images suggest a strong inverse relation between the two types of subband energies. Thus, the ringworm image detection

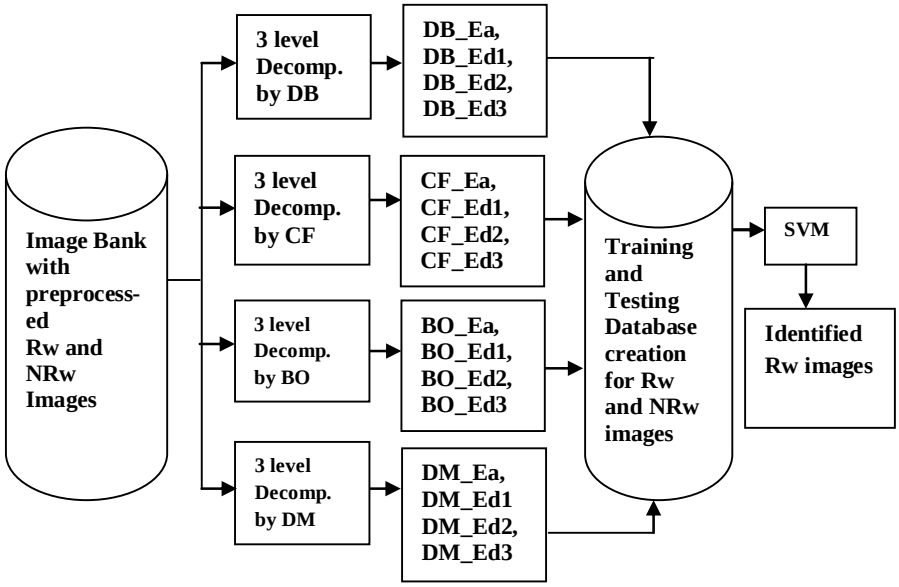

Figure 3.4 The 3-level decomposition of the preprocessed Ringworm (Rgw) and Non-ringworm (NRgw) images by Daubechies (DB), Coiflet (CF), Biorthogonal (BO) and Discrete Meyer (DM) wavelets. Also 'X'_Ea, 'X'_Ed1, 'X'_Ed2, 'X'_ED3 are the extracted energy features for the approximate suband and detail subbands at 1^{st}, 2^{nd} and 3^{rd} decomposition levels respectively where 'X' represents the DB, CF, BO and DM wavelets. Also, Decomp: Decomposition [115].

demonstrated by SVM classification is accurate.

In a supervised learning system, when the SVM is trained by training databases of ringworm and non-ringworm images given in Tables 3.1 and 3.2 respectively; it recognizes the ringworm images from the untrained images.

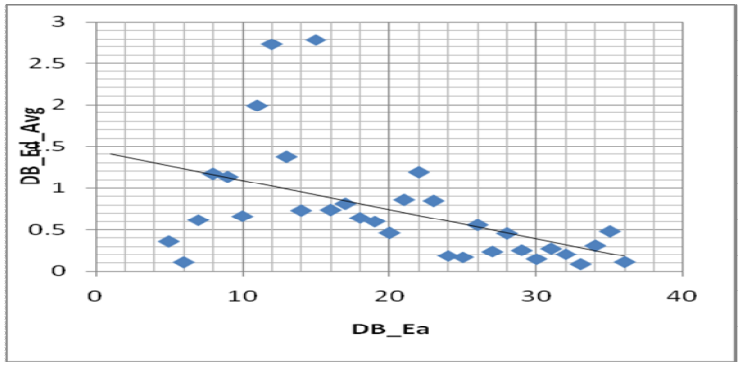

Figure 3.5 Scatter plot displaying average detail subband energy, DB_Ed_Avg as a function of approximation subband energy, DB_Ea for DB wavelet applied to ringworm image. DB_Ed_Avg is the mean of DB_Ed1, DB_Ed2 and DB_Ed3 where DB_Ed1, DB_Ed2 and DB_Ed3 are sum of the vertical, diagonal and horizontal detail subband energies corresponding to 1st , 2nd and 3rd levels of wavelet decomposition.

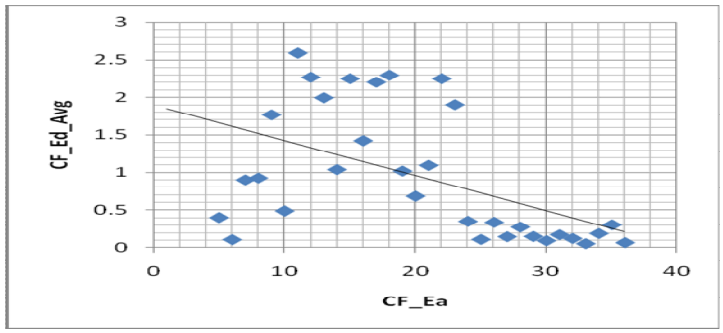

Figure 3.6 Scatter plot displaying average detail subband energy, CF_Ed_Avg as a function of approximation subband energy, CF_Ea for CF wavelet applied to ringworm image. CF_Ed_Avg is the mean of CF_Ed1, CF_Ed2 and CF_Ed3 where CF_Ed1, CF_Ed2 and CF_Ed3 are sum of the vertical, diagonal and horizontal detail subband energies corresponding to 1st, 2nd and 3rd levels of wavelet decomposition.

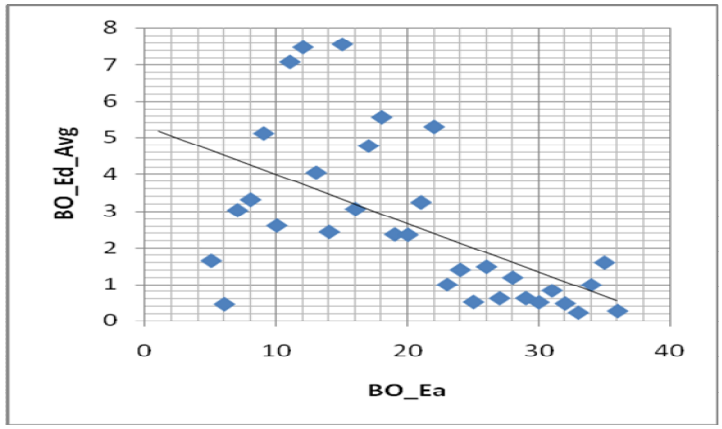

Figure 3.7 Scatter plot displaying average detail subband energy, BO_Ed_Avg as a function of approximation subband energy, BO_Ea for BO wavelet applied to ringworm image. BO_Ed_Avg is the mean of BO_Ed1, BO_Ed2 and BO_Ed3 where BO_Ed1, BO_Ed2 and BO_Ed3 are sum of the vertical, diagonal and horizontal detail subband energies corresponding to 1st, 2nd and 3rd levels of wavelet decomposition.

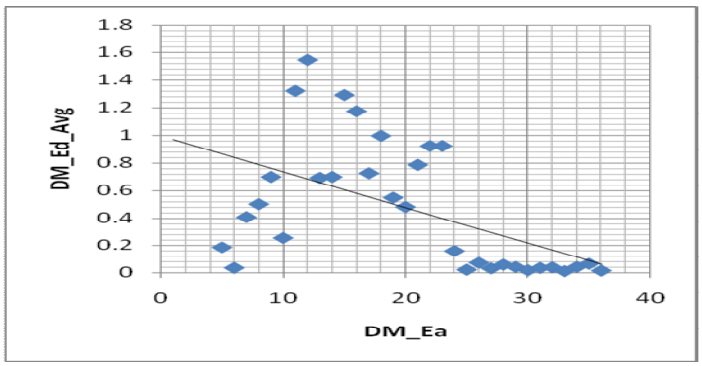

Figure 3.8 Scatter plot displaying average detail subband energy, DM_Ed_Avg as a function of approximation subband energy, DM_Ea for DM wavelet applied to ringworm image. DM_Ed_Avg is the mean of DM_Ed1, DM_Ed2 and DM_Ed3 where DM_Ed1, DM_Ed2 and DM_Ed3 are sum of the vertical, diagonal and horizontal detail subband energies corresponding to 1st, 2nd and 3rd levels of wavelet decomposition.

Table 3.1 Ringworm training database with the approximate and detail subband energies of the ringworm images decomposed by the DB, CF, BO and DM wavelets. DB_Ea, CF_Ea, BO_Ea and DM_Ea represent the percentage of energy corresponding to the approximate subbands caused due to DB, CF, BO and DM respectively. Also DB_Edn, CF_Edn, BO_Edn and DM_Edn represent the sum of the energy vectors corresponding to the horizontal, diagonal and vertical details for DB, CF, BO and DM respectively at n level of resolution with $1 \leq n \leq 3$

Im No.	Daubechies Wavelet				Coiflet Wavelet				Biorthogonal Wavelet				Discrete Meyer Wavelet			
	DB_ Ea	DB_ Ed1	DB_ Ed2	DB_ Ed3	CF_ Ea	CF_ Ed1	CF_ Ed2	CF_ Ed3	BO_ Ea	BO_ Ed1	BO_ Ed2	BO_ Ed3	DM_ Ea	DM_ Ed1	DM_ Ed2	DM_ Ed3
1	98.91	0.18	0.42	0.49	98.81	0.07	0.43	0.69	95.1	0.06	0.75	4.09	99.44	0.01	0.14	0.41
2	99.68	0.06	0.12	0.14	99.69	0.02	0.11	0.17	98.66	0.02	0.23	1.09	99.88	0	0.03	0.08
3	98.14	0.54	0.62	0.69	97.32	0.19	0.91	1.58	90.93	0.2	0.76	8.11	98.78	0.04	0.31	0.88
4	96.48	0.76	1.57	1.19	97.24	0.34	1.08	1.34	90.09	0.21	3.22	6.48	98.48	0.06	0.43	1.02
5	96.59	1.29	1.17	0.95	94.72	0.73	1.87	2.68	84.65	0.56	3.11	11.67	97.9	0.16	0.65	1.29
6	98.01	0.29	0.89	0.81	98.55	0.11	0.56	0.78	92.18	0.1	1.99	5.72	99.22	0.02	0.22	0.53
7	94.03	2.09	2.31	1.57	92.25	1.21	2.91	3.63	78.76	0.86	5	15.38	96.03	0.28	1.19	2.49
8	91.8	3.03	2.9	2.27	93.19	1.8	2.42	2.58	77.56	1.32	8.11	13	95.37	0.52	1.38	2.73
9	95.88	0.46	1.23	2.43	94.03	0.2	0.94	4.83	87.88	0.15	1.34	10.63	97.92	0.03	0.3	1.75
10	97.8	0.31	0.48	1.41	96.9	0.13	0.68	2.29	92.7	0.11	0.26	6.93	97.9	0.03	0.22	1.85
11	91.64	3.29	3.07	2	93.26	1.88	2.38	2.48	77.34	1.56	8.48	12.63	96.13	0.44	1.21	2.22
12	97.78	0.17	0.54	1.51	95.73	0.16	0.99	3.11	90.83	0.04	1.99	7.14	96.48	0.04	0.66	2.82
13	97.56	0.8	0.73	0.91	93.4	0.4	1.97	4.23	85.7	0.28	0.82	13.2	97.82	0.08	0.54	1.56
14	98.07	0.71	0.57	0.65	93.11	0.4	1.87	4.61	83.36	0.3	0.43	15.91	97	0.1	0.71	2.18
15	98.2	0.99	0.49	0.32	96.96	0.72	0.97	1.35	92.9	0.69	1.34	5.07	98.35	0.26	0.47	0.92
16	98.61	0.15	0.49	0.75	97.96	0.14	0.6	1.29	92.94	0.05	1.76	5.26	98.55	0.04	0.38	1.03
17	97.42	0.51	0.94	1.13	96.73	0.23	1.02	2.02	90.29	0.16	1.63	7.91	97.64	0.05	0.5	1.81
18	96.42	0.28	1.07	2.23	93.27	0.37	1.48	4.89	84.13	0.05	3.61	12.21	97.22	0.06	0.61	2.1
19	97.46	0.42	1.01	1.11	94.3	0.23	1.59	3.87	82.63	0.14	1.83	15..41	97.23	0.05	0.64	2.08
20	99.44	0.05	0.17	0.34	98.96	0.04	0.26	0.74	95.83	0.01	0.56	3.6	99.53	0.01	0.11	0.36
21	99.49	0.15	0.19	0.17	99.69	0.1	0.12	0.09	98.47	0.09	0.49	0.94	99.93	0.02	0.02	0.03
22	98.33	0.53	0.64	0.5	99	0.3	0.4	0.3	95.59	0.29	1.69	2.44	99.79	0.05	0.08	0.09
23	99.28	0.21	0.25	0.26	99.58	0.13	0.15	0.14	98.19	0.13	0.64	1.05	99.9	0.02	0.03	0.05
24	98.63	0.39	0.53	0.45	99.19	0.23	0.32	0.26	96.46	0.2	1.29	2.05	99.82	0.04	0.06	0.08
25	99.24	0.17	0.28	0.32	99.57	0.1	0.16	0.17	98.18	0.08	0.56	1.19	99.88	0.02	0.04	0.07
26	99.56	0.07	0.19	0.18	99.74	0.05	0.11	0.1	98.51	0.03	0.37	1.09	99.94	0.01	0.02	0.03
27	99.17	0.24	0.34	0.25	99.5	0.15	0.21	0.14	97.55	0.12	1.01	1.32	99.89	0.03	0.04	0.04

Table 3.2 Non-ringworm training database containing the approximate and detail subband energies of the non-ringworm images decomposed by the DB, CF, BO and DM wavelets. DB_Ea, CF_Ea, BO_Ea and DM_Ea represent the percentage of energy corresponding to the approximate subbands caused due to DB, CF, BO and DM respectively. Also DB_Edn, CF_Edn, BO_Edn and DM_Edn represent the sum of the energy vectors corresponding to the horizontal, diagonal and vertical details for DB, CF, BO and DM respectively at n level of resolution with $1 \leq n \leq 3$.

Im No.	Daubechies Wavelet				Coiflet Wavelet				Biorthogonal Wavelet				Discrete Meyer Wavelet			
	DB_ Ea	DB_ Ed1	DB_ Ed2	DB_ Ed3	CF_ Ea	CF_ Ed1	CF_ Ed2	CF_ Ed3	BO_ Ea	BO_ Ed1	BO_ Ed2	BO_ Ed3	DM_ Ea	DM_ Ed1	DM_ Ed2	DM_ Ed3
1	94.16	2.07	2.39	1.37	95.67	1.08	1.71	1.54	83.59	0.8	6.48	9.13	98.01	0.23	0.69	1.08
2	98.06	0.38	0.61	0.95	97.93	0.19	0.61	1.27	93.47	0.16	1.13	5.24	98.81	0.03	0.2	0.95
3	95.25	0.71	1.59	2.45	93.97	0.48	1.49	4.06	81.08	0.24	2.24	16.44	96.62	0.09	0.57	2.71
4	97.44	0.84	0.85	0.88	95.63	0.4	1.31	2.65	88.89	0.32	1.45	9.33	97.51	0.11	0.61	1.77
5	95.03	0.83	1.77	2.36	94.48	0.63	1.82	3.08	82.42	0.26	4.76	12.56	96.07	0.15	0.99	2.78
6	96.18	1.21	1.37	1.24	94.98	0.71	1.75	2.56	85.07	0.53	3.28	11.12	97.15	0.19	0.83	1.83
7	98.89	0.42	0.36	0.33	97.73	0.17	0.74	1.36	93.66	0.16	0.43	5.74	99.16	0.04	0.23	0.57
8	99.47	0.09	0.2	0.24	99.62	0.04	0.13	0.2	97.85	0.04	0.55	1.56	99.8	0.01	0.06	0.14
9	94.28	1.55	2.24	1.92	95.77	0.8	1.64	1.78	81.93	0.64	5.62	11.81	97.68	0.17	0.73	1.43
10	96.06	0.66	1.09	2.19	92.61	0.45	1.35	5.58	86.38	0.2	2.55	10.86	95.81	0.13	0.75	3.31
11	97.17	0.82	0.92	1.09	94.87	0.47	1.7	2.97	88.47	0.3	1.42	9.81	97.32	0.13	0.75	1.81
12	97.51	0.36	0.55	1.58	95.18	0.22	0.81	3.79	90.9	0.18	0.69	8.23	98.05	0.04	0.28	1.63
13	97.32	0.55	0.65	1.48	94.24	0.35	0.72	4.68	90.73	0.24	1.74	7.29	97.73	0.09	0.35	1.84
14	95.1	0.69	1.56	2.66	93.63	0.46	1.55	4.35	88.01	0.2	2.55	9.24	95.21	0.14	0.92	3.73
15	98.61	0.28	0.36	0.75	95.59	0.16	0.43	3.82	94.77	0.11	0.77	4.34	97.9	0.05	0.22	1.84
16	93.78	1.14	2.35	2.72	89.4	0.74	2.87	6.98	76.7	0.39	4.34	18.57	94.64	0.16	1.24	3.97
17	97.7	0.18	0.53	1.59	93.21	0.15	1.08	5.56	91.79	0.1	0.44	7.68	96.54	0.03	0.39	3.04
18	97.39	0.35	0.9	1.36	93.37	0.21	1.71	4.71	81.18	0.1	1.33	17.38	96.58	0.05	0.1	2.67
19	96.99	0.28	1.06	1.67	96.15	0.16	1.05	2.64	88.28	0.08	1.56	10.08	97.86	0.03	0.4	1.72
20	97.2	0.39	0.96	1.45	91.18	0.29	1.97	6.57	82.28	0.14	1.4	16.18	93.65	0.09	1.1	5.16
21	95.9	0.57	1.18	2.35	92.87	0.6	1.57	4.96	86.83	0.27	3.1	9.8	93.24	0.22	1.24	5.3
22	97.59	0.52	0.88	1	97.46	0.23	0.88	1.43	91.61	0.18	1.55	6.66	98.55	0.06	0.4	1
23	96.82	1.22	1.11	0.85	92.21	0.74	2.65	4.4	85.25	0.47	1.61	12.68	95.83	0.23	1.21	2.72
24	95.08	1.62	1.8	1.5	96.66	0.82	1.24	1.28	86.84	0.68	4.64	7.84	98.11	0.18	0.58	1.14
25	98.97	0.47	0.33	0.23	98.23	0.18	0.61	0.98	94.16	0.2	0.42	5.21	99.4	0.04	0.17	0.39
26	97.92	0.34	0.65	1.08	96.17	0.2	0.85	2.78	82.09	0.13	0.98	16.8	98.3	0.04	0.3	1.37
27	98.82	0.28	0.41	0.5	97.26	0.18	0.48	2.08	89.69	0.12	1.1	9.09	98.77	0.04	0.19	1

3.4.1 Texture Image Energy Feature Mining using Wavelet Transform

When the wavelet transform is applied to an image, the image is decomposed into one coarse approximation subband by the low pass filter and three detail

subbands by the high pass filter. Here, the approximation subband is decomposed recursively for three times. The structure of such a 1-level decomposition by the two dimensional discrete wavelet transform (2D-DWT) is illustrated in Figure 3.9.

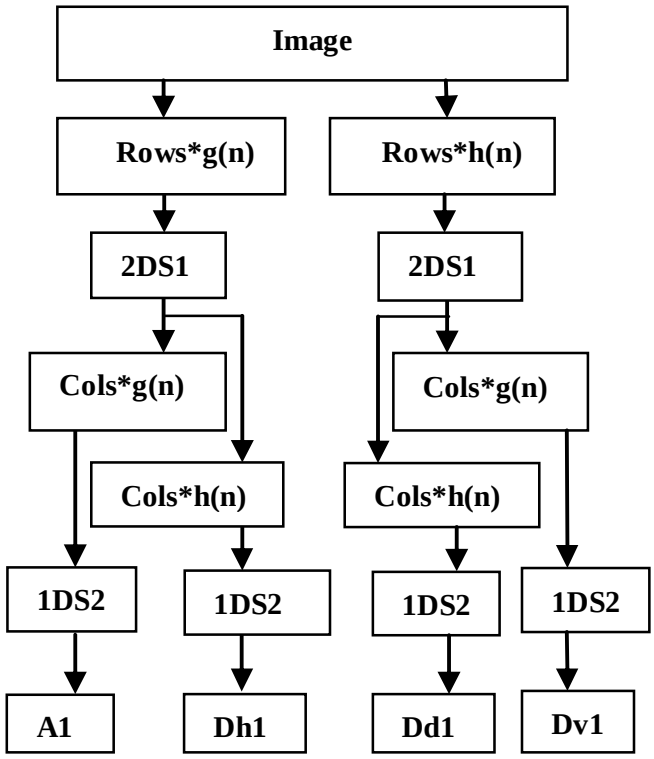

Figure 3.9 The decomposition architecture of the 2D-DWT. Here, 2DS1 implies rows are down sampled by 2 and columns by 1; 1DS2 implies rows are down sampled by 1 columns by 2. Here, "*", "cols", g(n), h(n), imply convolution operation, columns, low pass, high pass filters respectively. Also A_1, D_{h1}, D_{d1}, D_{v1} are the approximation, detail horizontal, detail diagonal and detail vertical coefficient matrices [26].

For a two dimensional skin image $f(x,y)$ with size $m \times n$, the scaling and the translation basic functions defined in [36] can be written as

$$\varphi_{j,m,n}(x,y) = 2^{j/2}\varphi(2^j x - m, 2^j y - n) \tag{3.12}$$

$$\psi^{i}_{j,m,n}(x,y) = 2^{j/2}\psi^{i}(2^j x - m, 2^j y - n) \tag{3.13}$$

where $i = \{h,v,d\}$ are the directional wavelets represented by h: horizontal, v: vertical and d: diagonal directions respectively. The discrete wavelet transform of such image $f(x,y)$ is then given by

$$W_{\varphi}(j_0,m,n) = \frac{1}{\sqrt{MN}}\sum_{x=0}^{M-1}\sum_{y=0}^{N-1} f(x,y)\varphi_{j_0,m,n}(x,y) \tag{3.14}$$

$$W_{\psi}^{\ j}(j,m,n) = \frac{1}{\sqrt{MN}} \sum_{x=0}^{M-1} \sum_{y=0}^{N-1} f(x,y) \psi^{\ i}_{j,m,n}(x,y) \tag{3.15}$$

where $i = \{h, v, d\}$ are the directional wavelets as mentioned above and j_0 is an arbitrary scale to initiate the recursive image decomposition process. The coefficients $W_{\varphi}(j_0, m, n)$ denote the approximation subband of the image $f(x,y)$ at the initial scale j_0. For further decomposition when the scale $j \geq j_0$, the horizontal, vertical and diagonal details are added by $W_{\psi}^{i}(j,m,n)$ coefficients. The 1-level decomposition architecture shown in Figure 3.9 results in A_1(approximate), D_{h1}(detail horizontal), D_{d1}(detail diagonal), D_{v1}(detail vertical) coefficient matrices. Owing to the large number of elements in each of the matrices, the average of the matrix coefficients is then taken to represent the individual matrix by a single valued feature from which energy feature is derived and fed to the SVM for texture characterization. For example, the average of the Dv1 matrix with its corresponding energy content can be written from [5] as Equations 3.16 and 3.17. The energy corresponding to the other matrices namely D_{h1} and D_{d1} can be similarly evaluated. The texture energy features corresponding to 3 levels of decomposition for DB, CF, BO and DM wavelets are extracted to record the training and testing databases for further SVM classification.

$$Average \quad Dv1 = \frac{1}{p \times q} \sum_{x=\{p\}} \sum_{y=\{q\}} |Dv1(x,y)| \tag{3.16}$$

$$Energy = \frac{1}{p^2 \times q^2} \sum_{x=\{p\}} \sum_{y=\{q\}} (Dv1(x,y))^2 \tag{3.17}$$

3.4.2 Experimental Results

The present investigation is carried out in Matlab environment with version 7.14.0.739 (R2012a). The ringworm and non-ringworm images from [60], [61], [73] are preprocessed and stored in the image bank as pictured in Figure 3.4. The websites [60], [61], [73] did not specify the image acquisition system and images are clear. The preprocessing step includes color to gray conversion, uniform resizing into 225×225 images and histogram equalization to uniformly distribute the intensities of the output skin images. The two training databases already presented by Table 3.1 and Table 3.2 are tabulated from the ringworm and non-ringworm texture images. Similarly two testing databases are also created and shown in Tables 3.3 and 3.4 respectively.

After the database creation, the SVM with linear kernel function is trained with Tables 3.1 and 3.2. Each training database contains the wavelet extracted energy features of 27 images. After the completion of SVM training each of the two testing databases containing the energy features of 3 untrained images are provided to the SVM for classification. As the total number of testing images is 6 (ringworm: 3, non-ringworm: 3), they are returned to the corresponding training databases after testing and three new samples are borrowed from each of the two training databases for further testing. It is worth mentioning that the returned test images are considered as the training images and the borrowed images from the two training databases behave as the fresh testing samples. Since the total number of test images is small, so the training–testing set of experimentation is executed for five times. The results are shown in Figure 3.10. The several performance indexing parameters of SVM namely accuracy, sensitivity, specificity, Positive Predictive Value (PPV) and Negative

Table 3.3 Ringworm testing database with the approximate and detail subband energies of the ringworm images decomposed by the DB, CF, BO and DM wavelets. DB_Ea, CF_Ea, BO_Ea and DM_Ea represent the percentage of energy corresponding to the approximate subbands caused due to DB, CF, BO and DM respectively. Also DB_Edn, CF_Edn, BO_Edn and DM_Edn represent the sum of the energy vectors corresponding to the horizontal, diagonal and vertical details for DB, CF, BO and DM respectively at n level of resolution with $1 \leq n \leq 3$

Im No.	Daubechies Wavelet				Coiflet Wavelet				Biorthogonal Wavelet				Discrete Meyer Wavelet			
	DB_ Ea	DB_ Ed1	DB_ Ed2	DB_ Ed3	CF_ Ea	CF_ Ed1	CF_ Ed2	CF_ Ed3	BO_ Ea	BO_ Ed1	BO_ Ed2	BO_ Ed3	DM_ Ea	DM_ Ed1	DM_ Ed2	DM_ Ed3
1	99.66	0.05	0.13	0.16	99.79	0.04	0.08	0.09	98.95	0.02	0.25	0.78	99.96	0.01	0.01	0.02
2	99.09	0.34	0.33	0.24	99.45	0.21	0.2	0.14	97.49	0.21	1.05	1.25	99.88	0.04	0.04	0.04
3	98.45	0.46	0.62	0.46	99.05	0.27	0.39	0.29	95.28	0.24	1.91	2.57	99.78	0.05	0.09	0.09

Table 3.4 Non-ringworm testing database containing the approximate and detail subband energies of the non-ringworm images decomposed by the DB, CF, BO and DM wavelets. DB_Ea, CF_Ea, BO_Ea and DM_Ea represent the percentage of energy corresponding to the approximate subbands caused due to DB, CF, BO and DM respectively. Also DB_Edn, CF_Edn, BO_Edn and DM_Edn represent the sum of the energy vectors corresponding to the horizontal, diagonal and vertical details for DB, CF, BO and DM respectively at n level of resolution with $1 \leq n \leq 3$.

Im No.	Daubechies Wavelet				Coiflet Wavelet				Biorthogonal Wavelet				Discrete Meyer Wavelet			
	DB_ Ea	DB_ Ed1	DB_ Ed2	DB_ Ed3	CF_ Ea	CF_ Ed1	CF_ Ed2	CF_ Ed3	BO_ Ea	BO_ Ed1	BO_ Ed2	BO_ Ed3	DM_ Ea	DM_ Ed1	DM_ Ed2	DM_ Ed3
1	97.89	0.72	0.67	0.72	95.53	0.37	1.55	2.55	89.85	0.27	0.85	9.04	97.73	0.1	0.62	1.54
2	97.16	0.4	1.13	1.3	97.59	0.22	0.86	1.34	89.6	0.18	2.63	7.59	98.14	0.04	0.45	1.36
3	98.11	0.43	0.7	0.76	96.19	0.3	0.79	2.72	89.4	0.18	1.49	8.93	98.38	0.07	0.32	1.23

Predictive Value (NPV) mentioned in Figure 3.10 can be mathematically expressed from [48], [108] as

$$Accuracy = \frac{TP + TN}{TP + FP + FN + TN} \tag{3.18}$$

$$Sensitivity = \frac{TP}{TP + FN} \tag{3.19}$$

$$Specificity = \frac{TN}{TN + FP} \tag{3.20}$$

$$PPV = \frac{TP}{TP + FP} \tag{3.21}$$

$$NPV = \frac{TN}{TN + FN} \tag{3.22}$$

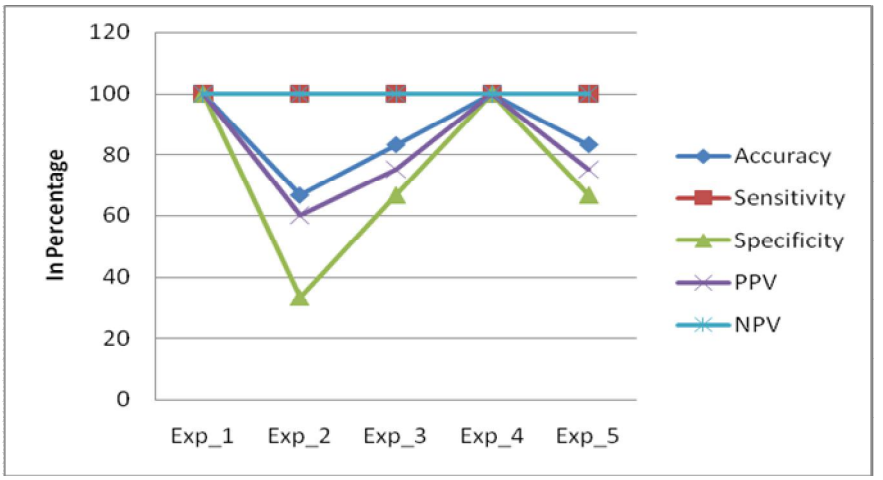

Figure 3.10 Performance analysis of SVM for proposed methodology I where Exp_1, Exp_2,..Exp_5 indicate the number of experimentations.

where TP: True Positive is the number of ringworm images which are classified as ringworm; TN: True Negative is the number of non-ringworm images which are classified as non-ringworm; FP: False Positive is the number of non-ringworm images classified as ringworm and FN: False Negative is the number of ringworm images being classified as non-ringworm.

In the five independent training-testing set of experiments as shown in Figure 3.10, the percentage of ringworm detection accuracy varies from a minimum of 66.67% to a maximum of 100% resulting in an average accuracy of 86.66%. The average sensitivity is 100%. As sensitivity is the ability of a diagnostic test to

correctly identify a sample as diseased, so high sensitivity is beneficial to detect ringworm images in our experiment. Whereas specificity denotes the ability of a diagnostic test to correctly identify a sample as without disease, so specificity reported here is also fairly good to classify the skin diseases without ringworm images [48]. The average PPV and NPV are 82% and 100% respectively where PPV refers to the percentage of images with positive test who actually have the disease and NPV denotes the percentage of images with negative test who do not have the disease.

3.5 Proposed Methodology II: Human Skin Ringworm Detection using Curvelet Transform

In this section we discuss how the curvelet transform is applied to the human skin disease images to identify the ringworms. The curvelet transform as mentioned in Chapter 2 is a multiscale image processing tool specially designed to represent edges along the curves. The novel attributes like anisotropy and anisotropy scaling of this transform motivates the implementation of the same to represent the circular inflamed lesions of the ringworm images with minimum number of discrete curvelet coefficients.

The complete methodology of human skin ringworm detection by the curvelet transform is given in Figure 3.11. It consists of three major steps. The first step

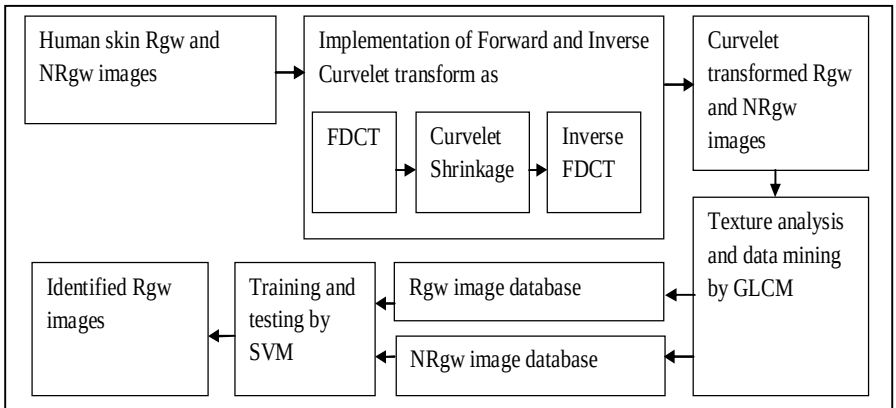

Figure 3.11 Block diagram representation of ringworm identification where Rgw: Ringworm, NRgw: Non-ringworm, FDCT: Fast Discrete Curvelet Transform, GLCM: Gray Level Co-occurrence Matrix, SVM: Support Vector Machine.

involves the application of the curvelet transform to the skin images for the feature extraction. The second step is the statistical texture investigation of the curvelet transformed skin images by the GLCM. Lastly SVM based classification is applied to distinguish the skin images as ringworm and non-ringworm very competently.

Out of the two digital implementations of the fast discrete curvelet transform (FDCT) - FDCT via Unequispaced Fast Fourier Transform and FDCT via wrapping, FDCT via wrapping is followed here for feature extraction of images due to its fast computation and ease of implementation. The algorithm of FDCT via wrapping [16] is mentioned below.

- The two dimension fast Fourier transform (2D FFT) is applied to the input skin images to get Fourier samples given by $\hat{f}[n_1, n_2]$ such that $-n/2 \le n_1, n_2 < n/2$.
- The Fourier samples so obtained are then multiplied with the Fourier transform localizing window, $\tilde{U}_{j,l}[n_1, n_2]$ to obtain $\tilde{U}_{j,l}[n_1, n_2]\hat{f}[n_1, n_2]$ for each scale j and angle l.
- The product so obtained is then wrapped around the origin to get $\tilde{f}_{j,l}[n_1, n_2] = W\left(\tilde{U}_{j,l}\,\hat{f}\right)[n_1, n_2]$ where $0 \le n_1 < L_{1,j}$ and $0 \le n_2 < L_{2,j}$ with L_{1j} and L_{2j} being the sides of the rectangular support frame used for wrapping.
- The inverse 2D FFT is applied to each $\tilde{f}_{j,l}$ to collect the discrete curvelet coefficients given by $C^D(j,l,k)$ where *D* implies "Digital" and j, l, k means that the individual coefficient is associated with scale, angle and position respectively.
- The curvelet coefficients often contain some insignificant coefficients produced due to high frequency noise. Such unimportant curvelet coefficients are removed by the process of curvelet shrinkage. The curvelet shrinkage refers to either preservation or elimination of the individual curvelet coefficient based on the type of defined shrinkage function.
- The inverse FDCT as shown in the block diagram Figure 3.11 is then applied to the matrix containing reduced curvelet coefficients to reconstruct the edge detected skin images.

3.5.1 Statistical Texture Analysis of Skin Image by GLCM

All the curvelet transformed human skin images are set for texture analysis as shown in Figure 3.11. Normally the texture of an image can be analyzed by the

statistical, structural and spectral approaches. Here the skin texture characterizing features namely the contrast, correlation, energy and homogeneity are found by GLCM [36]. The GLCM is a statistical based matrix formation technique used for texture investigation. It characterizes the skin texture by counting the number of occurrence of a pixel pair with specific intensity levels and fixed spatial relationship. Normally, the spatial relationship refers to the pixel of interest with its immediate right neighbor. But the pixel to pixel spatial relationship or offset can be user defined also. But sometimes a single GLCM, say, with horizontal offset (side by side spatial relationship) it is not possible to express the texture pattern having diagonal orientation. In such cases, multiple GLCMs with different pre-defined offsets are created for a single input image. The offsets can be defined along any one or all the directions (horizontal, vertical, diagonal) of an image. The statistical parameters obtained from the numerous GLCMs are then averaged to get the accurate results. For example, the GLCM with default horizontal offset created from an intensity image matrix I is given below. The element (4, 5) in GLCM has the value 3 because the frequency of occurrence of two horizontally adjacent pixels with intensity levels 4 and 5 in the image matrix I is thrice. Similarly the element (2, 3) in GLCM is 2 since two pixels with gray levels 2 and 3 appear twice in the input matrix I.

$$I = \begin{bmatrix} 1 & 2 & 3 & 4 & 5 \\ 2 & 1 & 6 & 2 & 3 \\ 7 & 3 & 5 & 7 & 3 \\ 6 & 2 & 4 & 5 & 8 \\ 4 & 5 & 8 & 7 & 3 \end{bmatrix}, \qquad GLCM = \begin{bmatrix} 0 & 1 & 0 & 0 & 0 & 1 & 0 & 0 \\ 1 & 0 & 2 & 0 & 0 & 0 & 0 & 0 \\ 0 & 0 & 0 & 1 & 1 & 0 & 0 & 0 \\ 0 & 0 & 0 & 0 & 3 & 0 & 0 & 0 \\ 0 & 0 & 0 & 0 & 0 & 0 & 1 & 2 \\ 0 & 2 & 0 & 0 & 0 & 0 & 0 & 0 \\ 0 & 0 & 3 & 0 & 0 & 0 & 0 & 0 \\ 0 & 0 & 0 & 0 & 0 & 0 & 1 & 0 \end{bmatrix} \tag{3.23}$$

3.5.2 Experimental Results

This part of investigation is also carried out in Matlab platform where the Curvelet toolbox version 2.1.3 [58] is installed. The ringworm and non-ringworm human skin images are taken from [60], [73]. The colored skin images are first converted into gray scale images followed by the uniform resizing and histogram equalization.

The curvelet transformed skin texture images are analyzed by the GLCM to result in two databases for the ringworm and non-ringworm images given by Table 3.5 and Table 3.6 respectively. Tables 3.5 and 3.6 present seven texture characterizing

features called mean, standard deviation, entropy, contrast, correlation, energy and homogeneity of ringworm and non-ringworm images respectively. These databases are used by SVM for training, validation and testing purposes. The non-exhaustive cross-validations namely the 5 fold and 10 fold cross-validations are followed to compare the performance of the SVM in terms of accuracy, sensitivity, specificity, PPV and NPV. But as the number of both types of skin images is limited, the experimentation is carried forward with leave-one-out cross validation in order to justify the previous validations and improve the ringworm image classification accuracy. The three cross-validation techniques used for SVM based classification are briefly discussed below.

Table 3.5 Database of ringworm images with seven statistical parameters.

Image No.	Mean	Standard Deviation	Entropy	Contrast	Corre-lation	Energy	Homo-geneity
1	114.55	53.5	7.57	0.31	0.93	0.11	0.87
2	83.58	30.66	6.95	0.42	0.72	0.17	0.83
3	99.83	43.99	7.42	0.28	0.9	0.14	0.88
4	83.49	27.84	6.79	0.28	0.78	0.22	0.87
5	111.59	45.2	7.5	0.35	0.88	0.13	0.87
6	103.67	47.52	7.45	0.22	0.93	0.13	0.9
7	93.2	44.38	7.39	0.36	0.87	0.13	0.85
8	94.77	34.68	7.1	0.14	0.92	0.23	0.93
9	127.1	56.12	7.72	0.18	0.96	0.13	0.94
10	108.33	44.46	7.46	0.28	0.91	0.13	0.87
11	100.56	26.88	6.74	0.33	0.72	0.22	0.85
12	102.21	41.55	7.22	0.14	0.99	0.19	0.95
13	128.73	49.82	7.57	0.21	0.94	0.15	0.93
14	89.54	42.63	7.34	0.41	0.85	0.13	0.84
15	133.7	28.33	6.71	0.35	0.72	0.26	0.86
16	159.03	45.46	7.42	0.17	0.94	0.17	0.93
17	155.58	62.92	7.6	0.19	0.96	0.13	0.95
18	117.12	52.98	7.62	0.26	0.93	0.13	0.89
19	144.28	42.9	7.4	0.31	0.89	0.12	0.85
20	129.7	58.65	7.63	0.28	0.94	0.14	0.94

21	191.72	30.69	6.7	0.21	0.85	0.29	0.96
22	77.9	26.19	6.7	0.31	0.72	0.25	0.87
23	106.41	21.59	6.34	0.27	0.64	0.36	0.88
24	142.79	41.87	7.39	0.29	0.89	0.15	0.89
25	208.93	37.26	6.61	0.28	0.86	0.28	0.94
26	127.51	35.83	7.12	0.52	0.74	0.14	0.79
27	97.2	36.96	7.21	0.28	0.87	0.17	0.88
28	125.33	55.64	7.54	0.11	0.97	0.15	0.94
29	168.04	44.8	7.38	0.21	0.93	0.2	0.94
30	146.85	62.39	7.65	0.11	0.98	0.15	0.95

Table 3.6 Database of non-ringworm images with seven statistical parameters

Image No.	Mean	Standard Deviation	Entropy	Contrast	Corre-lation	Energy	Homo-geneity
1	117.04	59.26	7.82	0.41	0.92	0.08	0.84
2	72.13	44.45	7.29	0.22	0.92	0.16	0.9
3	110.1	48.77	7.59	0.24	0.93	0.13	0.89
4	84.87	36.8	7.17	0.42	0.8	0.15	0.82
5	45.03	45.61	6.8	0.24	0.93	0.23	0.93
6	91.85	48.53	7.48	0.22	0.93	0.16	0.92
7	86.98	51.02	7.57	0.19	0.95	0.14	0.9
8	73.17	41.75	7.23	0.21	0.92	0.18	0.91
9	44	23.7	6.42	0.16	0.83	0.34	0.92
10	90.82	54.52	7.61	0.25	0.94	0.13	0.91
11	62.86	48.15	7.11	0.21	0.93	0.24	0.91
12	93.71	67.77	7.68	0.11	0.98	0.14	0.94
13	125.44	66.38	7.67	0.21	0.96	0.1	0.89
14	182.64	53.07	7.14	0.37	0.91	0.25	0.9
15	129.38	66.58	7.64	0.24	0.96	0.11	0.89
16	84.84	32.61	7	0.34	0.8	0.2	0.85
17	91.13	47.02	7.51	0.22	0.93	0.14	0.89
18	72.97	44.24	7.25	0.37	0.87	0.17	0.85

19	66.49	43.05	7.16	0.17	0.94	0.19	0.91
20	122.01	31.67	6.99	0.57	0.65	0.15	0.79
21	72.28	26.29	6.7	0.31	0.74	0.21	0.85
22	69.39	51.46	7.03	0.11	0.97	0.16	0.94
23	83.1	50.71	7.5	0.23	0.94	0.14	0.92
24	147.75	43.04	7.35	0.5	0.82	0.12	0.8
25	105.47	54.44	7.7	0.34	0.92	0.1	0.88
26	170.48	38.73	7.25	0.2	0.91	0.18	0.91
27	142.76	64.11	7.82	0.17	0.97	0.12	0.91
28	144.94	60.51	7.65	0.35	0.93	0.11	0.87
29	173.86	42.94	7.28	0.29	0.89	0.19	0.9
30	128.86	63.1	7.87	0.27	0.95	0.1	0.89

3.5.2.1 5 Fold Cross Validation (5FCV)

The 5FCV technique randomly divides each of the Tables 3.5 and 3.6 row-wise into 5 equal disjoint subsets. During the first iteration, 4 subsets from each table are used for SVM training; while the remaining 1 subset from each table is used for SVM testing. This process is continued for 5 times using different subsets of data from Tables 3.5 and 3.6 which are used for SVM testing. Figure 3.12 presents the result of 5FCV from which the average accuracy, sensitivity, specificity, PPV and NPV obtained are 74.8%, 73.4%, 76.6%, 80%, 81% respectively.

3.5.2.2 10 Fold Cross Validation (10FCV)

The 10FCV is conceptually same as that of 5FCV. It is followed in order to find any possible variation in SVM performance parameters. This technique randomly divides Table 3.5 and 3.6 row wise into 10 equal disjoint subsets. During the first iteration, 9 subsets from each table are used for SVM training. The remaining 1 subset is used for testing. Unlike 5FCV, this process is carried for 10 times using different subsets of data from Tables 3.5 and 3.6 which are used for SVM testing. Figure 3.13 presents the result of 10FCV from which the average accuracy, sensitivity, specificity, PPV and NPV obtained are 73.2%, 70.2%, 76.7%, 75.2%, 75.7% respectively.

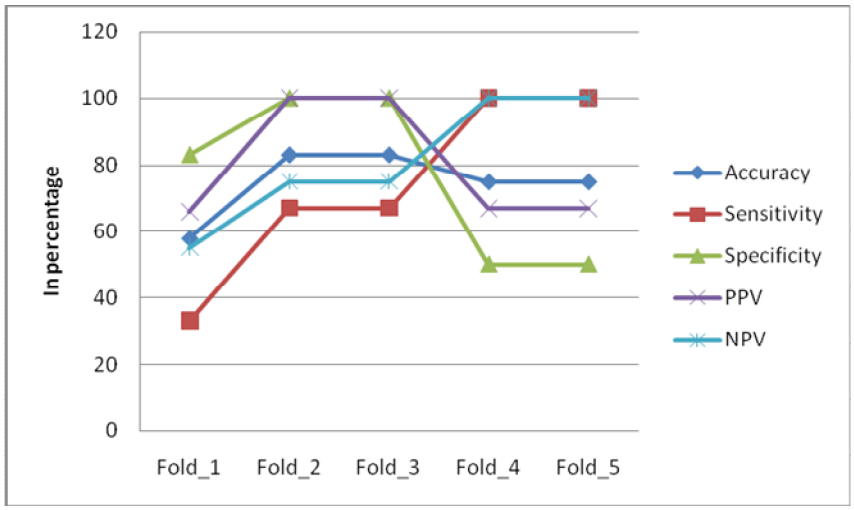

Figure 3.12 Performance analysis of SVM using 5FCV technique for proposed methodology II.

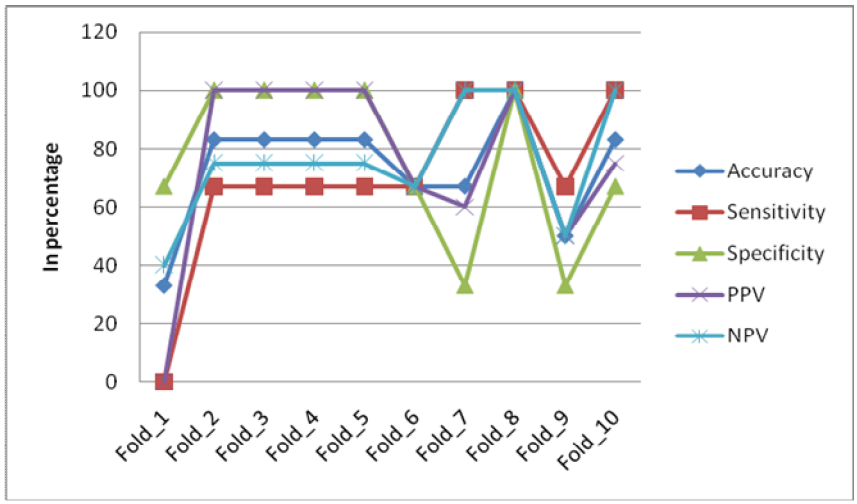

Figure 3.13 Performance analysis of SVM using 10FCV technique for proposed methodology II.

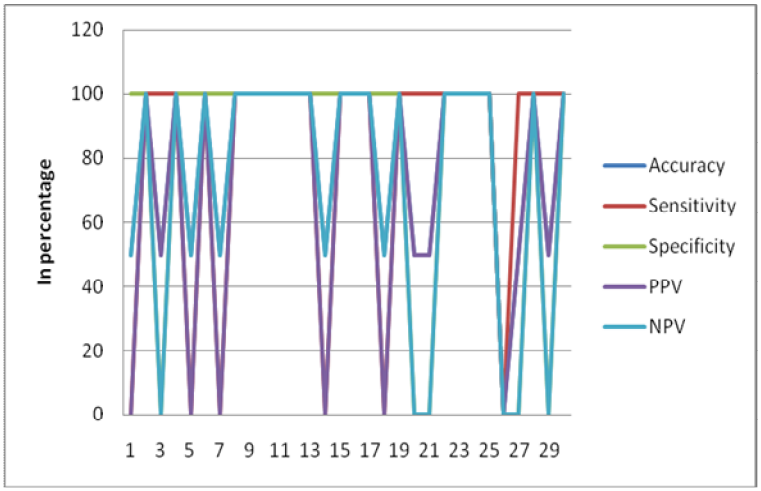

Figure 3.14 Performance analysis of SVM using LOOCV technique for proposed methodology II.

3.5.2.3 Leave-one-out Cross Validation (LOOCV)

Comparing the results of 5FCV and 10FCV, we find that the two methods yield almost similar result, especially ringworm detection accuracy. So in order to increase the detection accuracy further; LOOCV technique is implemented [47].

In this technique, only one image each from Tables 3.5 and 3.6 are considered as the two testing databases. Table 3.5 and Table 3.6 left out remaining images are used for training. With this training and testing databases, the SVM classification is continued till all the images from both the tables are individually considered for testing. Each time when the "borrowed" ringworm and non-ringworm images from Tables 3.5 and 3.6 are returned to the same, two new images are again taken for further testing. In Figure 3.14, the average accuracy, sensitivity, specificity, PPV and NPV presented are 80%, 70%, 90%, 92.86%, 83.33% respectively. So there is a considerable increase in detection accuracy as compared to 5FCV and 10FCV techniques.

3.5.2.4 Discussion on three Cross Validation Techniques

The comparison of the three cross validations is projected in Figures 3.15 and 3.16. The bargraphs presented in Figure 3.15 compare the 3 cross validation techniques in terms of accuracy, sensitivity, specificity and PPV. Figure 3.16

compares the NPV of the same techniques. It is found that LOOCV method is better than the other methods in terms of accuracy, specificity, PPV and NPV. On the other hand, as per as non-exhaustive validations are considered, the results of 5FCV and 10FCV techniques are more or less same.

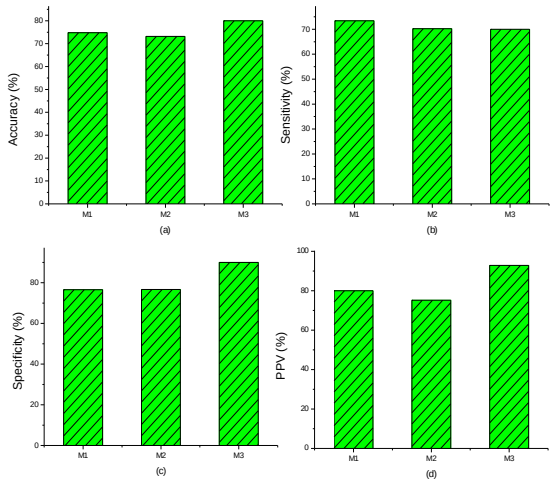

Figure 3.15 The comparison of M1, M2 and M3 in terms of average (a) accuracy of classification, (b) sensitivity, (c) specificity, (d) PPV where PPV: Positive Predictive Value. Here M1: 5FCV, M2: 10FCV, M3: LOOCV.

3.6 Comparison of the Proposed Methodology I with Proposed Methodology II

Demonstrating the human skin ringworm detection by the wavelet (Proposed Methodology I) and curvelet (Proposed Methodology II) in Section 3.4 and 3.5 respectively, the two schemes are now presented for comparison in Figure 3.17. It is found that the proposed methodology I is better than either of the three validation techniques under methodology II in terms of correct rate, sensitivity and NPV. But the proposed methodology II based on LOOCV method which is superior than 5FCV and 10FCV techniques as discussed in Section 3.5.2.4 gives higher specificity and PPV than methodology I.

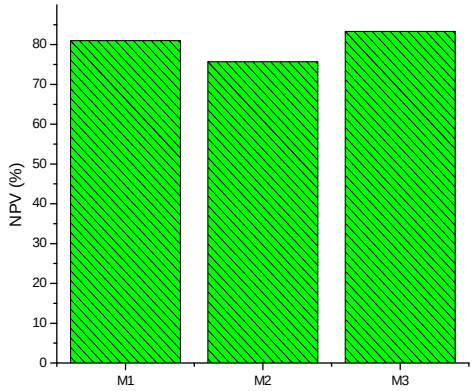

Figure 3.16 The comparison of M1, M2 and M3 in terms of average NPV where NPV: Negative Predictive Value. Here M1: 5FCV, M2: 10FCV, M3: LOOCV.

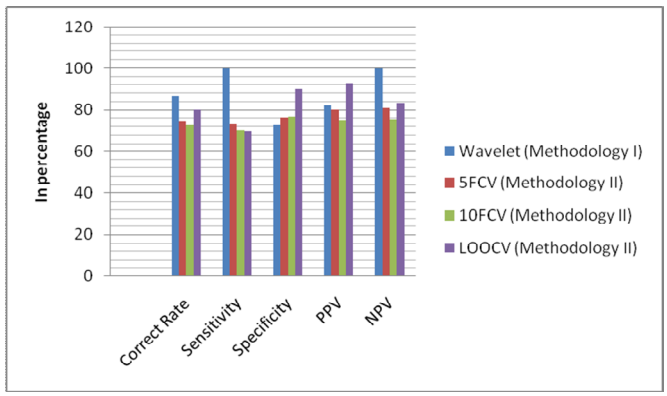

Figure 3.17 The comparison of the proposed methodology I with II in terms of the SVM performance parameters where PPV: Positive Predictive Value, NPV: Negative Predictive Value.

3.7 Comparison of Our Methodologies with Earlier Works

A comparative study between our methodology (I) and four other works based on wavelet is displayed in Table 3.7. It is to be noted that serial no 1 to 4 of Table 3.7 worked on the detection of Melanoma whereas our method detects ringworm using wavelets. This has been done because the work on ringworm detection using wavelet is rarely available. It is found that the skin disease detection accuracy of our method is

better than others. Again, the detection accuracy of methodology (I) is compared with that of methodologies based on discrete cosine transform (DCT), discrete Fourier transform (DFT), GLCM and LBP [20] in Figure 3.18. It is conceived from Figure 3.18 that with minimum number of features our methodology provides superior skin disease detection accuracy.

The above discussion is made in the context of comparing the methodologies related to skin disease detection. It is already mentioned above that the literature survey hardly provides any work on automated human skin ringworm detection except [82]. So our proposal, especially methodology (II) which is similar to [82] in implementing cross-validation technique is set for assessment. The 10FCV results of methodology II and [82] are compared in Figure 3.19. The percentage of average detection accuracy of our methodology (II) and [82] are 73.2 and 74.28 respectively. Our proposed ringworm detection accuracy is close to that obtained in [82]. Unlike [82], our methodology (both I and II) provides several useful diagnostic parameters-sensitivity, specificity, PPV and NPV to evaluate the overall SVM performance of ringworm detection.

Table 3.7 Comparison of our approach with other works
(Serial No. 1, 2, 3, 4 detect melanoma; Serial 5 detects ringworm)

Serial No.	Authors	Based on the following algorithms	Accuracy in percent
1.	Patwardhan *et al*. [109]	Tree structured wavelet transform which utilizes the spatial and frequency information of the skin lesions.	52.94
2.	Walvick *et al.* [139]	A single feature set is created by combining all the wavelet transform based features. The feature set is optimized by eliminating redundancies with the help of principal component analysis.	82.35
3.	Nimunkar *et al*. [107]	The computation of several statistical features like mean, variance, entropy, energy of the wavelet coefficients. The	83.33

		discriminant functions are evaluated with Mahalanobis distance.	
4.	Garnavi et al. [35]	Computer supported diagnostic system. The features are optimally selected and integrated from a) textural, b) border based and c) geometric properties of the affected lesion.	86.27
5.	Our method	Methodology I based on wavelet energy feature	86.66

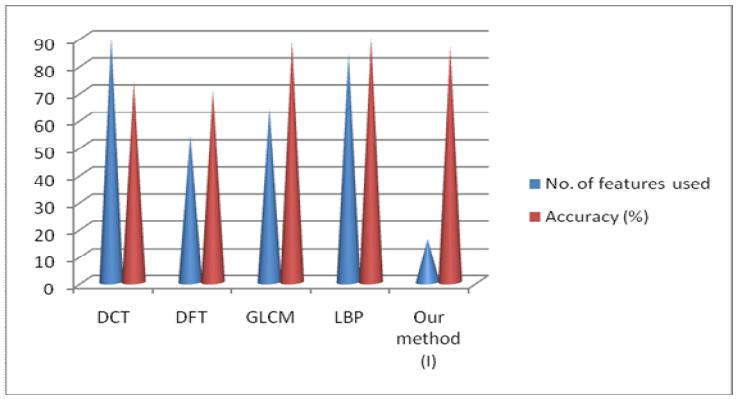

Figure 3.18 Comparison of our method (I) with methodologies based on DCT: Discrete Cosine Transform, DFT: Discrete Fourier Transform (DFT), GLCM: Gray Level Co-occurrence Matrix (GLCM) and LBP: Local Binary Pattern (LBP).

3.8 Conclusion

In this chapter, the frequently observed human skin disease called ringworm is detected by two approaches. One approach is the wavelet based technique and the other is the curvelet based method. Both the techniques are hopefully the first research proposals in their respective fields.

The wavelet based approach deploys four members of the wavelet family to strongly discriminate the energy features of the approximation and detail subbands of the skin images produced during each level of wavelet decomposition and subsequent

binary classification. And the ringworm detection accuracy is about 87%. The sensitivity is exceptionally good while the specificity can be improved.

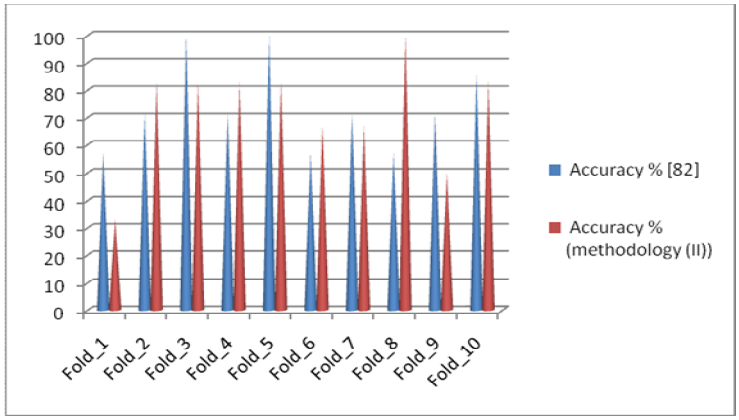

Figure 3.19 Comparison of 10FCV [82] with our methodology (II).

The scheme deploys curvelet transform for texture feature extraction, GLCM for statistical investigation and SVM for image classification. The average detection accuracy obtained from this approach with LOOCV technique is 80%. The advantage of the second scheme is that the SVM classification is based on 3 types of cross-validation techniques which help to evaluate SVM performance parameters called accuracy, sensitivity, specificity, PPV and NPV very efficiently. It is observed that 5FCV and 10FCV techniques present almost close results. The LOOCV is implemented in accordance to the pattern recognition literature due to the confined number of sample images and the results so obtained are quite satisfactory. The other remarkable feature of LOOCV technique is the high average specificity which allows to consider ringworm images with positive outcome from the classifier. Therefore, the ringworm positive patients can be easily identified with the help of the suggested methodologies.

Moreover, the two approaches do not require any extra hardware other than simple image acquisition system. In future, the work can be extended further with the application of both wavelet and curvelet transforms to increase the detection accuracy of the ringworm images.

Chapter 4

Darier Disease-A Genetic Disorder Detection using Wavelet and other Methods

4.1 Introduction

With the advent of computer-aided diagnosis, there is a rapid development of dermatology. It helps to remove subjectivity and unreliability from conventional diagnosis. The dermatologists can develop a sound opinion from the computerized skin screening technology.

A vast literature [95] is available on computer supported skin cancer investigation and characterization. Garnavi *et al.* [35] address the detection of malignant melanoma with the help of wavelet based textural analysis. The erythemato-squamous diseases like psoriasis, pityriasis rubra pilaris, seboreic dermatitis, pityriasis rosea, lichen planus and chronic dermatitis share common clinical features with little differences. So they are very difficult to differentiate. Ubeyli and Güler [135] proposed the automated detection of six such erythemato-squamous diseases using adaptive neuro-fuzzy system. The identification of leprosy, tinea versicolor and vitiligo which closely resemble each other in lesion pattern and color was addressed by Das *et al.*[20].

(a) (b)

Figure 4.1 Image of Darier disease (a) upper back with mild infection (b) foot with severe infection [59].

But the computer aided detection of Darier disease was not addressed much in the scientific literature. Darier disease is an unusual genetic disorder which is predominantly expressed as changes on skin surface [62]. The genetic disorder is inherited in autosomal dominant mode. This means the abnormal gene transmitted from a single parent to a child can cause this dermal condition. The disease inheriting probability of a child born out of two children of one affected parent is 50%. It is a non-contagious and chronic disease found in both male and female during the adolescence period. The skin becomes scaly and brownish. Innumerous greasy papules look like rough sandpaper. They appear on different parts of the human body like eye brows, forehead, sides of nose, neck, central chest, under breast, upper back, in between buttocks, groin, nail, foot etc. The papules often fuse together to form large smelly warts on the skin surface as shown in Figure 4.1. The cells of a normal skin stick together with the help of molecular complexes called desmosomes. But here, due to the presence of the unusual gene *ATP2A2* traced on chromosome 12q23-24.1, the desmosomes fail to adhere the skin cells for lack of calcium [62]. Some patients carry the diseases but do not show any noticeable symptom. While others have widespread lesions often flared by sunlight. The disease becomes intolerable when it is exacerbated by either bacterial or viral infection. As a result the patient suffers a lot of pain and agony. Keeping in view of the change in dermal surface morphology and clinical approval of appearance based diagnosis [55], [62], this particular disease is investigated in the perspective of computer vision.

In this chapter, we propose the detection of Darier skin disease by 1) gray level co-occurrence matrix (GLCM), 2) local binary pattern (LBP), and 3) wavelet

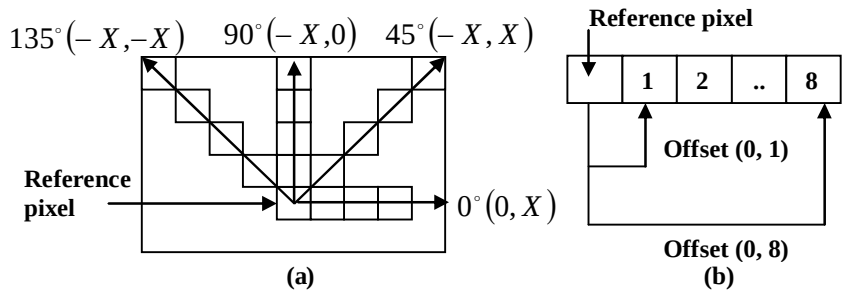

Figure 4.2 Defining offsets: (a) along four directions where X represents the distance, (b) Variation of horizontal offsets [51].

based methods. Earlier, all the three methods were implemented individually in applications like [20], [26]. But proposed methodology brings together three time tested data extracting methods on a common skin disease detection platform to investigate the individual method's disease detection accuracy followed by overall comparison. The individual method extracts texture characterizing features from the skin images and provides them to the feedforward neural network (FNN) for image detection.

Mitra *et al.* [104] demonstrates the automated skin disease identification by considering only the average of directional GLCMS and the exact number of skin surface characterizing features remains ambiguous. But our GLCM method not only computes the statistical features – contrast, correlation, energy, homogeneity along four directions $(\theta = 0^\circ, 45^\circ, 90^\circ, 135^\circ)$ as shown in Figure 4.2 (a), but also incorporates 8 offsets along each direction as shown in Figure 4.2 (b) to find distance wise average GLCM. Offset detailed in Section 4.2.1 refers to the user defined spatial relationship between two pixels of an input image from which GLCM is created. This facilitates the dual sensitiveness of proposed GLCM along direction and distance. The other salient feature of this approach is that the typical textural information e.g., periodicity of any particular lesion can be intensely investigated by the statistical parameter versus offset plot. The second approach of LBP is computationally simple and invariant to changes in gray level and rotation of an image. It is already popular amongst several image processing applications like face recognition, facial expression identification. But it is not used much in medical applications [20]. So its versatility is experimented in this chapter. The third method deploys four different wavelets called Daubechies (DB), Discrete Meyer (DM), Symlet (SY) and Biorthogonal (BO) for 3

level wavelet decomposition of skin images resulting in one approximation and three detail subbands at each level of decomposition. As the subband wise energy distribution at any given level of wavelet decomposition has the image discriminative property, so it is used here as a skin texture characterizing feature.

4.2 Proposed Methodology

In Figure 4.3, we present three independent methods founded on -1) GLCM, 2) LBP and 3) wavelet by three parallel paths to detect Darier disease from input skin texture images. Individual method mines textural features from the images of both the Darier and non-Darier (not Darier) skin diseases like diabetic gangrene, scabeies, ichthyasis congenita and provide databases to the FNN for image detection. The individual method is discussed in the subsequent sections.

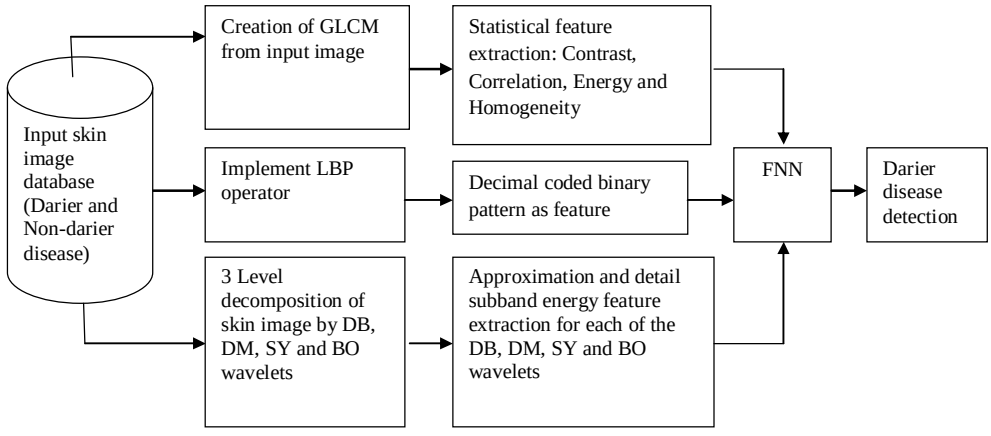

Figure 4.3 Schematic of proposed methodology where GLCM: Gray level co-occurrence matrix, LBP: local binary pattern. DB: Daubechies, DM: Discrete Meyer, SY: Symlet, BO: Biorthogonal wavelets. FNN: Feedforward Neural Network [117].

4.2.1 Textural Analysis by GLCM Methodology

In this method GLCM is first created from the input image as already explained by Equation 3.23. The statistical parameters are then evaluated from the GLCM. The four offsets, i.e., horizontal $(\theta = 0^{\circ})$offset, right diagonal $(\theta = 45^{\circ})$ offset, vertical $(\theta = 90^{\circ})$offset, and left diagonal $(\theta = 135^{\circ})$ offset are defined as shown in Figure 4.2 (a). As the skin texture varies along each direction, 8 distance offsets, i.e., [0,1] ……[0,8] as shown in Figure 4.2 (b) are incorporated to trace the horizontal variation of skin texture. Using the 8 horizontal offsets, 8 GLCMs are found and the

average horizontal GLCM is created. In a similar way the average GLCMs are found along four directions. Now, the direction wise statistical parameters called contrast, correlation, energy, homogeneity are calculated from the average horizontal, right diagonal, vertical and left diagonal GLCMs as illustrated in Table 4.1. Table 4.1 showcases the textural features of only Darier disease skin images. Using the same technique textural features of non-Darier disease skin images are tabulated and presented in Table 4.2. Tables 4.1 and 4.2 are used to create the input and target databases which are provided to FNN for image detection.

Table 4.1 The statistical features obtained from the average GLCM of Darier disease skin images. Deg: Degree

Im No.	**Contrast**				**Correlation**				**Energy**				**Homogenity**			
	0 Deg	45 Deg	90 Deg	135 Deg	0 Deg	45 Deg	90 Deg	135 Deg	0 Deg	45 Deg	90 Deg	135 Deg	0 Deg	45 Deg	90 Deg	135 Deg
1	1.51	2.19	1.69	2.53	0.83	0.74	0.80	0.70	0.05	0.05	0.05	0.04	0.76	0.69	0.74	0.69
2	0.44	0.85	0.66	0.63	0.95	0.91	0.93	0.93	0.08	0.06	0.07	0.07	0.85	0.75	0.82	0.84
3	0.92	1.57	1.31	1.47	0.89	0.82	0.85	0.83	0.05	0.04	0.05	0.04	0.76	0.69	0.70	0.69
4	2.90	4.02	1.66	3.84	0.66	0.52	0.81	0.54	0.03	0.03	0.05	0.03	0.58	0.54	0.72	0.54
5	1.70	2.19	0.87	2.30	0.80	0.73	0.90	0.73	0.05	0.04	0.06	0.04	0.71	0.65	0.79	0.65
6	3.25	4.14	3.32	3.74	0.63	0.51	0.61	0.56	0.03	0.03	0.03	0.03	0.60	0.56	0.59	0.56
7	0.76	0.87	0.63	1.21	0.91	0.91	0.93	0.86	0.06	0.06	0.07	0.05	0.76	0.75	0.81	0.72
8	1.61	2.12	1.05	2.03	0.81	0.75	0.88	0.76	0.04	0.04	0.05	0.04	0.69	0.64	0.75	0.65
9	3.68	4.04	3.31	3.95	0.57	0.52	0.61	0.53	0.02	0.02	0.03	0.02	0.55	0.53	0.56	0.53
10	0.99	2.03	1.16	1.58	0.89	0.76	0.86	0.81	0.06	0.05	0.06	0.06	0.80	0.68	0.76	0.77
11	2.87	4.62	4.49	5.00	0.67	0.43	0.46	0.38	0.03	0.02	0.03	0.02	0.61	0.53	0.55	0.53
12	2.21	2.67	1.44	2.62	0.74	0.67	0.83	0.68	0.04	0.03	0.04	0.03	0.65	0.61	0.70	0.61
13	1.67	2.54	1.79	2.58	0.81	0.71	0.79	0.70	0.04	0.04	0.04	0.03	0.70	0.64	0.69	0.63
14	0.99	0.94	0.75	1.22	0.89	0.90	0.91	0.85	0.05	0.05	0.06	0.05	0.73	0.73	0.77	0.70
15	1.12	2.17	1.86	2.18	0.88	0.74	0.78	0.74	0.04	0.04	0.04	0.04	0.69	0.64	0.70	0.65
16	0.98	2.25	1.86	2.02	0.89	0.73	0.78	0.76	0.05	0.04	0.05	0.04	0.75	0.67	0.71	0.68
17	2.02	3.49	1.93	3.45	0.76	0.58	0.77	0.58	0.04	0.03	0.05	0.03	0.67	0.61	0.73	0.60
18	1.81	2.91	2.73	3.53	0.79	0.65	0.67	0.57	0.04	0.03	0.04	0.03	0.68	0.62	0.65	0.59
19	2.51	2.61	0.85	2.96	0.70	0.69	0.90	0.65	0.04	0.04	0.05	0.04	0.66	0.66	0.76	0.63
20	4.20	4.52	2.29	4.66	0.51	0.46	0.73	0.44	0.03	0.02	0.04	0.03	0.56	0.53	0.65	0.53
21	2.52	3.23	1.57	2.94	0.70	0.61	0.82	0.65	0.03	0.03	0.05	0.03	0.62	0.58	0.71	0.61
22	2.48	2.69	0.94	2.90	0.70	0.66	0.89	0.64	0.04	0.04	0.06	0.03	0.64	0.62	0.75	0.60
23	2.22	3.60	2.63	3.63	0.75	0.59	0.71	0.59	0.03	0.03	0.03	0.03	0.65	0.58	0.62	0.56
24	0.89	1.69	1.53	2.29	0.90	0.79	0.82	0.73	0.05	0.05	0.05	0.04	0.75	0.70	0.72	0.62
25	1.87	3.49	2.59	3.48	0.79	0.59	0.69	0.59	0.04	0.03	0.04	0.03	0.69	0.60	0.65	0.59
26	1.62	2.56	1.97	2.23	0.82	0.70	0.77	0.74	0.04	0.03	0.04	0.04	0.68	0.62	0.68	0.65
27	2.93	3.54	1.84	3.46	0.65	0.57	0.78	0.58	0.03	0.03	0.04	0.03	0.58	0.56	0.68	0.57
28	1.96	2.53	2.41	2.55	0.77	0.70	0.72	0.70	0.04	0.03	0.03	0.03	0.66	0.60	0.63	0.61
29	5.03	5.75	4.13	5.63	0.42	0.34	0.53	0.35	0.03	0.02	0.03	0.02	0.55	0.51	0.57	0.51
30	2.02	2.24	0.66	2.14	0.75	0.73	0.92	0.74	0.04	0.04	0.06	0.04	0.64	0.62	0.78	0.63
31	1.78	2.14	1.70	1.99	0.80	0.76	0.81	0.77	0.04	0.04	0.04	0.04	0.68	0.63	0.66	0.65

32	0.91	1.11	0.71	1.16	0.89	0.87	0.92	0.86	0.05	0.04	0.05	0.04	0.72	0.69	0.76	0.68
33	1.96	2.62	1.20	2.47	0.77	0.68	0.86	0.70	0.04	0.03	0.05	0.03	0.64	0.60	0.75	0.62
34	1.61	2.47	1.44	2.04	0.81	0.71	0.83	0.75	0.04	0.04	0.04	0.04	0.68	0.61	0.71	0.66
35	2.89	3.46	2.41	3.79	0.67	0.59	0.72	0.56	0.03	0.03	0.03	0.03	0.60	0.57	0.62	0.56

Table 4.2 The statistical features obtained from the average GLCM of non-Darier disease skin images. Deg: Degree

Im No.	**Contrast**				**Correlation**				**Energy**				**Homogenity**			
	0 Deg	45 Deg	90 Deg	135 Deg	0 Deg	45 Deg	90 Deg	135 Deg	0 Deg	45 Deg	90 Deg	135 Deg	0 Deg	45 Deg	90 Deg	135 Deg
1	1.60	2.19	1.52	2.22	0.82	0.74	0.82	0.74	0.04	0.04	0.04	0.04	0.69	0.62	0.69	0.64
2	1.67	2.73	2.03	2.35	0.81	0.69	0.77	0.72	0.04	0.03	0.04	0.03	0.66	0.58	0.64	0.61
3	2.05	2.72	2.20	2.55	0.76	0.67	0.74	0.70	0.04	0.03	0.04	0.03	0.65	0.60	0.65	0.61
4	2.89	4.53	2.87	4.23	0.66	0.45	0.66	0.48	0.03	0.03	0.03	0.03	0.62	0.54	0.63	0.55
5	1.97	2.41	1.72	2.27	0.77	0.72	0.80	0.74	0.04	0.03	0.04	0.03	0.66	0.62	0.70	0.64
6	1.69	2.35	1.45	2.44	0.80	0.72	0.83	0.70	0.04	0.03	0.04	0.03	0.68	0.62	0.69	0.60
7	2.18	3.44	2.94	3.98	0.75	0.60	0.66	0.54	0.04	0.03	0.03	0.03	0.67	0.57	0.60	0.55
8	1.78	2.50	1.29	2.30	0.80	0.72	0.86	0.74	0.05	0.04	0.05	0.04	0.71	0.64	0.73	0.66
9	1.13	1.60	0.99	1.46	0.88	0.82	0.89	0.83	0.05	0.04	0.05	0.04	0.71	0.67	0.75	0.68
10	1.31	1.85	1.28	1.95	0.85	0.78	0.86	0.77	0.05	0.04	0.05	0.04	0.70	0.66	0.76	0.65
11	0.93	1.37	0.84	1.45	0.89	0.84	0.91	0.83	0.05	0.04	0.06	0.04	0.71	0.69	0.79	0.67
12	1.19	1.46	0.52	1.28	0.86	0.83	0.94	0.84	0.05	0.05	0.06	0.05	0.75	0.69	0.79	0.73
13	2.10	2.38	0.52	2.34	0.75	0.71	0.94	0.72	0.04	0.03	0.07	0.03	0.61	0.59	0.83	0.60
14	0.75	1.30	0.63	1.03	0.91	0.85	0.93	0.88	0.06	0.05	0.06	0.05	0.78	0.69	0.79	0.73
15	0.52	1.07	0.64	0.81	0.94	0.87	0.93	0.91	0.06	0.05	0.06	0.05	0.79	0.70	0.78	0.74
16	1.17	1.47	1.07	1.62	0.87	0.83	0.88	0.82	0.04	0.04	0.05	0.04	0.69	0.66	0.72	0.65
17	1.18	1.77	0.99	1.56	0.87	0.80	0.89	0.83	0.05	0.05	0.05	0.04	0.76	0.73	0.76	0.69
18	3.73	5.00	3.32	4.90	0.58	0.41	0.61	0.42	0.03	0.02	0.03	0.02	0.58	0.53	0.61	0.53
19	1.54	2.30	1.91	2.32	0.82	0.72	0.78	0.73	0.04	0.03	0.04	0.03	0.69	0.63	0.66	0.62
20	1.82	2.51	1.26	2.44	0.79	0.71	0.86	0.71	0.04	0.04	0.05	0.04	0.69	0.64	0.74	0.65
21	1.85	2.57	1.51	2.55	0.78	0.69	0.82	0.70	0.04	0.04	0.05	0.04	0.71	0.65	0.72	0.66
22	1.71	2.18	1.31	2.26	0.79	0.73	0.84	0.72	0.04	0.04	0.05	0.04	0.69	0.65	0.74	0.64
23	1.39	2.36	1.92	2.64	0.84	0.72	0.78	0.68	0.04	0.04	0.05	0.04	0.71	0.66	0.72	0.64
24	1.60	2.31	1.15	1.79	0.81	0.73	0.87	0.78	0.05	0.04	0.05	0.05	0.75	0.68	0.76	0.72
25	0.74	1.20	1.00	1.46	0.92	0.86	0.88	0.83	0.06	0.05	0.05	0.04	0.78	0.69	0.73	0.69
26	1.81	2.36	1.50	2.48	0.79	0.72	0.83	0.71	0.04	0.03	0.04	0.04	0.67	0.62	0.70	0.63
27	2.02	3.64	2.48	3.48	0.77	0.56	0.71	0.58	0.04	0.03	0.04	0.03	0.69	0.58	0.66	0.60
28	2.24	2.76	1.71	3.40	0.73	0.66	0.80	0.59	0.04	0.04	0.05	0.03	0.69	0.65	0.73	0.61
29	1.66	2.94	2.44	3.25	0.80	0.65	0.71	0.61	0.05	0.04	0.04	0.04	0.73	0.66	0.69	0.63
30	1.23	2.09	1.43	2.09	0.86	0.75	0.83	0.75	0.05	0.04	0.05	0.04	0.76	0.65	0.71	0.66
31	2.05	3.10	1.88	3.02	0.75	0.61	0.78	0.62	0.04	0.03	0.05	0.03	0.65	0.59	0.73	0.59
32	0.85	1.36	1.16	1.66	0.90	0.84	0.87	0.81	0.05	0.04	0.05	0.04	0.73	0.71	0.75	0.66

33	1.14	1.78	0.82	1.17	0.87	0.80	0.91	0.87	0.05	0.04	0.05	0.05	0.75	0.66	0.76	0.73
34	0.96	1.35	1.10	1.56	0.89	0.84	0.88	0.83	0.06	0.04	0.05	0.05	0.77	0.70	0.74	0.69
35	1.21	2.44	2.11	2.38	0.86	0.71	0.75	0.72	0.04	0.03	0.03	0.03	0.70	0.62	0.64	0.62

4.2.2 Textural Analysis by LBP Methodology

LBP is a mathematical operator which is commonly used for texture classification. The LBP of a particular pixel is calculated by considering only the sign of the difference of gray levels of that pixel with the defined surrounding pixels. The primary attribute of LBP, i.e., gray level invariance can be mathematically derived as given below [148].

Let $I(x,y)$ be a two dimensional monochrome image where g_c is the gray level of an arbitrary pixel (x,y) given by $g_c = I(x,y)$. Similarly g_p be the gray level of a sampling point in a circular neighborhood with P samples and radius R around the point (x,y). So it can be written as

$$g_p = I(x_p, y_p) \text{ where } p = 0,...P-1; \tag{4.1}$$

$$x_p = x + R\cos(2\pi p / P), \tag{4.2}$$

$$y_p = y - R\sin(2\pi p / P). \tag{4.3}$$

It is known that local texture of image $I(x,y)$ depends on the joint distribution of the gray values of $P+1$ $(P>0)$ pixels. That is,

$$T = t(g_c, g_0, g_{1,} g_{2,}..g_{P-1}). \tag{4.4}$$

Now the central pixel which in this case is the arbitrary pixel can be subtracted from each member of neighborhood without any loss of information as mentioned below.

$$T = t(g_c, g_o - g_c, g_1 - g_c, g_2 - g_c, ..., g_{p-1} - g_c). \tag{4.5}$$

As g_c is independent of $g_p - g_c$, the above equation can be further simplified as

$$T \approx t(g_c)t(g_0 - g_c, g_1 - g_c, g_2 - g_c, ...g_{P-1} - g_c) \tag{4.6}$$

where $t(g_c)$ denotes intensity distribution of $I(x,y)$ and carries no useful information in the context of textural pattern. But the second factor of the above expression can be exploited to represent the local texture pattern by considering the signs as mentioned below.

$$t(s(g_0 - g_c), s(g_1 - g_c), s(g_2 - g_c), ...s(g_{P-1} - g_c)) \tag{4.7}$$

such that

$$s(z)=1 \quad \text{for } z\geq 0, \tag{4.8}$$

$$s(z)=0 \quad \text{for } z<0. \tag{4.9}$$

In general, LBP is obtained from the joint distribution mentioned by the Equations 4.8 and 4.9. The basic LBP is found by adding the thresholded differences being multiplied by powers of 2 as given below.

$$LBP_{P,R}(x_c,y_c)=\sum_{P=0}^{P-1}s(g_p-g_c)2^P \tag{4.10}$$

The physical significance of Equation (4.10) is that the signs of differences within a defined neighborhood is represented by a P-bit number which results in 2^P different values for LBP code. The other attribute of LBP is rotational invariance achieved by clockwise rotating the set of neighbor pixels. The number of rotations varies till the maximum number of most significant bits in the binary pattern is zero. Mathematically,

$$LBP^{ri}_{P,R} = \min\{ ROR(LBP_{P,R}, i)\} \text{ for } i = 0,1,2,3,\ldots P-1. \tag{4.11}$$

Here, "$ROR(x,i)$ denotes the circular bitwise right rotation of bit sequence x by i steps" [135]. In our work we have found the LBP of both the Darier and non-Darier disease skin images and store the information in the form of histograms. Later the histograms of the two types of skin images are used to create the input and target databases which are given to FNN for Darier disease detection.

4.2.3 Texture Analysis by Wavelet Methodology

Each of the two dimensional discrete wavelet transforms (DB, DM, SY, BO) decomposes the skin image into one coarse approximate subband and three detail subbands with the help of low pass and high pass filters respectively as already shown in Figure 3.9. The approximation subband so obtained is decomposed twice to result in one approximation and three detail subbands at each level of decomposition. The four subbands - approximation suband, detail horizontal subband, detail vertical subband and detail diagonal subband generated after 1st level of decomposition are represented by the coefficient matrices given by A _1, D_H_1, D_V_1 and D_D_1. As each of the matrices contains too many coefficients, individual matrix is replaced by the average of the coefficients which can be expressed from [26] as

$$D\_H\_1 = \frac{1}{p \times q} \sum_{x=\{p\}} \sum_{y=\{q\}} |D\_H\_1(x, y)| \tag{4.12}$$

$$D\_V\_1 = \frac{1}{p \times q} \sum_{x=\{p\}} \sum_{y=\{q\}} |D\_V\_1(x, y)| \tag{4.13}$$

$$D\_D\_1 = \frac{1}{p \times q} \sum_{x=\{p\}} \sum_{y=\{q\}} |D\_D\_1(x, y)| \tag{4.14}$$

The coefficients of A_1 are not averaged since it undergoes further decomposition. The squaring based energy of the three detail subbands (matrices) can be obtained from Equations (4.12), (4.13) and (4.14) as

$$E\_D\_H\_1 = \frac{1}{p^2 \times q^2} \sum_{x=\{p\}} \sum_{y=\{q\}} (D\_H\_1(x, y))^2 \tag{4.15}$$

$$E\_D\_V\_1 = \frac{1}{p^2 \times q^2} \sum_{x=\{p\}} \sum_{y=\{q\}} (D\_V\_1(x, y))^2 \tag{4.16}$$

$$E\_D\_D\_1 = \frac{1}{p^2 \times q^2} \sum_{x=\{p\}} \sum_{y=\{q\}} (D\_D\_1(x, y))^2 \tag{4.17}$$

Hence, the total energy of the three detail subbands related to 1st level decomposition can be expressed as ED1 where

$$ED1 = E\_D\_H\_1 + E\_D\_V\_1 + E\_D\_D\_1 \tag{4.18}$$

Similarly ED2 and ED3 can be computed for the 2nd and 3rd decomposition levels. The approximation subband energy EA of the 3rd (last) decomposition level is obtained in a similar way as E_D_H_1 is computed from Equations 4.12 and 4.15; Like GLCM or LBP based methodologies, input and target databases are also created to provide the FNN for image classification.

4.2.4 Theory on Neural Network

The neural network is a processor which consists of a large number of parallel computation units called neurons [42]. The FNN illustrated in Figure 4.4 is the first neural network where the information flows in one direction, i.e., from the input to the output node via the hidden nodes [42], [63]. The hidden nodes are optional as in the case of a single layer perceptron which has no hidden node. This neural network which is also a popular classifier gains knowledge of a given problem by learning. The learning process refers to the adjustment of weights and bias of the neural network by the stimuli of the environment. The learning process is generally categorized as supervised ("with teacher") learning and unsupervised ("without

teacher") learning. In the supervised learning process, a predefined training dataset T having matched input-output examples is available and can be expressed from [42] as

$$T = \{(\mathbf{x}_i, d_i)\}_{i=1}^{N} \tag{4.19}$$

where $\mathbf{x}_i$ = input vector of i^{th} example, d_i = desired output of i^{th} example, N = size of sample. For training sample T, it is required to evaluate the free parameters of the network so that the actual output y_i caused due to the input x_i is close to desired output d_i for all values of *i*. The mean square error given by

$$E(n) = \frac{1}{N}\sum_{i=1}^{N}(d_i - y_i)^2 \tag{4.20}$$

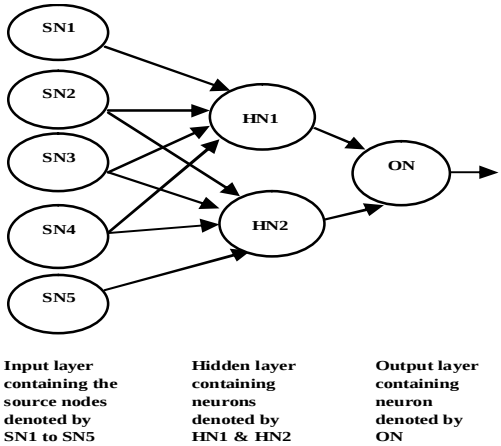

Figure 4.4 Schematic of Feedforward neural network with the input, hidden and output layers [54].

is used as the performance indexing parameter of the network. The unsupervised learning methodology utilizes the neurobiological concepts like competitive learning and Hebbian learning [53] to adjust the synaptic weights. Hebbian learning states that the variation in synaptic weight Δw_{ji} of a given neural network is defined as

$$\Delta w_{ji} = \eta x_i y_i \tag{4.21}$$

where η = learning rate, x_i = input (presynaptic) signal, y_i = output (postsynaptic) signal. The supervised training is found in multilayer perceptron and radial-basis function networks. And the unsupervised training is followed in Principal component analysis networks and self organizing maps.

The FNNs are non-linear and static networks. But they can be made dynamic networks by adding memory element in the input layer. The FNN used here is based

on the back propagation algorithm which has two distinct phases called the forward and the backward phases. During the forward phase, the network weights and bias remain fixed and the input signal passes from one layer to the other in the forward direction until an error signal is computed. According to [42], the error signal is given by

$$e_i = d_i - y_i \tag{4.22}$$

where d_i implies the desired output and y_i denotes the actual output of the network caused due to input x_i. During the backward phase the error signal propagates in the backward direction of the network given in Figure 4.4. The weights and the bias are adjusted to reduce the error e_i.

4.2.5 Darier Disease Skin Image Detection by Neural Network (FNN)

It is already shown in Figure 4.3 that each of the three methods of Darier disease investigation has FNN as the last stage. The FNN is formulated on the basis of conjugate gradient back propagation algorithm. It has three layers namely the input layer, the hidden layer and the output layer. Here the hidden layer has 20 neurons. When the texture features of all the skin images are computed by each individual method, two databases are created. The input database comprises of the characteristic features of all the input images; while the target database categories Darier and non-Darier skin images of input database as “1” and “0” in the corresponding location. That means after database creation, every method provides one input and one target database to FNN. The FFN network is trained with 70% of the input samples. The training is validated with 15% of the remaining fresh samples. And the other unused 15% samples are used for testing. So FNN detects the Darier diseases separately for three methods and the results so obtained are discussed in the following section.

4.3 Experimental Results and Discussion

The complete experiment is performed in Matlab 7.14.0.739 (R2012a). Seventy (thirty five: Darier and thirty five: non-Darier) disease skin images are taken [59]. The website [59] did not specify the image acquisition system and images are clear. The results of the Darier disease detection by FNN for individual method is represented by one confusion matrix and one performance plot.

The confusion matrix is a tabular representation of the predictions of a classifier algorithm put against its actual class. The rows of the confusion matrix represent the instances of predicted class whereas the columns represent that of actual class. The diagonal elements denote the correctly classified samples. The off-diagonal elements represent the misclassified samples. In the bottom right corner, the blue element represents the total percentage of correctly and incorrectly classified samples marked in green and red color respectively. Here, the confusion matrix for each method is a set of four confusion matrices called training, validation, testing and all confusion matrices. The training, validation and testing confusion matrices present how the neural network is trained, validated and tested by the 3 independent subsets of data from the input and target databases. And the all confusion matrix provides the disease detection accuracy and summary of the training, validation and testing matrices. The confusion matrices based on GLCM, LBP and wavelet based approaches are shown in Figures 4.5, 4.6 and 4.7 respectively.

One example showing the calculations of the entries in confusion matrix, say, All Confusion Matrix of Figure 4.5 is illustrated below. The cells of the matrix are numbered for convenience. The three cells of the top row from left to right are numbered as Cell 1, Cell 2 and Cell 3 respectively. The three cells of the middle row from left to right are Cell 4, Cell 5 and Cell 6 respectively. Similarly the cells of the bottom row from left to right are Cell 7, Cell 8 and Cell 9 respectively. The four outcomes of classification by neural network mentioned in Cell 1, Cell 2, Cell 4 and Cell 5 are TP (True Positive): 28, FP (False Positive): 6, FN (False Negative): 7 and TN (True Negative): 29. Here, TP denotes the number of predicted darier disease images which are actually darier disease images; FP denotes the number of predicted darier disease images which are actually not darier disease images; FN denotes the number of predicted non-darier disease images which are actually actually darier disease images; TN denotes the number of predicted non-darier disease images which are actually non-darier disease images. Now, the calculation of all entries from Cell 1 to Cell 9 is given below. Here, the total number of images is 70.

Cell 1: $TP = 28$

$$TP \text{ exp} ressed\ in\ percentage = \frac{28}{70} \times 100 = 40\% \tag{4.23}$$

Cell 2: $FP = 6$

$$FP \text{ exp} ressed\ in\ percentage = \frac{6}{70} \times 100 = 8.6\% \tag{4.24}$$

Cell 3: Positive Predictive Value expressed in percentage

$$\%PPV = \frac{TP}{TP + FP} \times 100 = \frac{28}{28 + 6} \times 100 = 82.35\% \approx 82.4\% \tag{4.25}$$

$$\%(1 - PPV) = (1 - .8235) \times 100 \approx 17.6\% \tag{4.26}$$

Cell 4: $FN = 7$

$$FN \text{ exp} ressed\ in\ percentage = \frac{7}{70} \times 100 = 10\% \tag{4.27}$$

Cell 5: $TN = 29$

$$TN \text{ exp} ressed\ in\ percentage = \frac{29}{70} \times 100 = 41.4\% \tag{4.28}$$

Cell 6: Negative Predictive Value expressed in percentage

$$\%NPV = \frac{TN}{TN + FN} \times 100 = \frac{29}{29 + 7} \times 100 = 80.55\% \approx 80.6\% \tag{4.29}$$

$$\%(1 - NPV) = (1 - .8055) \times 100 \approx 19.4\% \tag{4.30}$$

Cell 7: $\%Sensitivity = \frac{TP}{TP + FN} \times 100 = \frac{28}{28 + 7} \times 100 = 80\%$ (4.31)

$$\%(1 - Sensitivity) = 20\% \tag{4.32}$$

Cell 8: $\%Specificity = \frac{TN}{FP + TN} \times 100 = \frac{29}{6 + 29} \times 100 = 82.9\%$ (4.33)

$$\%(1 - Specificity) = (1 - .829) \times 100 = 17.1\% \tag{4.34}$$

Cell 9: $\%Accuracy = \frac{TP + TN}{TP + TN + FP + FN} \times 100$

$$= \frac{28 + 29}{28 + 29 + 6 + 7} \times 100 = 81.4\% \tag{4.35}$$

$$\%(1 - Accuracy) = (1 - .814) \times 100 = 18.6\% \tag{4.36}$$

where PPV is the percentage of patients with positive tests who really have darier disease. NPV is the percentage of patients with negative tests who really do not have darier disease. Sensitivity is the probability of positive tests amongst the patients having darier disease. Also, specificity is the probability of negative test amongst patients having no darier disease.

The performance plot represents three different performances- training, validation and testing of a neural network. Here performance means mean square error

Figure 4.5 Confusion matrix based on GLCM method.

Figure 4.6 Confusion matrix based on LBP method.

Figure 4.7 Confusion matrix based on wavelet method.

plotted as a function of iteration or cycle of computation of the network. Mean square error is the average of the square of the difference of the outputs and targets. So lower values of mse are preferred. The training ends when the generalization of the network is achieved. This is indicated by the increase of mse of the validation performance. Normally, the training terminates after six consecutive rises in validation error. The best performance is considered from the epoch having the minimum validation error [52]. Figures 4.8, 4.9 and 4.10 illustrate the performance plots for GLCM, LBP and wavelet based methodologies. The LBP based methodology provides the best validation performance (minimum mse) at the 11^{th} epoch.

4.4 Comparison of Works:

The Darier disease detection is hardly proposed by other authors in the light of computer aided diagnosis. So our work is not compared with earlier works. In this section, three proposed methodologies of Darier disease detection are compared.

The results of the Darier disease detection by FNN in terms of the performance indexing parameters (PIP) like percentage of correctly training, validation, testing and classification of the input skin images are compared from Figures 4.5, 4.6, 4.7 and

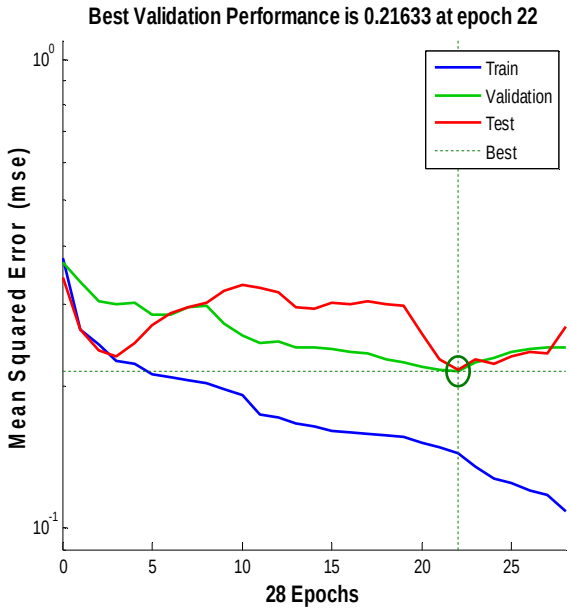

Figure 4.8 Performance plot of neural network based on GLCM method.

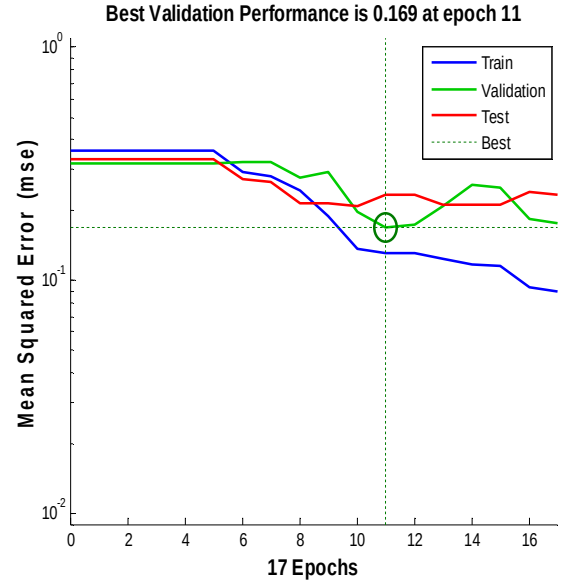

Figure 4.9 Performance plot of neural network based on LBP method.

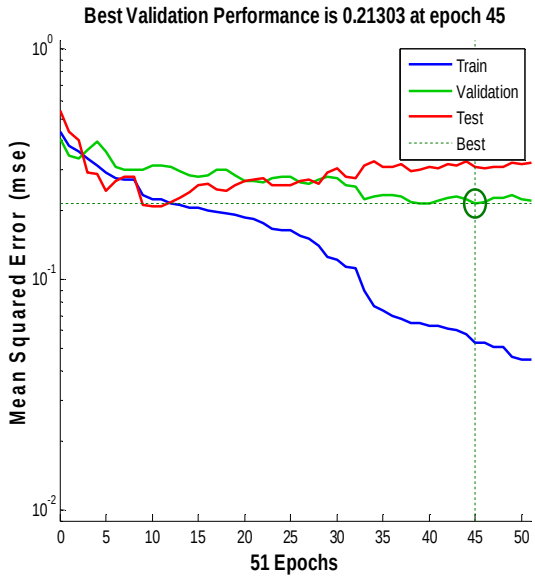

Figure 4.10 Performance plot of neural network based on wavelet method.

pictorially represented in Figure 4.11. It is found from Figure 4.11, that the wavelet based methodology of Darier disease detection is better than both GLCM and LBP based methodologies in terms of all PIP. The percentage of correctly testing the samples of GLCM and LBP methodologies by FNN is same and about 73%. The above two methodologies also provide the same Darier disease detection accuracy of about 82%. The difference of the two methodologies lies in the percentage of correctly training and validation by the FNN. Though the correct network training by GLCM methodology $(\approx 88\%)$ is better than LBP methodology $(\approx 84\%)$, LBP scheme supersedes the former in terms of correct network validation.

The Darier disease detection accuracy by GLCM method is indeed less than wavelet method. But the notable advantage of the former is its offset wise investigation of skin texture statistics. As the skin image contains typical textural variation with irregular projections or rashes along different directions, this particular aspect of textural variation is strongly captured by the statistical parameter versus offset plots. The directional offsets are varied by 8 offsets as shown in Figure 4.2 (b) along $\theta = 0^{\circ}, 45^{\circ}, 90^{\circ}\ and\ 135^{\circ}$ and the corresponding statistical parameter variations are observed in Figures 4.12- 4.15 respectively. In Figure 4.16, the offset is varied along

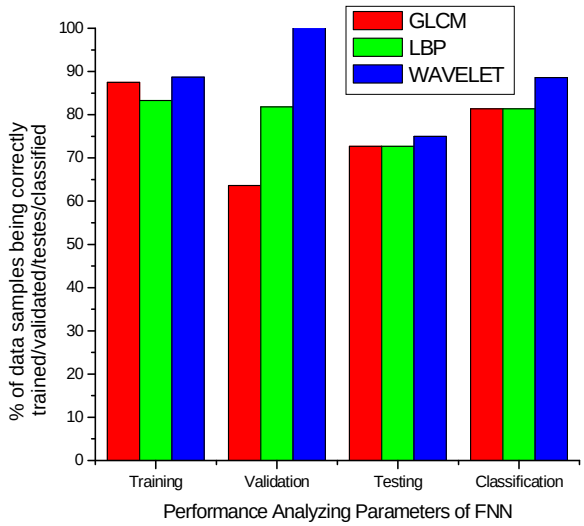

Figure 4.11 Comparison of GLCM, LBP and Wavelet based methodologies in terms of the performance indexing parameters of the neural network.

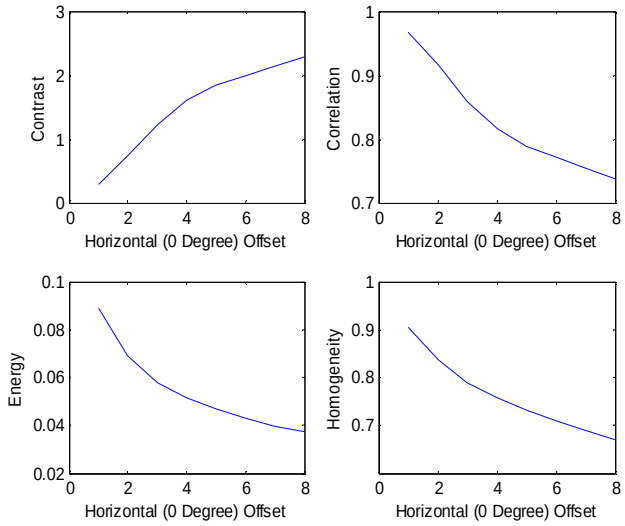

Figure 4.12 Variation of statistical parameter as a function of horizontal offset.

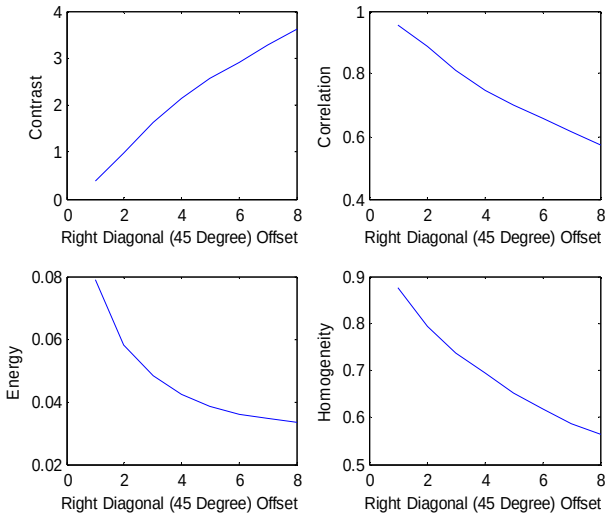

Figure 4.13 Variation of statistical parameter as a function of right diagonal offset.

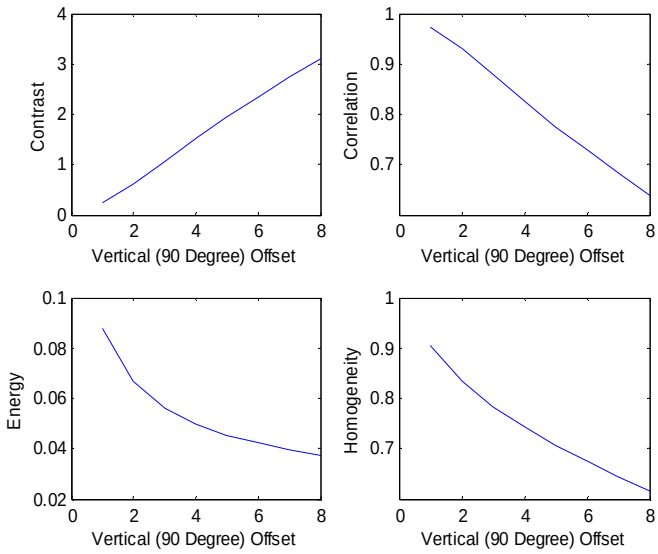

Figure 4.14 Variation of statistical parameter as a function of vertical offset.

all four directions in groups of 8 offsets defined by [0 1 to 0 8], [-1 1 to -8 8], [-1 0 to -8 0] and [-1 -1 to -8 -8] for $\theta = 0^{\circ}, 45^{\circ}, 90^{\circ}\ and\ 135^{\circ}$ respectively.

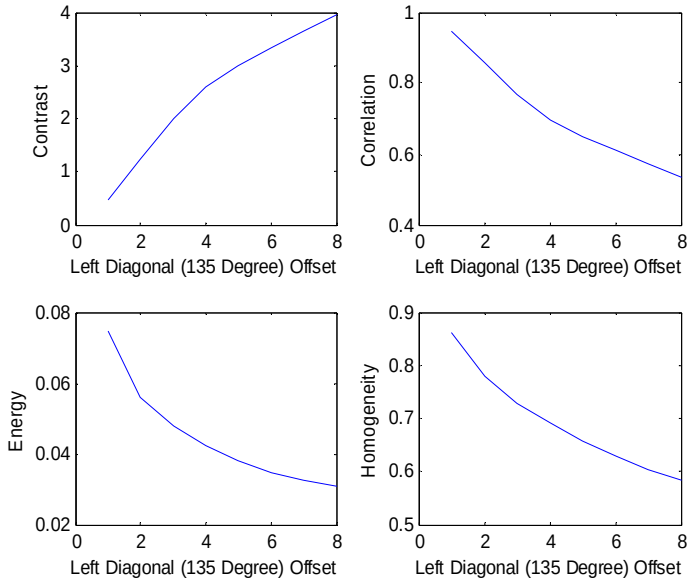

Figure 4.15 Variations of statistical parameter as a function of left diagonal offset.

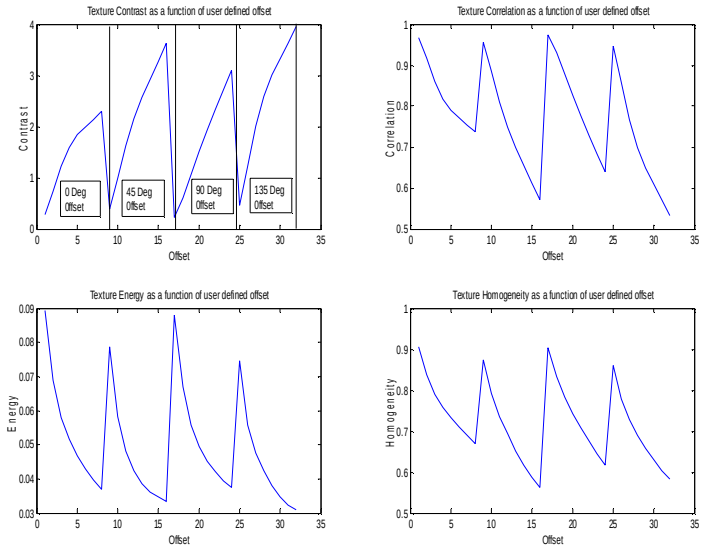

Figure 4.16 Variation of statistical parameter as a functions of multidirectional $\left(\theta = 0^{\circ}, 45^{\circ}, 90^{\circ}, 135^{\circ}\right)$ offsets. Deg: Degree. The direction wise offset partition mentioned in contrast versus offset plot (North west) holds true for the remaining plots. The subtitles of top left figure: Texture Contrast as a function of user defined offset; top right figure: Texture Correlation as a function of user defined offset; bottom left figure: Texture Energy as a function of user defined offset; bottom right figure: Texture Homogeneity as a function of user defined offset.

4.5 Conclusion

This investigation illustrates the detection of Darier disease by three different methodologies. This detection is probably the first attempt where a genetic disorder is identified by dermal imaging technique. So comparison of our result with existing algorithm is not furnished.

The empirical data reveals that wavelet based approach is better than GLCM and LBP methodologies. Though LBP and GLCM methodologies achieve exactly the same correct rate of testing and classification; but considering the correct rate of training and validation, LBP methodology is the better choice. At this juncture, what deserves mentioning is the offset based statistical plots by GLCM methodology which provides typical skin textural information along different directions of an image. In future advanced wavelet like curvelet and contourlet may be implemented to detect Darier disease.

Chapter 5

Diabetic Retinopathy Detection using Curvelet and Automated Retina Analyzer

5.1 Introduction

The segmentation of the retinal blood vessels plays an important role in the diagnosis of several life threatening diseases like cardiovascular problems, hypertension, diabetes, arteriosclerosis, glaucoma, diabetic retinopathy (DR) and so on [126], [147]. The clinical conditions are related to the morphology and functionality of the retinal vasculature. Thus, the determination of the vessel features especially the length, diameter, tortuosity, vessel count, branching pattern has become an integral part of modern ophthalmology. However, the manual inspection of the optic fundus to extract the blood vessels is time consuming and susceptible to human error due to the complex vascular arrangement and large image database of innumerous patients. As an alternative, the automated analysis of the retina images is widely accepted and practised by the ophthalmologists all over the world.

The several approaches demonstrating the automated segmentation of the retinal blood vessels can be broadly classified as tracking methods, mathematical morphology based methods, filtering methods and machine learning based algorithms. The tracking methods help to present the overall network of the blood vessels by edge

detection and subsequent marking out of the associated vessel centre lines [133]. The tracking methods can be either semi-automated or automated. In the semi-automated tracking method, the user manually chooses the initial seed point of the vessel. But in automated tracking strategy, the algorithms determine the initial seed points of the vessels. The first method is popular for coronary angiography while the second is successful for processing the retina images [118]. The mathematical morphology refers to the use of the morphological operators for the reconstruction of the vessel centre lines. Mendonca *et al.* [102] used the same to fill the extracted centre lines of the automated segmented blood vessels by the differential filters. Zana *et al.* [146] segmented the vessel-like elements from the tree shaped vascular network using the morphological operators and cross-curvature computation. The mathematical morphology is used to point out the vessel-like elements based on their morphological attributes like the linearity and continuity of individual element. Another example of morphology based segmentation was addressed by Fang *et al.* [33], where the retinal vessels are enhanced by mathematical morphology by considering their spatial properties. The vessels are differentiated from background using curvature evaluation and linear filtering. However, this leads to the loss of some important features. So Fang et al. [33] followed a reconstruction process using dynamic local region growing to recover the complete vasculature structure. The filter based methods are simple and emphasize on optimizing the response to blood vessels [147]. Considering the poor contrast of blood vessels, Chaudhuri *et al.* [17] designed the matched filter on the basis of the spatial and optical characteristics of the detectable vessel segments. The conflict of the attribute matching between the vascular and non-vascular entities was addressed by Hoover *et al.* [43] where the global attributes of the vascular network compliment the local attributes. The machine learning based algorithms are of two types – supervised and unsupervised algorithms. The supervised algorithms use predefined information whereas the unsupervised methods directly classify the data without any prior information. Such supervised algorithm using feedforward neural network (FNN) was implemented to detect the blood vessels of retina image [114]. Niemeijer *et al.* [106] introduced a vessel segmentation methodology based on pixel wise classification. An individual pixel based on its attributes is classified as vessel point or not by the k-nearest neighbor (kNN) algorithm. The performance of the three different classifiers namely linear classifier, quadratic classifier and kNN classifier are compared on a set of experiments [27].

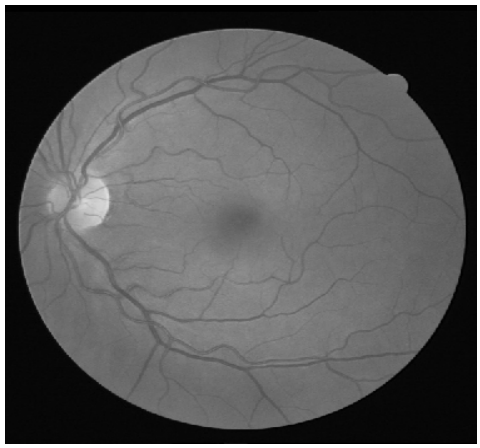

Figure 5.1 Human retina image showing non-linear blood vessels [128].

Finding the better performance of kNN classifier [27], Staal *et al.* [128] implemented the same for the vessel extraction of coloured retina images.

In this chapter, we propose the implementation of the curvelet transform to segment the retinal blood vessels which are non-linear and twisted as shown in Figure 5.1. As the curvelet transform is specially formulated to provide the sparse representation of objects having curve edges [93], and successfully implemented for retinal feature extraction [3], blood vessel segmentation [31], automated optic disk detection [32]; it is thoughtfully deployed in this investigation to extract the retinal blood vessels from the fundus image.

The novelty of this methodology is that the curvelet extracted retinal blood vessels are examined by the Automated Retinal Image Analyzer (ARIA) [7] to compute the eight retinal blood vessel features (RBVF) called (1) number of selected diameter (NDA), (2) mean diameter (MDA), (3) standard deviation of diameter (SDA), (4) minimum diameter (MNDA), (5) maximum diameter (MXDA), (6) length of vessel segment (L), (7) diameter to length ratio of vessel segment (DALR) and (8) tortuosity (TOR). It is medically approved that with the progress of DR [54], [74] there are significant changes in the RBVF. Therefore, RBVF of both the DR and non-diabetic retinopathy (NDR) images are computed to tabulate input and target databases. NDR image means retina image without DR. The two databases are provided to the neural network. Using the supervised learning algorithm discussed in Section 5.4, the neural network gets trained and validated with the databases. Then the

network detects DR images from the set of unused DR and NDR images. Therefore, this scheme synthesizes (1) curvelet transform, (2) ARIA and (3) FNN on a common Matlab platform to detect the DR images.

5.2 Diabetic Retinopathy

DR is a clinical condition of the retina caused due to the prolonged suffering of a patient from diabetes mellitus. Though the initial stage of DR does not show any noticeable symptom but mere negligence can lead to blindness. The four phases of this opthalmic disease are (1) mild non-proliferative retinopathy, (2) moderate non-proliferative retinopathy, (3) severe non-proliferative retinopathy and (4) proliferative retinopathy [54]. During the mild non-proliferative retinopathy, the minute blood vessels of the retina bulge out and some of them get blocked. As a result several parts of the retina remain undernourished. In order to supply nutrients to the affected retinal parts, new blood vessels grow along the surface of the retina and vitreous gel during the proliferative retinopathy. The thin and delicate walls of nascent blood vessels often leak blood in the central retina causing blurred vision or blindness [74]. According to the International Clinical Diabetic Retinopathy Severity Scale [66], Table 5.1 presents the different stages of DR based on the clinical conditions. The clinical changes of the vessel network caused at different stages of DR are modelled and correlated with the corresponding changes in the vessel features. The change in the vessel diameter (DM) causes change in the secondary vessel parameters like MNDA, MXDA, MDA and SDA. Similarly change in the vessel segment length (L) causes change in parameters DALR and TOR respectively. Therefore, DR is screened in the light of changed vascular morphology by measuring the changes in the above mentioned vessel parameters.

Table 5.1 Severity scale of DR.

Serial No:	Stages of DR	Ophthalmoscopic observations
1.	No DR	There is no abnormality.
2.	Mild non-proliferative retinopathy	Microaneurysms are created.
3.	Moderate non-proliferative retinopathy	More microaneurysyms are created.

4.	Severe non-proliferative retinopathy	One of the following conditions prevails. a) The number of intraretinal hemorrhages present in each of the four quadrants of the retina fundus exceeds 20. b) Particular venous beading is found in more than two quadrants of the retina fundus. c) The intraretinal microvascular abnormalities are prominent in more than one quadrant of the retina fundus.
5.	Proliferative retinopathy	Either one or both of the following conditions prevails. a) New blood vessels are created either in abnormal tissue or position of the retina fundus b)Vitreous or pre-retinal hemorrhage takes place.

5.3 Retinal Vessel Segmentation by Curvelet and Subsequent Analysis by ARIA

The fast discrete curvelet transform (FDCT) via wrapping already mentioned in Section 2.6 is applied to the retina images for the extraction of blood vessels. The algorithm of FDCT using wrapping technique consists of the following steps.

(1) Implementation of the FDCT to the retina images

(2) Curvelet Shrinkage

(3) Implementation of the inverse FDCT to reconstruct the retina images

The implementation of the FDCT to the retina images begins with the application of two dimensional fast Fourier transform (2D FFT) to the same for obtaining the Fourier samples given by $\hat{f}[n_1, n_2]$ where $-n/2 \le n_1, n_2 < n/2$. Then the product of the Fourier transform localizing window, $\tilde{U}_{j,l}[n_1, n_2]$ [16] and the Fourier samples mentioned above is found as $\tilde{U}_{j,l}[n_1, n_2]\,\hat{f}[n_1, n_2]$ for each scale j and associated angle l. The product is then wrapped around the origin to have

$$\tilde{f}_{j,l}[n_1, n_2] = W\left(\tilde{U}_{j,l}\,\hat{f}\right)[n_1, n_2] \qquad (5.1)$$

such that $0 \le n_1 < L_{1,j}$ and $0 \le n_2 < L_{2,j}$ where $L_{1,j}$ and $L_{2,j}$ are the sides of the wrapping rectangle [16]. Lastly the inverse 2D FFT is applied to each $\tilde{f}_{j,l}$ for obtaining the discrete curvelet coefficients $C^D(j,l,k)$ where the superscript D denotes "digital" and j, l, k represent the association of individual curvelet coefficient with scale, angle and position respectively. The curvelet coefficients so obtained often contain some insignificant coefficients produced due to high frequency noise. Such unimportant curvelet coefficients are removed by the process of curvelet shrinkage. The curvelet shrinkage refers to either preservation or ignorance of the individual curvelet coefficient x based on the type of defined shrinkage function S_σ (x). The commonly used shrinkage functions are soft and hard shrinkages which can be mathematically expressed from [94] as follows

$$\text{Soft shrinkage:} \qquad S_\sigma(x) = \begin{cases} x - \sigma, & x \ge \sigma \\ 0, & |x| < \sigma \\ x + \sigma, & x \le -\sigma \end{cases} \tag{5.2}$$

$$\text{Hard shrinkage:} \qquad S_\sigma(x) = \begin{cases} x, & |x| \ge \sigma \\ 0, & |x| < \sigma \end{cases} \tag{5.3}$$

where fixed threshold $\sigma > 0$. The remaining and essential curvelet coefficients are subjected to inverse FDCT to reconstruct the blood vessels segmented retinal images. Once the vessel segments are extracted by the curvelet, they are processed by ARIA.

ARIA is a freely available online software [7]. This software runs on Matlab and is successfully tested with retina images from the standard databases like DRIVE [128], REVIEW [2] and STARE [44], [56]. The functions and arguments in ARIA are image specific, i.e., some are designed for high resolution images while others are meant for low resolution. Therefore, whenever an image is selected for processing, the predefined functions are set carefully. The automated analysis of the retina images consists of two parts. The first part deals with the wavelet based segmentation of the blood vessels from the background fundus image as shown in Figure 5.2. The second

part involves the quantification of the RBVF whose output is shown at the bottom left corner of the ARIA window as displayed in Figure 5.3. The Isotropic Undecimated Wavelet Transform (IUWT) [130] is applied for vessel segmentation. The IUWT generated coefficients, W_{j+1} can be mathematically expressed from [7] as

$$W_{j+1} = C_j - C_{j+1} \tag{5.4}$$

where C_j and C_{j+1} are adjacent sets of scaling coefficients. The set of wavelet coefficients produced at each level of iteration is considered as a wavelet level. The retinal blood vessels are segmented by simply summing the wavelet levels which exhibit the highest contrast for vessels. The thresholding used for segmentation is based on a certain percentage of lowest valued wavelet coefficients. According to Starck *et al*. [130], the wavelet function is determined as the difference of two levels of resolution as mentioned below.

$$\frac{1}{4}\Psi\left(\frac{x}{2},\frac{y}{2}\right) = \varphi(x,y) - \frac{1}{4}\varphi\left(\frac{x}{2},\frac{y}{2}\right) \tag{5.5}$$

where $$\varphi(x,y) = \varphi_1(x)\phi_1(y) \tag{5.6}$$

with $$\phi_1(x) = \frac{1}{12}\left(|x-2|^3 - 4|x-1|^3 + 6\lfloor x \rfloor^3 - 4|x+1|^3 + |x+2|^3\right) \tag{5.7}$$

where $\varphi_1(x)$ is the 3rd order spline. The several post wavelet filtering steps like the implementation of connectivity constraint for edge detection are subsequently followed.

Figure 5.3 displays the screen shot of the interactive window of the ARIA software. The significance of ARIA is that most of the features can be easily accessed from this window without programming. The menus of the interactive window are File, Processors, Copy, Vessels, Retina and Display. There are also other options to calibrate and view the image. Several check boxes to display the retina image with or without centre, edge, labels, diameter and optical disk are also provided. The northeast side of the interactive window shown in Figure 5.3 provides a directory of diameters corresponding to the selected vessel segments. The southeast side of the window provides profile plot of either an individual or a group of selected vessel segments. The list of RBVF is exhibited at the southwest side of the window. This retinal image analyzer also facilitates the customization of the retinal analysis either through Graphical User Interface or writing independent code.

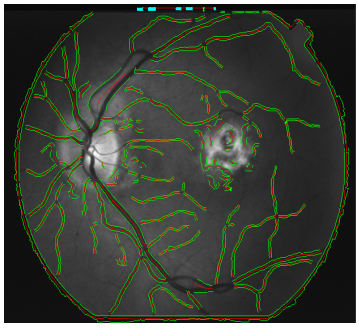

Figure 5.2 The Automated Retinal Image Analyzer processed retinal image taken from STARE database [56]. The centre lines are marked in red while the vessel edges are marked in green.

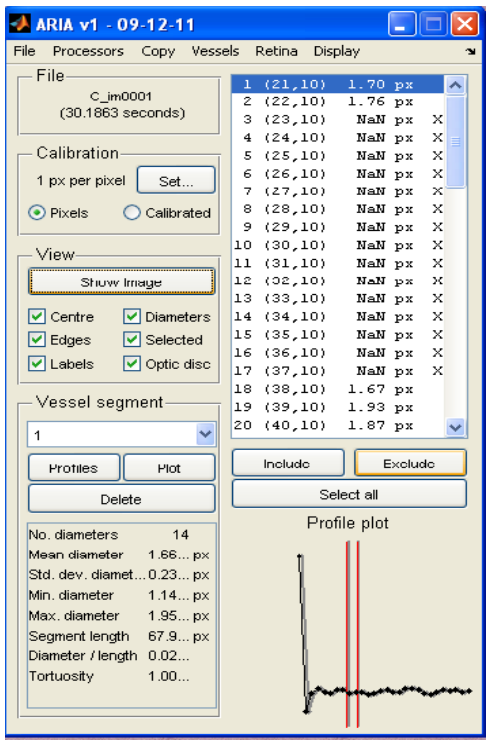

Figure 5.3 Main interactive window of Automated Retinal Image Analyzer [7].

5.4 Proposed Methodology

The complete process of DR detection by curvelet, ARIA and FNN is enumerated in this Section. The curvelet transform [58] and ARIA [7] are installed and run in Matlab. The DR and NDR images are taken from the STARE database [44], [56]. The website [56] did not specify the image acquisition system and images are clear.

Our method detects DR images from a set of input DR and NDR images as illustrated in Figure 5.4. The input images are provided to the curvelet transform. The curvelet transform segments the non-linear retinal vasculature by the FDCT, curvelet shrinkage and inverse FDCT as already discussed in Section 5.3. The curvelet transformed retina images are then provided to ARIA as shown in Figure 5.4.

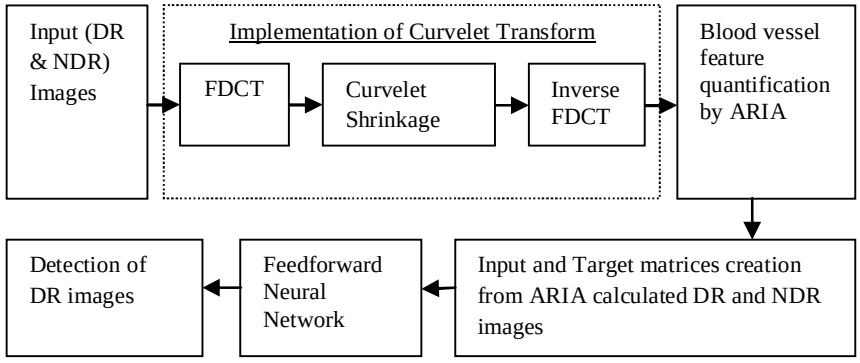

Figure 5.4 Schematic of diabetic retinopathy detection where DR: Diabetic Retinopathy, NDR: Non Diabetic Retinopathy, FDCT: Fast Discrete Curvelet Transform, ARIA: Automated Retinal Image Analyzer.

The blood vessels are again segmented by ARIA. This helps in near optimal blood vessel detection. The eight RBVF like NDA, MDA, SDA, MNDA, MXDA, L, DALR and TOR are efficiently quantified by ARIA as illustrated in Figure 5.5; Figure 5.5 represents the detailed steps represented by the block, “Blood vessel feature quantification by ARIA” in Figure 5.4. The green channel is selected for colour to grayscale conversion of retina images because it exhibits maximum contrast for vessel detection. The vessels are segmented by IUWT as explained in Section 5.3. The detected blood vessels undergo iterative morphological thinning to remove the unwanted exterior pixels. This leads to a “new binary image containing connected lines of ‘on’ pixels running along the vessel centres. The number of ‘on’ neighbours for each of these pixels is counted: end pixels (<2 neighbours) are identified, and

branch pixels (>2 neighbours) are removed" [7]. As the branches are removed, the vascular tree is divided into vessel segments which are considered for the computation of vessel diameter. This is helpful because diameters are not well defined at branches.

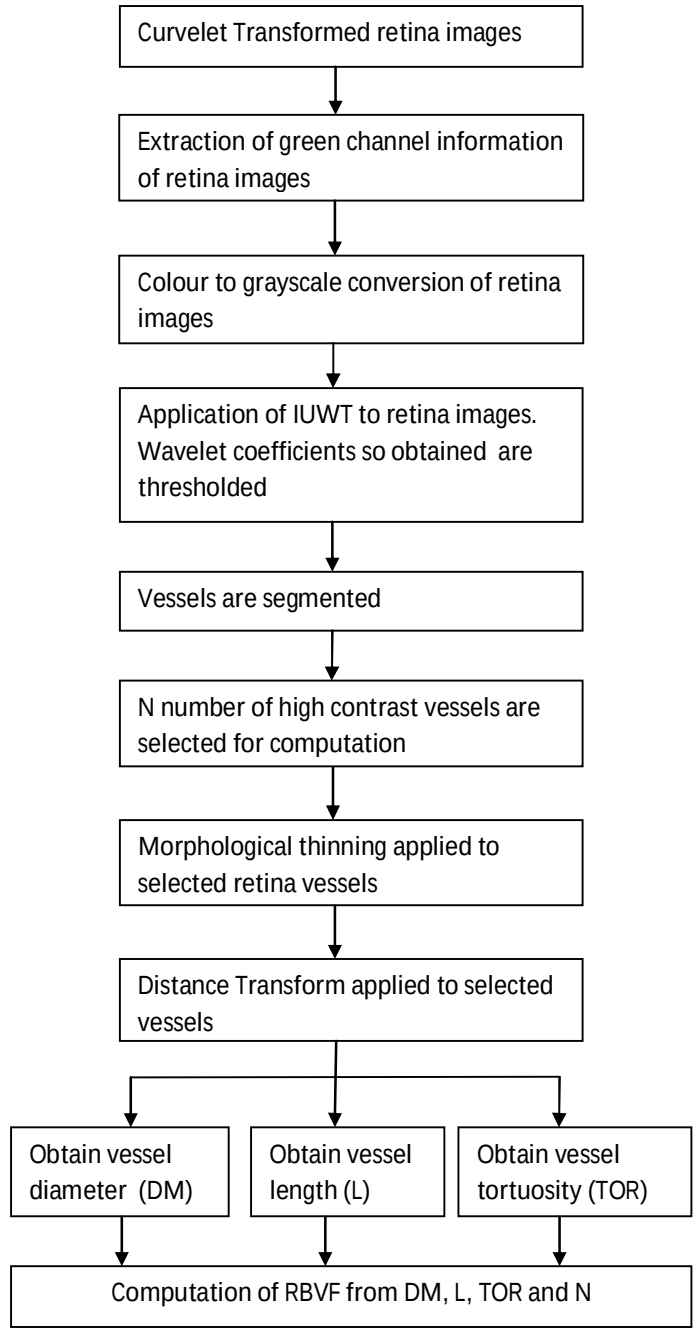

Figure 5.5 Flowchart of blood vessel feature quantification by Automated Retinal Image Analyzer where RBVF: Retinal Blood Vessel Features.

The vessel diameter is roughly calculated by taking the distance transform of the inverted binary segmented image. “This gives the Euclidean distance of every ‘vessel’ pixel from the closest non-vessel pixel, and therefore doubling the maximum value of the distance transform along the thinned centerlines provides an estimate of the diameter of every vessel segment at its widest point”[7]. The vessel segment length is calculated by summing the Euclidean distances between all points present along the centre line of a selected vessel segment. The tortuosity is obtained by dividing the vessel segment length by the Euclidean distance present between the two end points of a vessel segment. When a vessel segment is perfectly straight, tortuosity equals to 1. And for a more tortuous segment, its value is greater than 1. Therefore, the computation of the key parameters that is diameter, length, tortuosity and number of selected vessel segments helps to calculate all the RBVF. Following the flowchart of Figure 5.5, the processing of a retina image by ARIA is presented in Figure 5.6.

The two databases given by Tables 5.2 and 5.3 represent the ARIA computed vessel features of 31 DR and 31 NDR images respectively. An input matrix of 8×62 is created which represents the 62 (DR: 31 and NDR: 31) images each of which has 8 vessel features. In order to classify the input images into a set of “two” target categories, i.e., DR and NDR; a target matrix of 2×62 representing 62 images of 2 elements is also created. The “two” elements are “1” and “0” such that if the vessel features of an input matrix image is DR, it is marked as “1” else “0” in the corresponding location of the target matrix. The two matrices are provided to the FNN. The input images are randomly divided into three independent categories as training, validation and testing images. After training of FNN, it is validated to assess the generalization of the network and terminate the training process when the generalization ceases to improve. Finally, the FNN is tested with the fresh retina images to detect the DR cases.

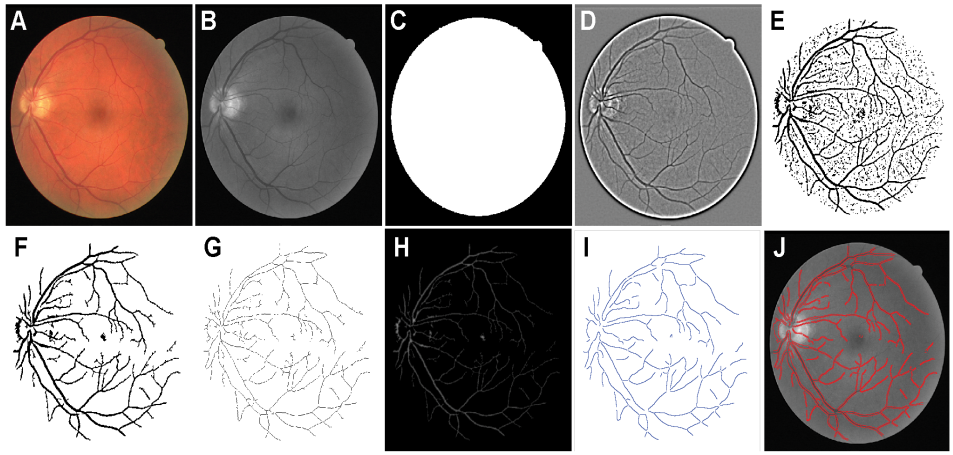

Figure 5.6 Overview of basic steps followed by ARIA to process a retina image: A. Original retina image, B. Green channel selected, C. Mask produced by thresholding, D. IUWT applied to B, E. Thresholding of wavelet coefficients, F. Removal of small objects and filling of small holes, G. Morphological thinning applied to F, H. Distance transform applied to F to compute diameters, I. Branches are removed from G and some spline fitting (mathematical function) is applied to detect centerlines. J. Edges are detected [7].

Table 5.2 The retinal blood vessel features NDA, MDA, SDA, MNDA, MXDA, L, DALR, TOR of the curvelet segmented and ARIA processed DR images.

Image No.	**NDA**	**MDA**	**SDA**	**MNDA**	**MXDA**	**L**	**DALR**	**TOR**
01	31.00	1.92	1.11	0.70	5.50	130.69	0.01	1.00
02	32.00	2.02	0.44	1.36	3.13	74.98	0.03	1.00
03	420.00	4.47	1.51	2.60	10.72	670.46	0.01	1.54
04	25.00	1.75	0.57	0.34	3.22	121.37	0.01	1.00
05	53.00	4.93	1.96	1.75	8.28	137.62	0.04	1.00
06	30.00	1.93	0.35	0.83	2.35	112.07	0.02	1.00
07	672.00	7.56	2.37	3.31	12.61	737.71	0.01	1.69
08	38.00	3.67	1.53	1.11	6.19	111.14	0.03	1.00
09	6.00	1.41	0.33	0.94	1.64	7.23	0.20	1.00
10	276.00	10.42	1.70	6.53	14.53	392.60	0.03	1.15
11	66.00	3.09	1.57	1.42	6.89	122.06	0.03	1.00
12	875.00	9.91	3.37	3.33	16.65	1370.00	0.01	88.29
13	14.00	2.28	1.74	0.77	5.46	99.82	0.02	1.00
14	55.00	5.19	1.60	1.36	7.83	112.90	0.05	1.00
15	32.00	4.21	1.16	1.84	5.73	112.41	0.04	1.00
16	4.00	9.55	0.14	9.36	9.66	2.84	3.36	1.00
17	36.00	2.53	0.95	1.20	4.04	97.31	0.03	1.00
18	409.00	8.07	3.88	3.33	17.08	425.98	0.02	1.18
19	7.00	1.21	0.55	0.54	1.73	58.15	0.02	1.00
20	22.00	7.24	1.87	4.97	10.28	21.88	0.33	1.14

21	41.00	9.16	1.89	5.78	12.04	45.82	0.20	1.02
22	15.00	11.71	1.29	10.39	13.34	14.70	0.80	1.00
23	46.00	4.11	1.01	2.78	6.30	45.65	0.09	1.07
24	15.00	7.85	1.05	6.44	9.18	21.69	0.36	1.00
25	20.00	9.52	1.22	8.27	10.86	28.30	0.34	1.14
26	46.00	9.69	1.91	7.99	13.38	47.15	0.21	1.09
27	17.00	11.02	0.94	9.82	12.29	16.92	0.65	1.16
28	83.00	7.38	3.07	4.69	15.42	102.53	0.07	1.03
29	50.00	8.56	1.09	6.98	10.86	66.83	0.13	1.09
30	56.00	15.76	1.79	13.55	18.82	55.69	0.28	1.09
31	45.00	6.69	1.62	2.75	11.13	60.60	0.11	3.54

Table 5.3 The retinal blood vessel features NDA, MDA, SDA, MNDA, MXDA, L, DALR, TOR of the curvelet segmented and ARIA processed NDR images

Image No.	**NDA**	**MDA**	**SDA**	**MNDA**	**MXDA**	**L**	**DALR**	**TOR**
01	49.00	4.48	1.61	1.03	8.47	323.06	0.01	1.00
02	17.00	2.82	0.51	1.91	3.49	22.71	0.12	1.00
03	21.00	3.65	0.34	3.38	4.61	71.46	0.05	1.01
04	3.00	2.07	0.00	2.07	2.08	1.96	1.06	1.00
05	14.00	5.49	1.17	4.17	7.89	26.02	0.21	1.00
06	2.00	1.54	0.14	1.44	1.64	0.96	1.61	1.00
07	4.00	4.06	0.78	2.91	4.54	29.55	0.14	1.00
08	15.00	3.99	0.83	3.22	5.57	13.81	0.29	1.00
09	7.00	5.41	0.05	5.35	5.50	5.85	0.93	1.00
10	109.00	11.21	3.02	5.48	15.81	281.51	0.04	1.14
11	176.00	8.60	2.63	4.70	14.90	186.74	0.05	1.03
12	3.00	1.04	0.45	0.76	1.56	11.42	0.09	1.00
13	4.00	2.18	0.23	1.90	2.44	2.92	0.75	1.00
14	9.00	2.02	1.23	0.80	4.94	94.25	0.02	1.00
15	17.00	1.87	0.95	0.30	3.27	23.62	0.08	1.00
16	31.00	2.21	0.52	1.43	3.57	110.02	0.02	1.00
17	39.00	2.29	0.66	1.44	4.19	80.05	0.03	1.00
18	25.00	2.60	0.78	1.96	4.97	135.90	0.02	1.00
19	40.00	2.90	2.08	0.99	9.11	168.56	0.02	1.00
20	5.00	2.97	0.33	2.66	3.51	4.82	0.62	1.00
21	21.00	4.07	1.57	1.53	6.22	98.89	0.04	1.00
22	5.00	1.96	0.44	1.50	2.46	74.94	0.03	1.00
23	98.00	2.58	0.33	1.72	3.72	97.37	0.03	1.06
24	6.00	1.77	0.47	0.96	2.32	21.40	0.08	1.00
25	808.00	9.90	3.52	4.08	20.00	1107.39	0.01	4.14
26	20.00	4.03	1.04	2.35	5.98	127.65	0.03	1.00
27	68.00	6.72	2.23	2.54	10.81	76.70	0.09	1.01
28	28.00	2.08	0.61	0.31	3.68	83.46	0.02	1.00
29	34.00	2.35	1.51	0.96	6.89	104.45	0.02	1.00
30	28.00	3.05	2.28	1.43	9.58	111.49	0.03	1.00
31	21.00	2.56	0.81	1.62	5.45	55.62	0.05	1.00

5.5 Experimental Results and Analysis

The DR detection accuracy of the FNN depends on its number of hidden layer neurons, N and the combination of the number of training, validation and testing images. In Figure 5.7, the variation of DR detection accuracy is observed with the variation in the number of hidden layer neurons for various combination of the number of training, validation and testing images. The number of the training images is varied from 50% to 90% (in steps of 10) of the total number of input images. The number of validation/testing images is varied (decreased) from 25% to 5% (in steps of 5) of the total number of input images. As the maximum detection accuracy of FNN is 82.3% for 70%, 15%, 15% of input images considered as training, validation and testing images respectively with N=20, the performance of the network with these constraints is illustrated by the confusion matrices and performance plot shown in Figures 5.8 and 5.9 respectively.

The literature of confusion matrix is already explained in Section 4.3. In Figure 5.8, the four confusion matrices - the Training, Validation, Testing and All confusion matrices are presented. The Training, Validation, Testing matrices present the total percentage of correctly trained, validated and tested images as 81.8%, 88.9% and 77.8% respectively. Similarly the percentage of incorrectly trained, validated and

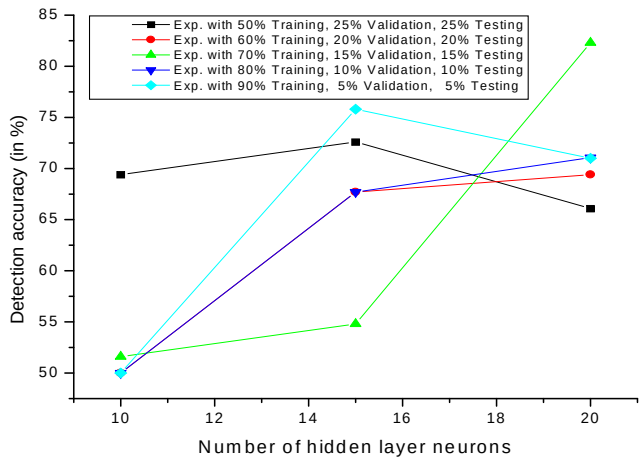

Figure 5.7 The variation of detection accuracy of DR images with the change in the number of hidden layer neurons. Here, X% Training/Validation/Testing means X% of input images considered as Training/Validation/Testing images where X: integer and Exp: Experiment .

Figure 5.8 The Training, Validation, Test and All Confusion matrices obtained from the confusion plot of the Feedforward neural network with 20 hidden layer neurons.

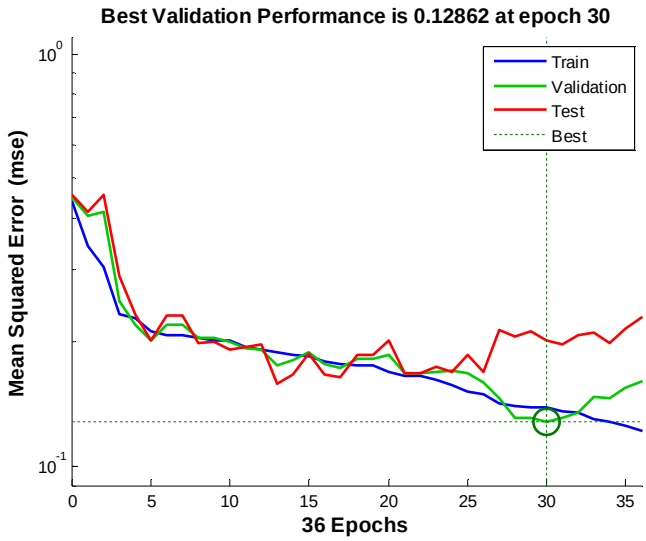

Figure 5.9 Performance plot of Feedforward neural network. The mean square error of three functions -1) training, 2) validation, 3) testing with variation in epoch is shown. The intersection of the vertical and horizontal green dotted lines with the validation curve gives the best validation performance.

tested images are 18.2%, 11.1% and 22.2% respectively. The All confusion matrix presents the percentage of correctly and incorrectly classified DR images as 82.3% and 17.7% respectively.

The performance plot also addressed in Section 4.3 presents 1) training, 2) validation and 3) test performances of the neural network in Figure 5.9. The validation and test performance plots are more or less similar till 25^{th} iteration, thereby, reducing the probability of data over fitting. The best validation performance of FNN is 0.12 which occurs at 30^{th} iteration.

Table 5.4 compares the DR detection accuracy of our work with others. The proposed detection accuracy is better than that reported in [19], [119], [145]. Cree *et al.* [19] suggested an automated retina analyzer to delineate the blood vessels present near the optic disk. After extracting the optical features from the red lesion, they are classified by the *k*- nearest neighbor algorithm. This methodology is primarily considered because it compares various methods to trace the blood vessels of the retina images. Zahlmann *et al.* [145] detected macular edema, proliferative and non-proliferative diabetic retinopathy by using thresholding techniques and Gausian filter based edge detection. Samuel *et al.* [119] demonstrated a computerized detection of non-proliferative retinopathy using three lesions namely cotton wool spots, hard exudates and microaneurysyms. Moreover, the curvelet based diabetic retinopathy grading system addressed by Alipour *et al.*[3] involves too many steps such as 1) contrast limited adaptive histogram equalization; 2) detection of 2a) optic disk, 2b) retinal vessel, 2c) exudates and 2d) micro-aneurysms, 3) foveal vascular zone detection and 4) support vector machine based classification. Our algorithm is compact, simple and easy to implement since it incorporates 3 basic steps of 1) retinal

Table 5.4 Comparison of our method with others

Authors	Proposal	Based on	Accuracy (%)
Cree et al. [19]	Automated retinal analyzer	Bayes rule	70
Zahlman et al. [145]	Situation estimation using hybrid fuzzy based image processing	Thresholding techniques and Gaussian edge detector	79
Samuel et al. [119]	Computerized detection of non-proliferative diabetic	Cotton wool spots, hard exudates and microaneurysms	81.7

	retinopathy		
Our method	Curvelet integrated automated retinal analyzer	Feedforward neural network	82.3

vessel segmentation by curvelet transform, 2) RBVF computation by ARIA and 3) FNN to detect the DR images.

The two important diagnostic parameters called sensitivity and specificity mentioned in Equations 3.19 and 3.20 are addressed here and compared with others. Figure 5.10 illustrates the pictorial comparison of sensitivity and specificity obtained from our work with that proposed by others. Sensitivity is defined as the probability of positive tests amongst the patients who have DR. On the contrary, specificity refers to the probability of negative test amongst patients who do not have DR. It is found from Figure 5.10 that percentage of sensitivity (sn) and specificity (sp) obtained from our method (sn: 81, sp: 84) are almost consistent in comparison to a wide difference from others (sn: 100, sp: 67) [78], (sn: 80.21, sp: 70.66) [124], (sn: 95.1, sp: 46.3) [138], (sn: 96.7, sp: 71.4) [85]. However, Lichode *et al.* [86] provides sensitivity and specificity with little difference. In addition, our method supersedes [78], [85], [86], [124], [138] in terms of specificity. Though the proposed sensitivity (sn: 81) is better than (sn: 80.21) [124]; it deserves further improvement. In addition, the sensitivity and specificity mentioned above can also be demonstrated by the receiver operating characteristics (ROC) curves [81].

The two other diagnostic parameters called positive predictive value (PPV) and negative predictive value (NPV) mentioned in Equations 3.21 and 3.22 are hardly addressed in the above works. PPV and NPV are evaluated in our work in order to detect DR images with clinical advantage. PPV is the percentage of patients having a positive test who really have DR. On the other hand, NPV is the percentage of patients having a negative test who really do not have DR. Here, PPV and NPV are obtained from the All Confusion Matrix shown in Figure 5.8. They can also be expressed in accordance to Equations 3.21 and 3.22 as

$$PPV = \frac{TP}{TP + FP} = \frac{25}{25 + 5} = 83.3\% \tag{5.8}$$

and

$$NPV = \frac{TN}{TN + FN} = \frac{26}{6 + 26} = 81.3\% \tag{5.9}$$

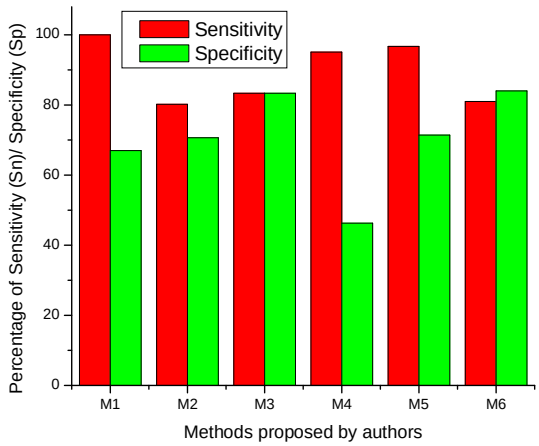

Figure 5.10 Comparison of sensitivity and specificity proposed by different authors with our work. The methods-M1, M2, M3, M4, M5 represent different authors [78], [85], [86], [124], [138], and M6 represents our method.

5.6 Conclusion

The proposed scheme successfully integrates the curvelet transform, ARIA and FNN on a common platform to detect the DR images. The retinal images are identified with an accuracy of 82.3%. The neural network is tested by varying the percentage of training (validation and testing) images and found that the maximum DR detection accuracy of 82.3% occurs at 70%, 15% and 15% of the input images considered as training, validation and testing images respectively. In other cases when the percentage of training samples is either (50-60)% or (80-90)% of the input images, the network is either under trained or overtrained leading to poor detection accuracy. In this work the several important diagnostic parameters – sensitivity, specificity, predictive positive value, negative predictive value are presented along with the DR detection accuracy.

In future, this work can be extended to detect the various stages of DR. That is, the first part of the work should detect DR image, while the second part should identify the exact stage of it like mild non-proliferative retinopathy or proliferative retinopathy. Moreover, this work can also be completed by investigating the segmentation of the retinal blood vessels by other mathematical transform like contourlet. The result so obtained can be compared with that presented here.

Chapter 6

Mammogram Denoising using Wavelet, Curvelet and other Transforms

6.1 Introduction

Breast cancer is one of the deadliest diseases that a woman suffers. Mammogram is a low energy X-ray technique used to diagnose early breast cancer. The mammogram is usually corrupted by noise mainly during acquisition. Therefore, the primary objective of mammogram denoising is to preserve the important features while filtering out the noise to the maximum extent. In the earlier days, noise was reduced by linear methods like Wiener Filtering. But linear filtering methods produce blurring effect and incomplete noise filtration. So non-linear filtering techniques like the wavelet based denoising was proposed to overcome the limitations of the linear filters. Wavelet based denoising do pretty well for images with point singularities but fail to represent objects with singularities along curves. So curvelet [13], Poisson Unbiased Risk Estimation Technique – Linear Expansion of Thresholds (PURE-LET) [91], contourlet [96] are used here along with the wavelet transform to denoise the mammogram. PURE-LET is a statistical technique specially formulated to filter Poisson noise from image. In this chapter the complete investigation on mammogram denoising is divided into three parts as i) Mammogram Denoising I, ii) Mammogram Denoising II, and iii) Mammogram Denoising III.

In Mammogram Denoising I, we denoise the mammogram by the wavelet and curvelet transforms with a motive to investigate the role of the "embedded" thresholding algorithm. In Mammogram Denoising II, curvelet transform based on three types of block thresholding are implemented to evaluate their performance and compare with curvelet based on hard thresholding (HT). Mammogram Denoising III deals with the Poisson noise removal of mammogram by wavelet, contourlet, curvelet and PURE-LET transforms.

Malar *et al.* [96] denoised mammogram by the three mathematical transforms namely wavelet, curvelet and contourlet which are based on only one type of thresholding technique called HT. As the signal to noise ratio (SNR) of the denoised mammogram depends on the type of the thresholding algorithm coded within the transform, we extend the work of Malar *et al.* [96] in i) Mammogram Denoising I, by deploying three thresholding schemes i.e., soft, hard and block thresholding under the common frame of implementation called the wavelet transform and the curvelet transform for mammogram denoising. Thus, one can compare the mammogram denoising ability of all the three thresholding techniques using the wavelet and the curvelet transforms separately. Then the performance trend of these thresholding techniques with the wavelet transform can be matched and justified with the performance trend of the same with the curvelet transform. Hence, a comparative study of the mammogram denoising based on the different thresholding techniques using wavelet and curvelet transforms is successfully completed in the first part of the investigation.

Like [96], it is also found from i) Mammogram Denoising I, that whatever be the type of thresholding adopted for mammogram denoising, the curvelet is better than the wavelet. So considering curvelet transform, it is also found that block thresholding gives better denoising for Salt and Pepper and Speckle noises. There are three types of block thresholding techniques - diagonal real thresholding (DRT), diagonal complex thresholding (DCT) and block complex thresholding (BCT). Mammogram denoising based on the three block thresholding techniques using curvelet transform is evaluated and compared with HT using the same transform. Here, HT is selected since it is only implemented by Malar *et. al* [96] to denoise mammogram. Therefore, the second part (Mammogram Denoising II) of this chapter deals with the curvelet based mammogram denoising based on HT, DRT, DCT, BCT techniques; their performance evaluation and comparison.

The third part (Mammogram Denoising III) of the investigation initiates with the observation of the peculiar trend of Poisson noise removal from mammogram by the three transforms. It is observed from [96] that Salt and Pepper, Gaussian, Speckle noise removal from mammogram by the curvelet, contourlet and wavelet transforms has the following trend.

$$SNR_{Curvelet} \rangle SNR_{Contourlet} \rangle SNR_{wavelet} . \quad (6.1)$$

But for Poisson noise removal the transforms exhibit a different trend as follows.

$$SNR_{Wavelet} \rangle SNR_{Contourlet} \rangle SNR_{Curvelet} \quad (6.2)$$

Therefore, the verification of this exceptional decreasing order of SNR for Poisson noise (Equation 6.2) and subsequent effort to improve the same is the motivation of this part of experimentation. At first we confirm the order of peak signal to noise ratio (PSNR) of the denoised mammograms by the wavelet, contourlet and curvelet transforms with the order of SNR mentioned in Equation 6.2. Here we have selected PSNR instead of SNR as a measure of denoising quality since we are not interested in the exact value of the PSNR or SNR, rather we are concerned about its increasing or decreasing order. Secondly, we apply a newly introduced denoising strategy called PURE-LET to the mammograms to improve the PSNR further.

All the three experiments are performed in Matlab with Version: 7.14.0.739 (R2012a). The mammograms are taken from MIAS database [132] and rescaled to 512×512 images. The website [132] did not specify the image acquisition system and images are clear. The online available curvelet toolbox [58], contourlet toolbox [67] and PURE-LET toolbox [68] are installed in Matlab.

6.2 Background Overview

Over the last few decades the wavelet and the curvelet transforms have played a significant role in image processing like denoising, compression, segmentation, restoration etc. Wavelet transform is popular in the denoising of the medical images specially for mammograms. A vast literature on this application is available in many research works [38], [77], [79], [131], [140]. Wang et al. [140] identified microcalcification in mammogram by applying wavelet based subband image decomposition. As microcalcification matches the high frequency components of the image the detection becomes easy by first filtering out the low frequency component and reconstructing the output mammogram from only the high frequency subbands.

Jamarani *et al*. [77] used wavelet based decomposition for the detection of microcalcification in digital mammograms but later took the help of Artificial Neural Network (ANN) for its classification. Another very recent work on the detection and classification of cancerous and noncancerous tissues in digital mammogram was suggested by Görgel *et al*. [38]. Their investigation consists of four steps of homomorphic filtering, selection of region of interest by Local Seed Region Growing (LSGR) algorithm, implementation of Spherical Wavelet Transform and classification by Support Vector Machine (SVM). Despite innumerous applications of discrete wavelet transform, it suffers from shift sensibility due to the down-sampling, poor directionality and lack of phase information. Keeping this in mind, Alarcon-Aquino *et al.* [1] have rightly proposed the detection of microcalcification using dual-tree complex wavelet transform (DT-CWT) with better phase information, directional selectivity, shift invariance and limited redundancy. Eltoukhy *et al*. [30] compared the wavelet transform with the curvelet transform for the diagnosis of breast cancer and experimentally found that curvelet transform surpasses the wavelet transform in the detection of malignant lesions. The wavelet transform when combined with curvelet transform to reduce noise in image [45] gives optimal results as compared to using them separately. Tsai *et al*. [134] reported a mammogram visual quality improvement method based on undecimated wavelet transform and its coefficient mapping. Like the wavelet transform, the curvelet transform is also widely used in mammogram denoising [97].

6.3 Mammogram Denoising I: Soft, Hard and Block Thresholding Techniques for Mammogram Denoising

The main aim of image denoising is to remove/reduce the noise and to obtain an approximation of the original image which gives the minimum mean square error (MSE). The process of mammogram denoising shown in Figure 6.1 refers to the application of the transform to the noisy mammogram followed by the thresholding of the transform generated coefficients and the implementation of the inverse transform. As the philosophy of the denoising method remains the same for both the wavelet and the curvelet transforms [18], [94] we have discussed the thresholding techniques in the context of the “mother” wavelet.

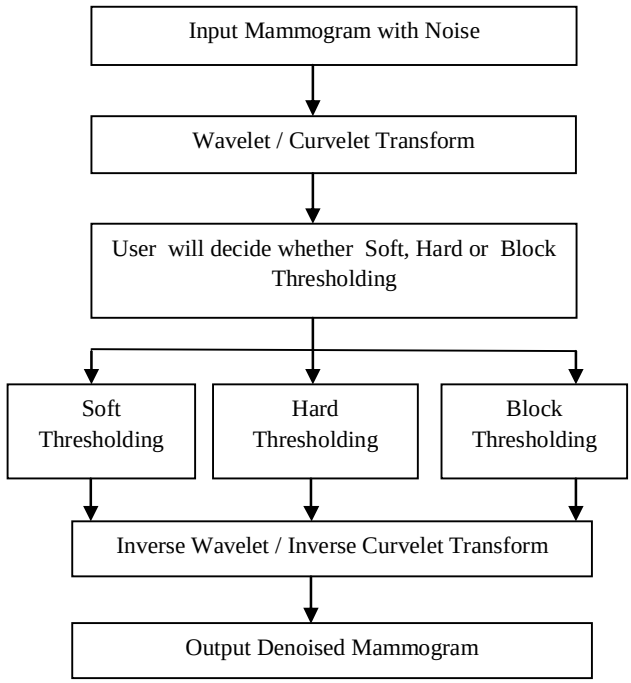

Figure 6.1 Block diagram representation of mammogram denoising by the wavelet or curvelet transform based on soft, hard and block thresholding techniques [116].

First of all the wavelet transform is applied to the mammogram with different types of noise in order to denoise the same in the transform domain resulting in the generation of discrete wavelet coefficients. Secondly, the thresholding technique is applied to these empirical coefficients to remove the insignificant coefficients primarily caused due to the noise from the significant ones representing the mammogram features. Thus, noise is attenuated in this step. Indeed, thresholding is very active due to the non-linear sparse representation of the noisy mammograms by the wavelet transform. Finally, the inverse wavelet transform is applied to the thresholded coefficients to get back the noise free mammogram. Soft and hard thresholding rules are basically term-by-term comparison method whereas the block thresholding refers to a “group” phenomenon explained below.

6.3.1 Soft Thresholding

Here, the wavelet coefficients whose absolute values are lower than threshold are set to zero and the non-zero coefficients are modified according to the following condition. The soft thresholding function [18], [94] can be written as

$$\delta_{\lambda}^{s}(d_{jk}) = \begin{cases} 0, & for \quad |d_{jk}| < \lambda \\ d_{jk} - \lambda, & for \quad d_{jk} \geq \lambda \\ d_{jk} + \lambda, & for \quad d_{jk} \leq \lambda \end{cases} \tag{6.3}$$

where d_{jk} represents the wavelet coefficient at the j^{th} decomposition level with k being the index of the coefficient at that level and λ is the threshold level. Soft thresholding produces visually satisfactory images than the hard thresholding.

6.3.2 Hard Thresholding

It refers to the retention of the wavelet coefficient if the absolute value of the coefficient is either greater than or equal to the threshold value. On the other hand if the absolute value of the coefficient is lesser than the threshold, it is simply set to zero. Thus the hard thresholding function [18], [94] can be written as

$$\delta_{\lambda}^{H}(d_{jk}) = \begin{cases} 0, & for \ |d_{jk}| < \lambda \\ d_{jk}, & for \ |d_{jk}| \geq \lambda \end{cases} \tag{6.4}$$

where d_{jk} represents the wavelet coefficient at the j^{th} decomposition level with k being the index of the coefficient at that level and λ is the threshold level. When noise is sufficiently strong in the images hard thresholding produces sudden artifacts in the denoised images.

6.3.3 Block Thresholding

Once the wavelet coefficients are generated by the application of the wavelet transform to the noisy mammogram, block thresholding introduced by Hall *et al.* [39], [40] divides the empirical wavelet coefficients into groups or blocks. As wavelet transform is a multiresolution transform, therefore at each resolution level j the wavelet coefficients $\tilde{y}_{j,k}$ are divided into blocks which do not overlap and have length L. The indices of the wavelet coefficients present in the b^{th} block at j^{th} resolution

level is given by jb. The sum of the squares of the experimentally generated wavelet coefficients denoted by S_{jb}^2 is expressed as

$$S_{jb}^2 = \sum_{k \in (jb)} \tilde{y}^2{}_{j,k} \tag{6.5}$$

Now, the block thresholding rule implies that if S_{jb}^2 is greater than the threshold T, the block jb with all the wavelet coefficients present in it is preserved; else the block with its coefficients is rejected. Mathematically, the block thresholding can be represented from [10] by

$$\hat{\theta}_{j,k} = \tilde{y}_{j,k} . I(S_{jb}^2 > \mathrm{T}) \quad \text{for (j,k)} \in \text{(j,b)} \tag{6.6}$$

This method offers high estimation precision than the term by term thresholding because it utilizes the information of all the constituent wavelet coefficients within a given block.

6.3.4 Experimental Results and Discussion

Different types of noise called Salt and Pepper, Poisson, Gaussian and Speckle are added to the mammograms. The simulation is validated by the proposal of Naveed *et al.* [105] being tested on Salt and Pepper noise present in mammogram. The other types of noise present in the mammogram are evident in the reports [96], [97]. Salt and Pepper noise with noise density of 0.05, Gaussian white noise with zero mean and 0.01 variance, multiplicative Speckle noise with zero mean and 0.04 variance are added to the mammograms for experimental purpose. Once the noises are added to the mammograms they are denoised by the biorthogonal wavelet and discrete curvelet transforms [111]. The wavelet and curvelet denoised mammograms by soft, hard and block thresholding techniques for Salt and Pepper, Poisson, Gaussian and Speckle noises are shown in Figure 6.2 to Figure 6.9 respectively. Table 6.1 presents the average signal to noise ratio of twenty mammograms with different types of noise; subjected to soft, hard and block thresholding techniques based wavelet and curvelet transforms. When compared amongst the three thresholding methods with the wavelet transform as shown in Table 6.1 and Figure 6.10, the block thresholding outperforms the soft and hard thresholding techniques for Salt and Pepper, Gaussian and Speckle noises. A similar comparison shown in Table 6.1 and Figure 6.10 is carried out amongst the three thresholding techniques of the curvelet transform and found that the

block thresholding yields higher SNR than soft and hard techniques for Salt and Pepper noise and Speckle noise too. The interesting and notable point is, that whatever be the type of the transform used, the hard thresholding denoises the mammogram better than the soft and block thresholding for Poisson noise exclusively. Finally, the denoising performance of the soft, hard and block thresholding using wavelet and curvelet for all the four types of noise is plotted simultaneously in Figure 6.10 and found that irrespective of the selected thresholding methodology the curvelet transform is better than the wavelet transform.

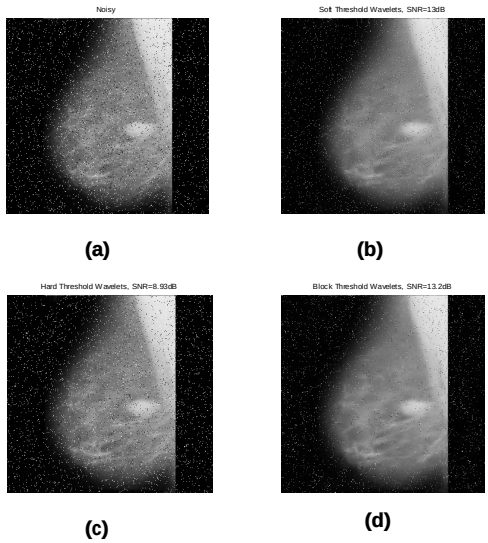

Figure 6.2 (a) Noisy mammogram with Salt and Pepper noise; Denoised mammograms by (b) Soft Threshold Wavelet (c) Hard Threshold Wavelet (d) Block Threshold Wavelet.

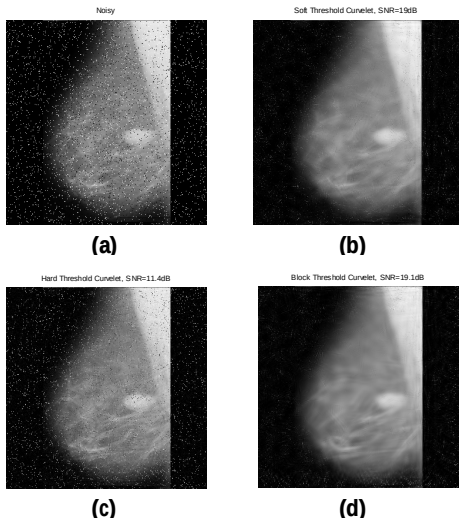

Figure 6.3 (a) Noisy mammogram with Salt and Pepper noise; Denoised mammograms by (b) Soft Threshold Curvelet (c) Hard Threshold Curvelet (d) Block Threshold Curvelet.

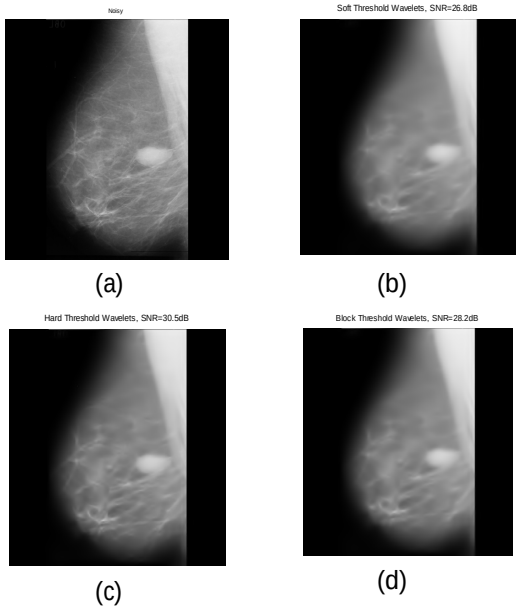

Figure 6.4 (a) Noisy mammogram with Poisson noise; Denoised mammograms by (b) Soft Threshold Wavelet (c) Hard Threshold Wavelet (d) Block Threshold Wavelet.

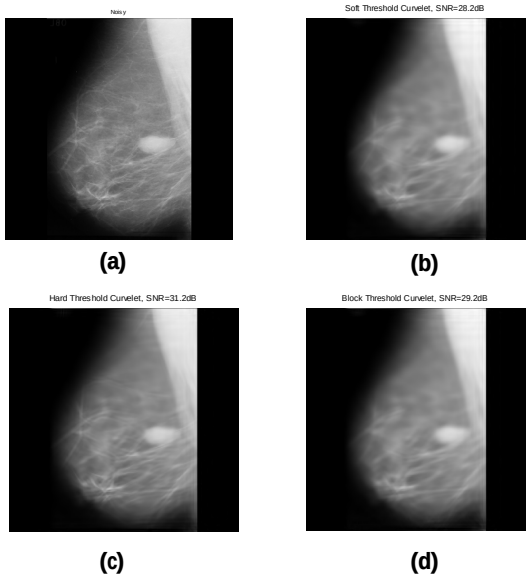

Figure 6.5 (a) Noisy mammogram with Poisson noise; Denoised mammograms by (b) Soft Threshold Curvelet (c) Hard Threshold Curvelet (d) Block Threshold Curvelet.

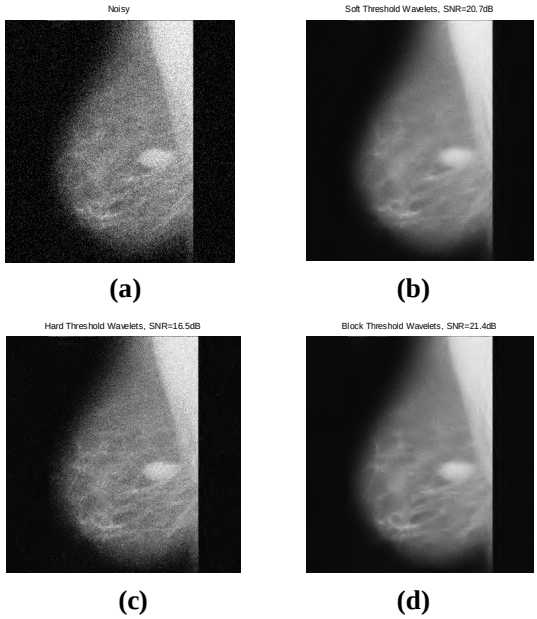

Figure 6.6 (a) Noisy mammogram with Gaussian noise; Denoised mammograms by (b) Soft Threshold Wavelet (c) Hard Threshold Wavelet (d) Block Threshold Wavelet.

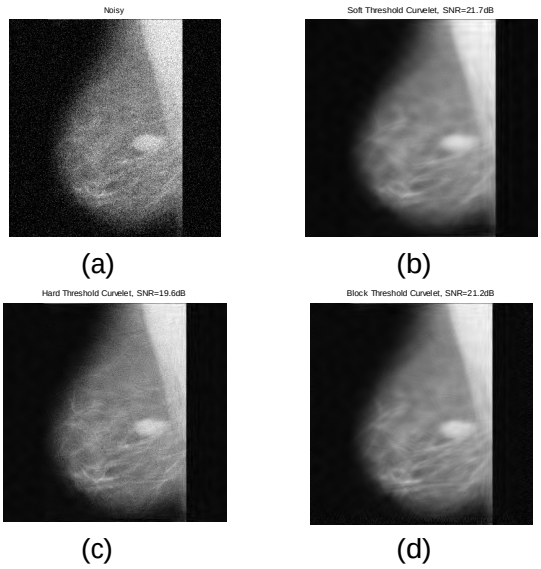

Figure 6.7 (a) Noisy mammogram with Gaussian noise; Denoised mammograms by (b) Soft Threshold Curvelet (c) Hard Threshold Curvelet (d) Block Threshold Curvelet.

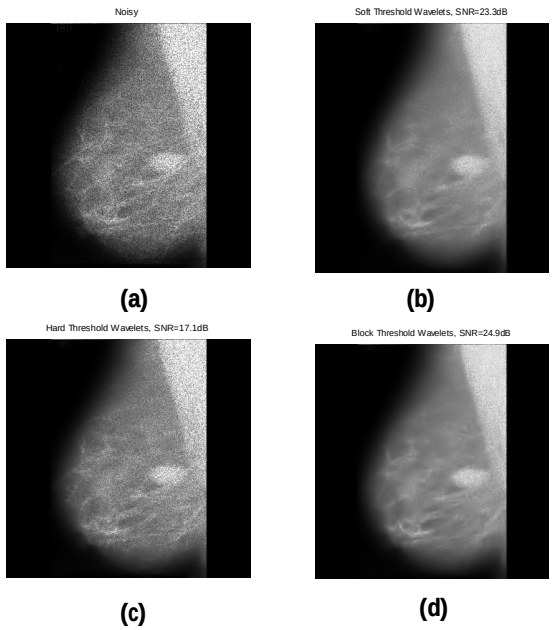

Figure 6.8 (a) Noisy mammogram with Speckle noise; Denoised mammograms by (b) Soft Threshold Wavelet (c) Hard Threshold Wavelet (d) Block Threshold Wavelet.

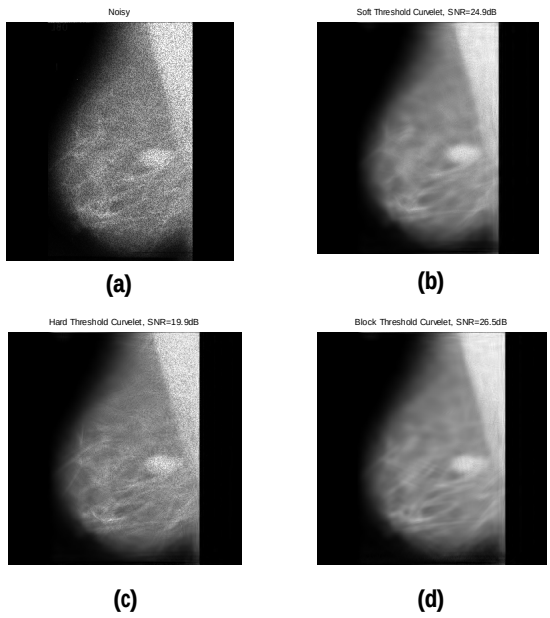

Figure 6.9 (a) Noisy mammogram with Speckle noise; Denoised mammograms by (b) Soft Threshold Curvelet (c) Hard Threshold Curvelet (d) Block Threshold Curvelet.

Table 6.1 The average SNR (db) of the Soft, Hard and Block thresholding techniques based wavelet and curvelet transform denoised mammograms for different types of noise.

Types of Noise	**Denoising by Wavelet Transform**			**Denoising by Curvelet Transform**		
	Soft Threshold (SNR in db)	Hard Threshold (SNR in db)	Block Threshold (SNR in db)	Soft Threshold (SNR in db)	Hard Threshold (SNR in db)	Block Threshold (SNR in db)
Salt and Pepper	13.14	9 .01	13.20	19.08	11.36	19.20
Poisson	27.94	31.76	29.36	29.18	32.42	30.42
Gaussian	21.10	17.10	21.66	21.98	20.06	21.44
Speckle	23.22	17.20	24.92	24.72	19.92	26.24

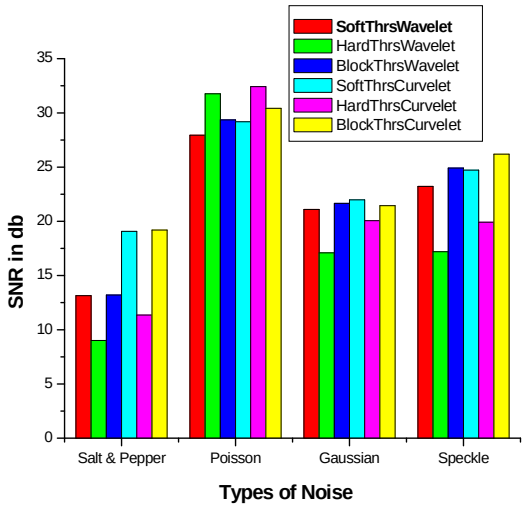

Figure 6.10 Comparison of the average SNR obtained by applying soft, hard and block thresholding techniques based on wavelet and curvelet transform to mammograms with different types of noise.

6.4 Mammogram Denoising II: Using Curvelet Transform Based on Three Different Block Thresholding Techniques

Due to the different trend of Poisson noise removal by wavelet, contourlet and curvelet transforms (Equation 6.2), it is dealt separately in Section 6.5. In this section, we first denoise the mammograms with Salt and Pepper, Gaussian and Speckle noises by the curvelet transform based on the traditional HT. Then we denoise the mammograms by the curvelet transform but based on three block thresholding techniques - DRT, DCT and BCT. The meaning of DRT, DCT and BCT can be understood from the nomenclature and also briefed in [58]. For example, DCT refers to the information based thresholding which considers the fast discrete curvelet transform (FDCT) generated complex curvelet coefficients located along the diagonal of the curvelet coefficient matrix [113]. We compare the denoising performance of the conventional HT algorithm with the non-conventional block thresholding algorithms (DRT/DCT/BCT). The denoising performance of all the thresholding algorithms (HT, DRT, DCT, BCT) are plotted as a function of noise standard deviation to demonstrate the noise sensitivity.

The mammogram denoising by the curvelet transform illustrated in Figure 6.11 is divided as the application of the forward FDCT to the noisy mammogram, curvelet thresholding and implementation of inverse FDCT to the thresholded curvelet coefficients. In Figure 6.11 the two dimensional fast Fourier transform (2D FFT) is applied to the input noisy mammogram to get the Fourier samples given by $\hat{f}[n_1, n_2]$ where $-n/2 \le n_1, n_2 < n/2$. The product of $\tilde{U}_{j,l}[n_1, n_2]\ \hat{f}[n_1, n_2]$ is obtained for each scale j and angle l where $\tilde{U}_{j,l}$ represents the curvelet frequency window [16]. The above product is wrapped around the origin to get $\hat{f}_{j,l}[n_1, n_2] = W(\tilde{U}_{j,l}\ \hat{f})[n_1, n_2]$ with $0 \le n_1 < L_{1,j}$ and $0 \le n_2 < L_{2,j}$ where $L_{1,j}$ and $L_{2,j}$ are the dimensions of the rectangle used for wrapping data [16]. The two dimensional inverse fast Fourier transform (2D IFFT) is applied to each $\hat{f}_{j,l}[n_1, n_2]$ in order to obtain the discrete curvelet coefficients $C^D(j,l,k)$ where superscript D represents "Digital" and (j,l,k) represent the association of individual curvelet coefficient with scale, angle and position respectively. When the curvelet coefficients are generated, the insignificant coefficients caused by noise are removed by the thresholding algorithms. The inverse FDCT is applied to the thresholded curvelet coefficients to reconstruct the denoised mammogram.

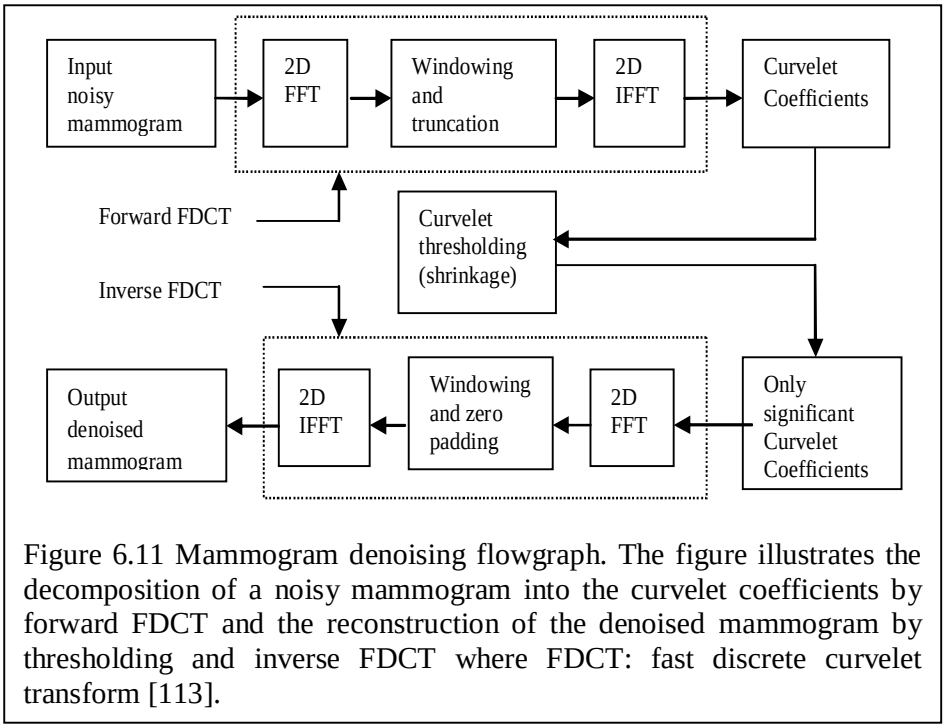

Figure 6.11 Mammogram denoising flowgraph. The figure illustrates the decomposition of a noisy mammogram into the curvelet coefficients by forward FDCT and the reconstruction of the denoised mammogram by thresholding and inverse FDCT where FDCT: fast discrete curvelet transform [113].

6.4.1 Experimental Results and Discussion

The Salt and Pepper, Gaussian, Speckle noises are added to the mammogram and denoised by the HT, DRT, DCT and BCT. The denoising results are presented in Table 6.2. The denoised mammograms by the HT, DRT, DCT, BCT for all the mentioned noises are shown in Figures 6.12 to 6.14 respectively. It is found from Table 6.2 that for Salt and Pepper and Gaussian noises, the curvelet denoising based on block thresholding technique gives better performance than conventional HT. Interestingly, for Gaussian noise DRT gives satisfactory result than HT but the noise filtration by DCT, BCT and HT are more or less the same.

It is well known that the curvelet denoising performance is dependent on the noise level. As presented in Tables 6.3 to 6.5, the noise standard deviation is varied from 10 to 60 to compare the curvelet denoising methodologies (HT, DRT, DCT, BCT) for the above mentioned noises. The PSNR versus standard deviation for Salt and Pepper, Gaussian and Speckle noises are shown in Figures 6.15 to Figure 6.17 respectively with the following observations.

- For the fixed range of standard deviation (10 to 60), the response of each noise filtering approach has a linear and a saturation region.
- Considering all types of noise, it is seen from that BCT outperforms HT, DRT and DCT in the saturation region.
- The denoising is very significant for Salt and Pepper noise because it can be observed from Figure 6.15 that DRT, DCT and BCT surpasses HT by a large margin.
- Though BCT dominates the saturation region for Gaussian noise as shown in Figure 6.16, it competes with HT, DRT and DCT.

Table 6.2 PSNR obtained from the curvelet transform (based on HT, DRT, DCT, BCT) denoised mammograms for Salt and Pepper, Gaussian and Speckle noises. Here, the PSNRs are averaged over ten mammograms.

Types of Noise	Curvelet denoising based on conventional thresholding	Curvelet denoising based on block thresholding technique		
	HT (PSNR in db)	DRT (PSNR in db)	DCT (PSNR in db)	BCT (PSNR in db)
Salt and Pepper	19.37	23.20	21.13	20.48
Gaussian	29.84	30.08	29.67	29.83
Speckle	33.55	32.24	29.92	29.50

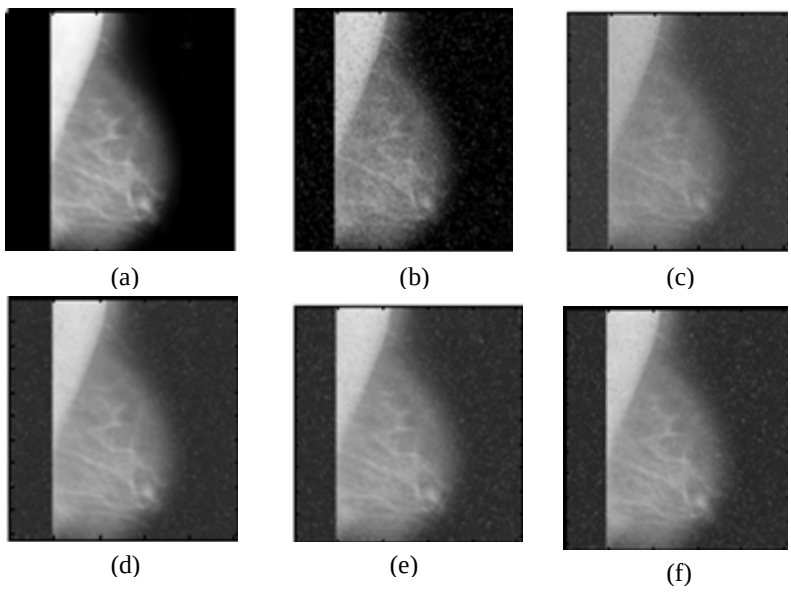

Figure 6.12 (a) Original mammogram; (b) Noisy mammogram (Salt and Pepper noise); Denoised by (c) HT; (d) DRT; (e)DCT ; (f) BCT.

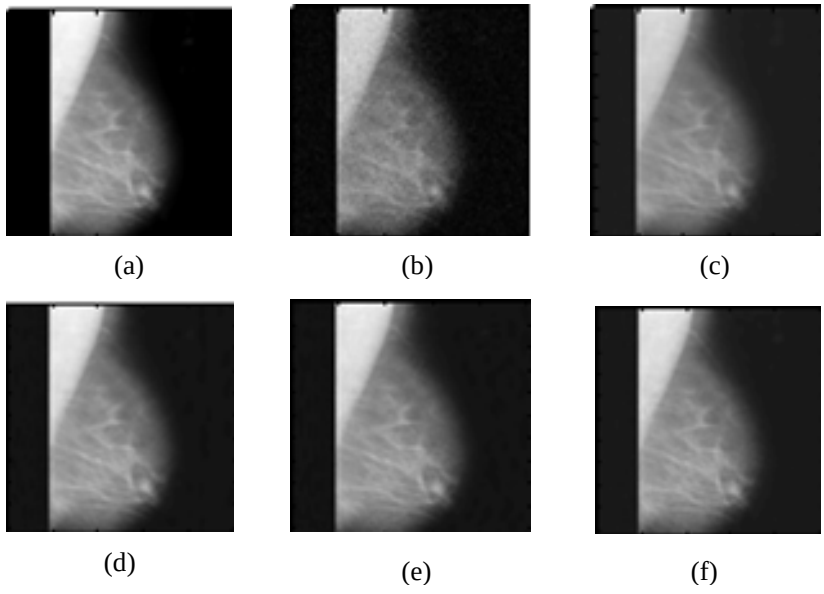

Figure 6.13 (a) Original mammogram; (b) Noisy mammogram (Gaussian); Denoised by (c) HT; (d) DRT; (e)DCT ; (f) BCT.

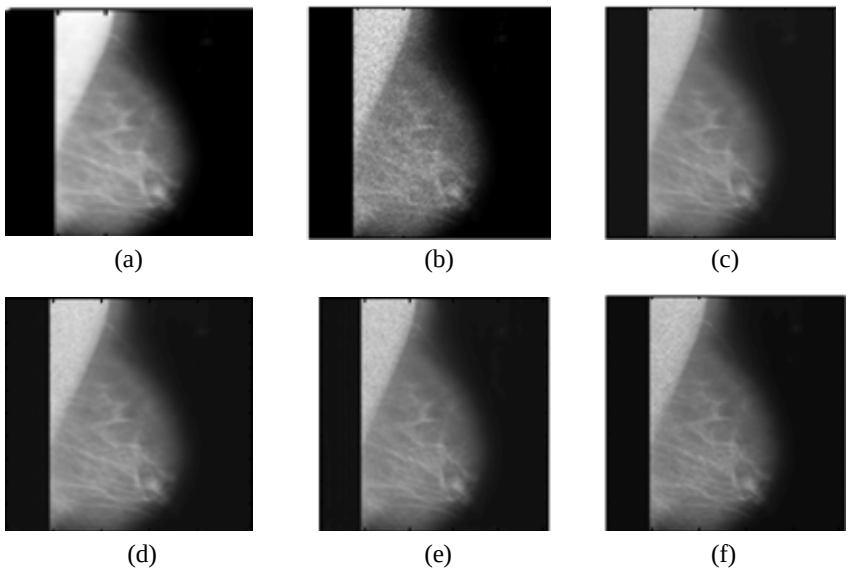

Figure 6.14 (a) Original mammogram; (b) Noisy mammogram (Speckle); Denoised by (c) HT; (d) DRT; (e) DCT ; (f) BCT.

Table 6.3. PSNR obtained from the curvelet transform (based on HT, DRT, DCT, BCT techniques) denoised mammograms caused due to the variation of noise standard deviation of Salt and Pepper noise.

Standard Deviation (σ)	HT (PSNR in db)	DRT (PSNR in db)	DCT (PSNR in db)	BCT (PSNR in db)
10	17.77	18.31	17.57	17.11
20	19.49	23.49	21.49	20.7
30	20.62	29.03	26.95	27.6
40	21.24	31.65	30.98	31.68
50	22.22	31.95	32.04	32.3
60	29.66	31.64	31.96	32.18

Table 6.4 PSNR obtained from the curvelet transform (based on HT, DRT, DCT, BCT techniques) denoised mammograms caused due to the variation of noise standard deviation of Gaussian noise.

Standard Deviation (σ)	HT (PSNR in db)	DRT (PSNR in db)	DCT (PSNR in db)	BCT (PSNR in db)
10	25.03	25.38	24.03	23.22
20	29.89	30.04	29.59	29.74
30	30.18	30.23	30.42	30.4
40	30.09	29.99	30.21	30.29
50	29.95	29.86	30.02	30.11
60	29.81	29.67	29.86	29.95

Table 6.5 PSNR obtained from the curvelet transform (based on HT, DRT, DCT, BCT techniques) denoised mammograms caused due to the variation of noise standard deviation of Speckle noise.

Standard Deviation (σ)	HT (PSNR in db)	DRT (PSNR in db)	DCT (PSNR in db)	BCT (PSNR in db)
10	26.45	26.23	25.06	24.32
20	34.59	33.14	30.9	30.54
30	37.24	37.33	36.69	37.27
40	37.01	36.84	37.67	38.15
50	36.48	36.16	36.91	37.31
60	35.96	35.51	36.26	36.61

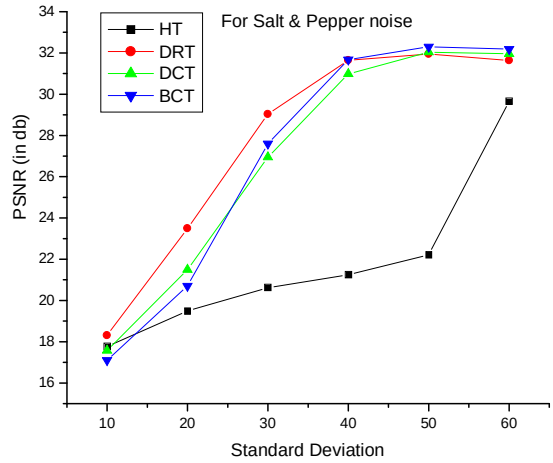

Figure 6.15 PSNR versus standard deviation of noise for different thresholding techniques based curvelet denoising of mammogram subjected to Salt and Pepper noise where HT: Hard thresholding, DRT: Diagonal real thresholding, DCT: Diagonal complex thresholding, BCT: Block complex thresholding.

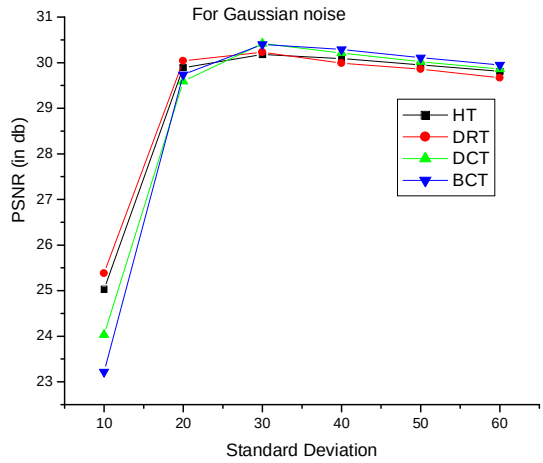

Figure 6.16 PSNR versus standard deviation of noise for different thresholding techniques based curvelet denoising of mammogram subjected to Gaussian noise where HT: Hard thresholding, DRT: Diagonal real thresholding, DCT: Diagonal complex thresholding, BCT: Block complex thresholding.

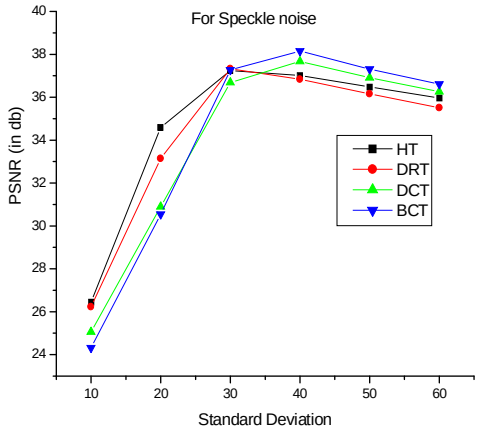

Figure 6.17 PSNR versus standard deviation of noise for different thresholding techniques based curvelet denoising of mammogram subjected to Speckle noise where HT: Hard thresholding, DRT: Diagonal real thresholding, DCT: Diagonal complex thresholding, BCT: Block complex thresholding.

6.5 Mammogram Denoising III: Poisson Noise Removal using Poisson Unbiased Risk Estimation Technique

In this section we discuss the PURE-LET approach of noise removal from low intensity images followed by the discussion on experimental results.

6.5.1 PURE-LET Approach of Poisson Noise Removal

The PURE-LET approach is a statistical estimate of the mean square error (MSE), or "risk", which is present between the unknown noise free mammogram and the processed noisy mammogram [91][100]. Due to the Poisson noise hypothesis, we denote this "risk" as Poisson unbiased risk estimate (PURE). PURE is equivalent of Stein's Unbiased Risk Estimate (SURE) which is applicable for Gaussian statistics [9] [101]. The "risk" or MSE estimate is minimized "over a collection of "acceptable" denoising processes to find the best one, in the sense of the signal-to-noise ratio (SNR), which is a widespread measure of restoration quality [2]" [91].

The PURE-LET approach is efficient because it is defined in the domain of unnormalized discrete Haar wavelet transform and is based on the theory of linear expansion of thresholds (LET). The well known block diagram representation of the unnormalized discrete Haar wavelet transform is shown in Figure 6.18; The acceptable denoising processes mentioned above "are expressed as a linear combination of elementary denoising processes, from which only the weights are unknown" [91].

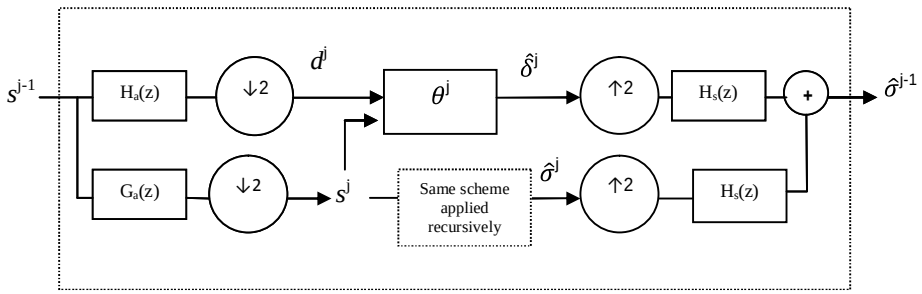

Figure 6.18 Filterbank implementation of the unnormalized discrete Haar wavelet transform. The superscript $j = 1.....J$ means the decomposition level; **s** is the vector of noisy scaling coefficients (s^0 is thus the noisy input); **d** is the vector of noisy wavelet coefficients; $\boldsymbol{\theta}$ is the subband-dependent thresholding function; $\widehat{\boldsymbol{\delta}}$ (resp. $\widehat{\boldsymbol{\sigma}}$) is the vector of the estimated noise-free wavelet (resp. scaling) coefficients [91].

It is these weights which are calculated by minimizing the PURE, through the solution of a simple linear system of equations. The PURE-LET approach of noise removal from mammogram is a popular, low memory requirement and computationally efficient denoising algorithm specially suited for low intensity imaging [92].

6.5.2 Experimental Results and Discussion

Here ten mammograms are added with Poisson noise for experimentation. All the mammograms are denoised by the wavelet, curvelet and contourlet transforms to match the order of PSNR given by Equation 6.2. It is found that the order $PSNR_{wavelet}>PSNR_{contourlet}>PSNR_{curvelet}$ of all the mammograms match truly to the order represented by Equation 6.2. Therefore, in order to reduce the Poisson noise further from the mammograms, the mammograms are denoised by PURE-LET. The denoising performance obtained by the various transforms is summarized in Figure 6.19. It is found that PURE-LET denoising outperforms all other transforms. That PURE-LET gives the best denoising result can also be visualized from a sample mammogram shown in Figure 6.20.

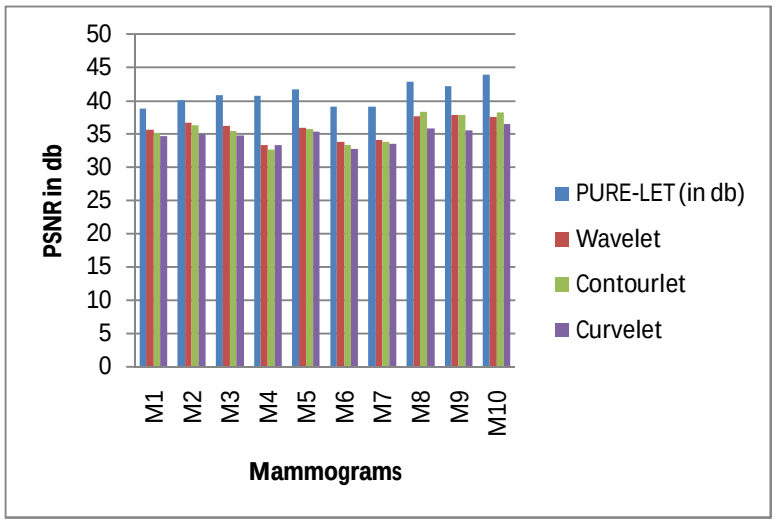

Figure 6.19 Comparison of mammogram denoising by PURE-LET, wavelet, contourlet and curvelet implemented on ten mammograms represented by M1 to M10 in terms of PSNR expressed in db [112].

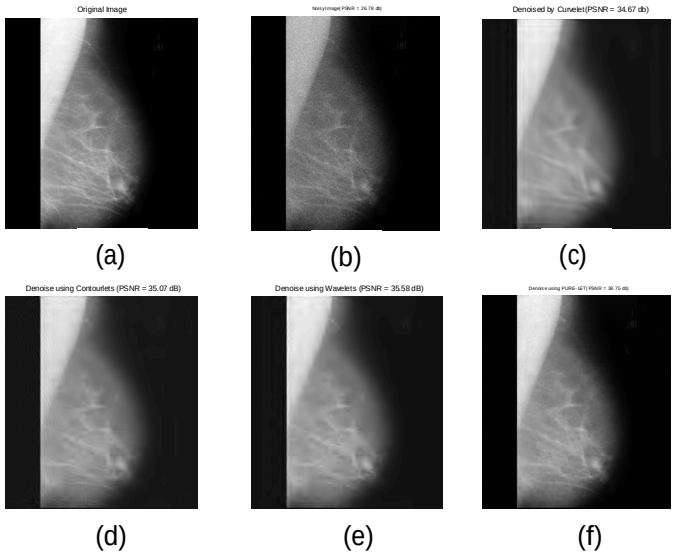

Figure 6.20 (a) Original Mammogram, (b) Noisy Mammogram (PSNR=26.78db), (c) Denoised by Curvelet (PSNR=34.67db), (d) Denoised by Contourlet (PSNR=35.07db), (e) Denoised by Wavelet (PSNR=35.58db), (f) Denoised by PURE-LET (PSNR=38.75db) [112].

The localization of the curvelet transform in the spatial, frequency and orientation domains helps the curvelet to represent the singularities which are supported on C^2 (twice continuously differentiable) curves in two dimension very sparsely and optimally [144]. That is, curvelet are suitable for representing and denoising images with curve like edges. Similarly the contourlet transform attain the optimal estimation of the 2-D functions which are smooth and have C^2 contours. In simple words the contourlet is highly efficient for the processing of images having smooth contours [22]. But here, the mammograms lack line or curve or contour singularities. The mammogram with Poisson noise may be considered as point singularities. Therefore, wavelets which can represent point singularities very well denoises the mammograms better than both the contourlet and the curvelet transform. Lastly, the PURE-LET provides the maximum denoising effect on account of two factors. First of all it is designed by unnormalized discrete Haar Wavelet transform and secondly it incorporates the concept of linear expansion of thresholds (LET) which means the overall denoising process is expressed as linear combination of elementary denoising processes [91]. As the Haar wavelet transform is an orthonormal transform, therefore the minimization of the MSE is attained separately

for each Haar wavelet decomposed sub-band of the mammogram resulting in the global minimization of MSE of the mammogram. This results in higher PSNR of the denoised mammogram as compared to wavelet, contourlet and curvelet.

6.6 Comparison of Our Work with Others

Malar *et al.* [96] denoised the mammograms with different noises using wavelet, curvelet and contourlet transforms. But all the transforms were based on only conventional hard thresholding. Whereas in the first phase of our experimentation (Mammogram Denoising I), we remove noise from mammogram using wavelet and curvelet transforms but based on three thresholding techniques- soft, hard and block thresholding. We find that our mammogram denoising method based on wavelet transform using hard thresholding is better than [96] as shown in Figure 6.21. However, mammogram denoising by curvelet transform using hard thresholding of our method, Mammogram Denoising I (Table 6.1) excels [96] in Poisson noise only. In addition, when we denoise mammograms with Poisson noise by wavelet, contourlet and curvelet in the last part of our experimentation (Mammogram Denoising III), we observe that our method using the above mentioned transforms gives better denoising result than [96] as shown in Figure 6.22. Unlike [96], we implement PURE-LET transform to result better noise removal.

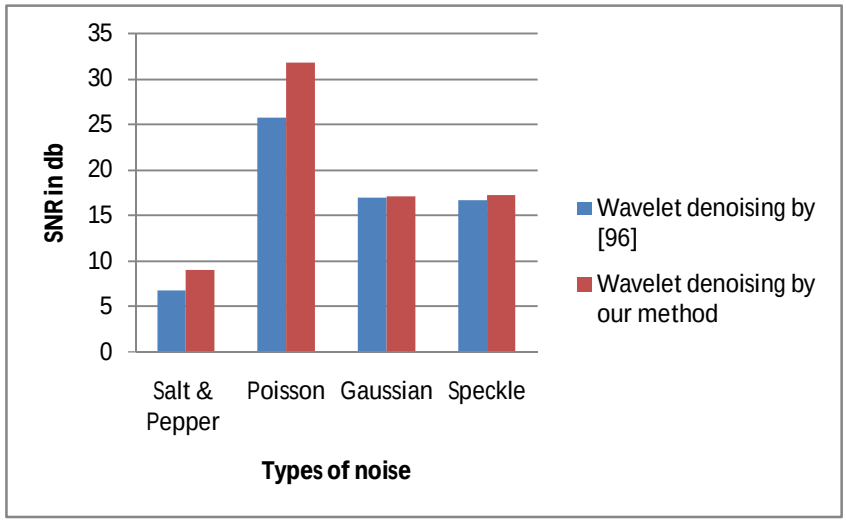

Figure 6.21 Comparison of mammogram denoising by wavelet transform based on hard thresholding [96] with our method (Mammogram Denoising I).

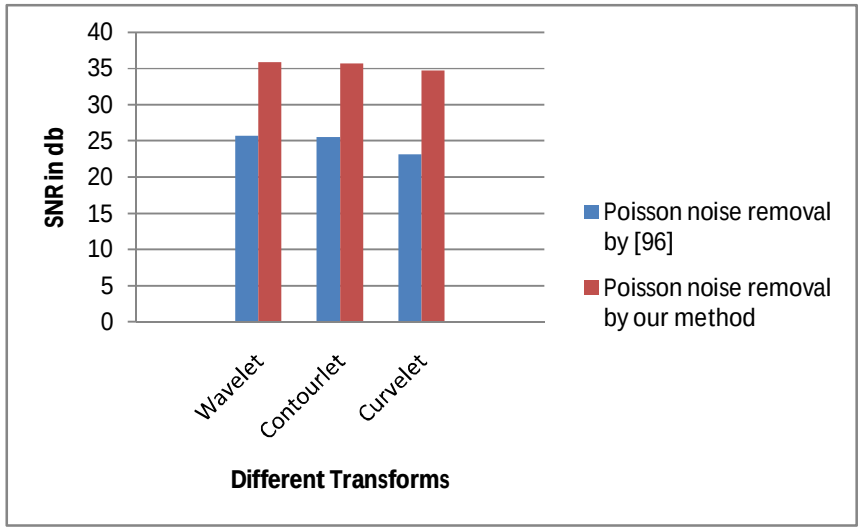

Figure 6.22 Comparison of Poisson noise removal from mammogram by curvelet transform based on hard thresholding [96] with our method (Mammogram Denoising III).

6.7 Conclusion

In this chapter we investigate the mammogram denoising comprehensively by wavelet, curvelet, contourlet and PURE-LET transforms. The four noises selected for study occur in practical cases. So this study would help the scientific community to filter noise from mammogram before reading or extracting data.

A comparative study on the role of the thresholding algorithms on mammogram denoising using the wavelet and curvelet transforms is presented. When comparison is done amongst the three thresholding techniques with the wavelet and curvelet transform separately, block thresholding provides promising SNR for all types of noise with Poisson noise being the exception. Therefore the applicability of the thresholding algorithms along with the associated transform is well established. When thresholding technique wise comparison is drawn in between wavelet and curvelet transforms, the later provides better mammogram noise removal.

Finding block thresholding and curvelet as the superior thresholding technique and transform from the first part of the experimentation, mammogram is denoised by curvelet transform in conventional (HT) and non-conventional (block thresholding)

ways. It is found that block based curvelet thresholding (DRT, DCT, BCT) should be preferred for denoising mammogram with Salt and Pepper, Gaussian and Speckle noises.

Lastly the exceptional trend of Poisson noise removal from mammogram is first studied and compared with other works. Then PURE-LET is applied to give better noise filtration. Thus the foothold of Poisson noise suppression technique called PURE-LET is exploited for Poisson noise removal of mammogram.

Chapter 7

Conclusion

7.1 Overview of the Thesis

Reviewing fifteen advanced wavelets (X-lets) for optimal sparse image representation, the wavelet and curvelet are found to be successfully applied in image processing. This thesis exploits their potentiality in medical imaging. Medical imaging is indeed a vast field. A few areas of medical imaging like i) human skin ringworm disease, ii) Darier disease (genetic disorder), iii) diabetic retinopathy, iv) mammogram denoising are selected for investigation by the wavelet, curvelet and other related transforms. The first three areas of investigation deal with detection of the disease; whereas the fourth investigation focuses on the role of different transforms and techniques to remove noise from mammogram.

7.2 Major Contributions of the Thesis

The major contributions of the thesis are briefly described below.

The primary goal of understanding the significance and classification of X-let has been presented in Chapter 1. The different areas of multiresolution image representation starting from ridgelet to other X-lets like curvelet, contourlet, wedgelet, bandlet, grouplet, surfacelet, shearlet, Gabor wavelet, brushlet, platelet, steerable pyramid, ranklet, spline wavelet, cortex transform have been reviewed from almost 150 research papers and briefly presented. The shortcomings of an X-let and gradual

development of another X-let from it is presented in Chapter 1. For example, it can be said that the failure of wavelet to capture the geometrical regularity along edges of an image is partially solved by the curvelet and almost completely solved by wedgelet. It is observed that the X-lets are structurally or functionally similar. For instance, the contourlet and the surfacelet share a common structure where Laplacian Pyramid (LP) is combined with two dimensional DFB for contourlet and with three dimensional DFB for surfacelet. Similarly, sharing of a common functionality is also observed amongst wedgelet, bandlet and grouplet that are well suited for analyzing the geometry of complex edge structure. The important observation is that despite sharing a common structure or a similar function they are very much application specific.

The literature on wavelet transform is already available in several standard books. So it is not discussed separately. However, a separate chapter is dedicated to curvelet transform. The curvelet transform is comparatively a new mathematical transform. Different research papers are available on this transform. But there is hardly any book on it. This thesis attempts to develop an almost total concept on curvelet transform in Chapter 2. The definition, properties and types of curvelet transform are systematically presented. The concept of discrete coronization which is essential to understand fast discrete curvelet transform (FDCT) but partially discussed in several papers is comprehensively addressed here. The mathematical treatment of different types of FDCT is followed by their respective algorithms. Moreover, the concept of transition of polar tiling of frequency plane to pseudopolar tiling of the same plane is demonstrated with suitable illustrations.

The human skin disease called ringworm is detected in the light of computer vision in Chapter 3. The disease is commonly found in people of all age groups. But its detection is hardly addressed in the medical imaging literature. Two independent mathematical transform based methodologies are proposed for its detection. The first methodology implements three level wavelet decomposition of the skin images by different wavelets and subsequent evaluation of the approximation and detail subband energies. The second methodology implements the curvelet to segment the circular protrusion of the skin images especially associated with ringworm images followed by statistical texture investigation by gray level co-occurrence matrix (GLCM). After feature extraction by both the methodologies, support vector machine (SVM)

recognizes the images as ringworm with detection accuracy of around 87% and 80% for first and second methodologies respectively. Both the methodologies are expansively addressed and compared with each other to select the better one. The superior method is then compared with the contemporary methodologies.

In Chapter 4, Darier disease is detected. It is a genetic disorder. But it gets expressed as changes on the skin surface. So by detecting such changes on the skin surface by proposed algorithms, we basically identify a Darier disease positive patient. The detection of this disease is rarely found in the medical imaging literature. The proposed scheme incorporates three parallel modules based on 1) GLCM, 2) local binary pattern (LBP) and 3) wavelet based energy feature for skin texture feature extraction. The feedforward neural network (FNN) receives one input database and one target database from each of the three parallel modules for Darier disease detection. All the approaches are compared to find the most suitable one as skin texture screening tool. The GLCM, LBP and wavelet based schemes attain Darier disease detection accuracy of about 82%, 82% and 89% respectively. The other important aspect of this work is that GLCM based module addresses the presence and location of several typical skin texture abnormalities by the statistical plots.

The early detection of diabetic retinopathy (DR) and its subsequent medication is of prime importance to the medical practitioners. Chapter 5 deals with the implementation of the curvelet transform to segment the non-linear and twisted retinal blood vessels from the fundus image. As the curvelet is specially formulated to provide the sparse representation of the objects having curve singularities, it is thoughtfully deployed in this investigation to extract the blood vessels from the retina image. The essence of this scheme is that the curvelet extracted retinal blood vessels are examined by the Automated Retinal Image Analyzer (ARIA) [7] to compute the retinal blood vessel features (RBVF). It is medically approved that with the severity of DR there are significant changes in RBVF. Therefore, RBVF of both DR and non-diabetic retinopathy (NDR) images are computed to tabulate input and target databases which are provided to the FNN for DR detection.

Mammogram is an easy and affordable means of diagnosis of breast cancer. Like other medical data, it is also affected by noise during acquisition. Most of the works on mammogram denoising deal with the performance of different transforms. The investigation performed in Chapter 6 aims at denoising the mammogram by the

wavelet and the curvelet transform with a motive to examine the role of the "embedded" thresholding algorithm. As the thresholding technique is a key factor for the noise reduction, a comprehensive study on the employment of soft, hard and block thresholding techniques with the transforms have been presented methodically. Mammogram is supplemented with different types of noise and then denoised by the wavelet and the curvelet transforms using the above mentioned thresholding techniques to compare the denoising performance of the thresholding algorithms along with the transforms.

Malar *et al.* [96] denoised mammogram with Salt and Pepper, Poisson, Gaussian and Speckle noises by wavelet, contourlet and curvelet transforms. It is found from comparative study [96] that the curvelet transform based on conventional hard thresholding (HT) is better than other transforms for noise removal of mammograms. So this investigation is carried forward with an intent to improve denoising performance of curvelet transform by incorporating non-conventional thresholding. Here, block thresholding is considered as the non-conventional thresholding. The block thresholding technique is of three types- diagonal real thresholding (DRT), diagonal complex thresholding (DCT) and block complex thresholding (BCT). The mammogram noise removal by curvelet transform based on (HT) is then compared with that of DRT, DCT and BCT algorithms. It is found that the block thresholding techniques outperform HT technique in removing mammogram noise.

Investigating Table 1[96], it is found that the wavelet transform removes Poisson noise from mammogram better than the contourlet and curvelet transforms. This is exceptional because for Salt and Pepper, Gaussian and Speckle noises wavelet transform shows poor performance. So the unusual trend of Poisson noise removal from mammogram by the above transforms is verified. Secondly, a recently developed denoising strategy called Poisson Unbiased Risk Estimation–Linear Expansion of Thresholds (PURE-LET) is applied to the mammograms. It is based on unnormalized discrete Haar wavelet and is applied to mammogram to remove Poisson noise better than wavelet, contourlet and curvelet transforms. Mäkitalo *et al.* in 2013 applied PURE-LET to Fluorescent Microscopy [101]. This time, PURE-LET is implemented to an unexplored area of mammogram noise filtration.

7.3 Scope of Future Work

In Chapter 1, fifteen different types of X-lets are discussed. In future researchers may come up with a new X-let called Masterlet. The proposed block diagram of Masterlet is given in Figure 7.1. The Masterlet is divided into N number of Sub-grouplets and each Sub-grouplet is further classified into a fixed number of X-lets. At first, the input image should be tested with certain algorithm to match with a particular Sub-grouplet. And once it is done, the algorithm should further decide which X-let would be the most appropriate one for its representation with given limitations. Thus all the X-lets could be replaced by a smart Masterlet which would take care of all the geometrical complexities, conditions and constraints of an image and accordingly select the most suitable inbuilt X-let needed for its optimum representation.

We have performed some specific studies on the applicability of curvelet and wavelet transform in medical image processing. The medical images are taken from standard image database. In future, we plan to create our own databases with large number of images. This would simplify the preprocessing steps. It would also help other researchers to carry their scientific work.

The work on ringworm detection can be extended by introducing colour as an important feature in image database. This would improve ringworm detection accuracy.

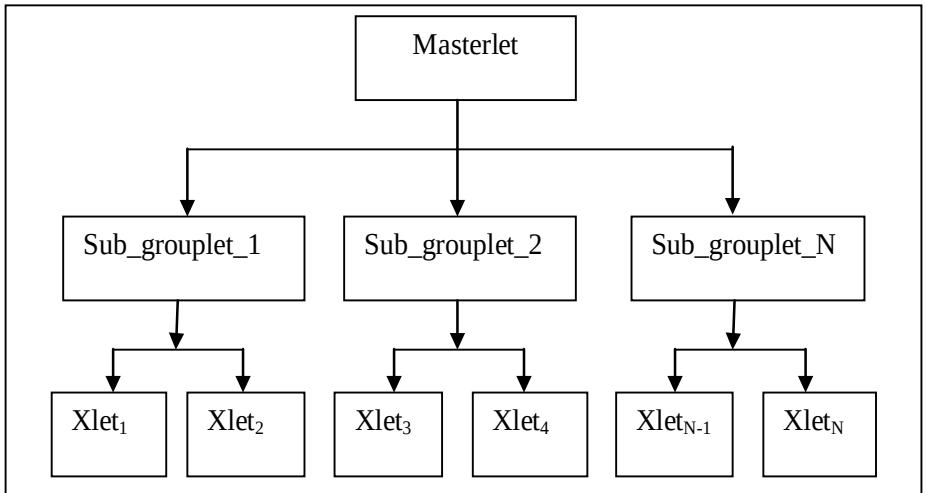

Figure 7.1 Block diagram of Masterlet.

Our present work, Chapter 5 detects DR image from DR and NDR images. This work can be completed by detecting the exact stage of DR, that is, mild non-proliferative retinopathy, moderate non-proliferative retinopathy, severe non-proliferative retinopathy or proliferative retinopathy. Then a medical person can detect if a patient is DR positive. If so, he can also know the exact stage of it and initiate immediate medication.

In Mammogram Denoising I, Chapter 6 we have denoised mammogram by soft, hard and block thresholding techniques based on wavelet and curvelet transforms. In future, the same work can be extended with the contourlet transform. And then a comparison can be made amongst the thresholding techniques based on wavelet, curvelet and contourlet transforms.

All the referred papers of the work stressed on the detection accuracy of the disease only because the computational time is very small. In future, work may be done to study and compare the computational complexities of the proposed methods.

The proposals suggested and executed in this thesis would help to improve the computer supported diagnostic system of diseases. The medical personnel can take quick and accurate decisions for diagnosing diseases. The thesis would also enlighten the scientific community to extend the research proposals.

Bibliography

[1] V. Alarcon-Aquino, O. Starostenko, J. M. Ramirez-Cortes, R. Rosas-Romero, J. Rodriguez-Asomoza, O. J. Paz-Luna, K. Vazquez-Munoz, Detection of microcalcifications in digital mammograms using the dual-tree complex wavelet transform, Engineering Intelligent Systems, Vol. 17, No. 1, pp.49-63, 2009.

[2] B. Al-Diri, A. Hunter, D. Steel, M. Habib, T. Hudaib, S. Berry, Review – reference data set for retinal vessel profiles, In Proceedings of the 30th Annual Conference of the IEEE Engineering in Medicine and Biology Society, Vancouver, British Columbia, Canada, 20-24th August 2008

[3] S. H. M. Alipour, H. Rabbani, M. R. Akhlaghi, Diabetic retinopathy grading by digital curvelet transform, Computational and Mathematical Methods in Medicine,Vol. 2012, No. 761901, 11 pages, doi: 10.1155/2012/761901

[4] E. Angelini, R. Campanini, E. Iampieri, N. Lanconelli, M. Masotti, T. Petkov and M. Roffili, A ranklet- based CAD for digital mammography, in Proceedings of 8th International Workshop on Digital Mammography, pp. 349-346, Manchester, UK, 2006

[5] S. Arivazhagan, L. Ganesan, Texture classification using wavelet transform, Pattern Recognition Letters, Vol. 24, No. 10, pp. 1513-1521, June 2003

[6] R. H. Bamberger, M. J. T. Smith, A filter bank for the directional decomposition of images: theory and design, IEEE Transactions on Signal Processing, Vol. 40, No. 4, pp. 882-893, April 1992

[7] P. Bankhead, C. N. Scholfield, J. G. McGeown, T. M. Curtis, “Fast retinal vessel detection and measurement using wavelets and edge location refinement, PloS ONE, Vol. 7, No.3, e32435, March 2012, doi: 10.1371/journal.pone.0032435

[8] K. Bashar, N. Ohnishi, Fusing cortex transform and intensity based features for image texture classification, in Proceedings of 5th International Conference on Information Fusion, Vol. 2, pp. 1463-1469, Annapolis, MD, USA, 8-11July 2002

[9] T. Blu, F. Luisier, The SURE-LET approach to image denoising, IEEE Transactions on Image Processing, Vol. 16, No. 11, pp. 2778-2786, 2007

[10] T. Cai, "On block thresholding in wavelet regression: adaptivity, block size, and threshold level, Statistica Sinica, Vol. 12, pp. 1241-1273, 2002.

[11] E. J. Candès, Ridgelets : theory and applications, Ph.D dissertation, Department of Statistics, Standford University, Standford, California, September 1998

[12] E. J. Candès and D. L. Donoho, Ridgelets: A key to higher-dimensional Intermittency?, Phil. Trans. A, Royal Society of London, Vol. 357, No. 1760, pp. 2495-2509, 1999

[13] E. J. Candès and D. L. Donoho, Curvelets - A surprisingly effective nonadaptive representation for objects with edges, in Curve and Surface Fitting, A. Cohen, C. Rabut and L. L. Schumaker, Eds. Nashville, TN: Vanderbilt University Press, 1999

[14] E. J. Candès and D. L. Donoho, New tight frames of curvelets and optimal representation of objects with piecewise C^2 singularities, Commun. Pure Appl. Math, pp.219-266, February 2004

[15] E. Candes and D. Donoho, Continuous curvelet transform. I. Resolution of the wavefront set, Applied Computation Harmonic Analysis, Vol. 19, No.2, pp.162-197, 2005

[16] E. Candès, L. Demanet, D. Donoho, and L. Ying, Fast discrete curvelet transforms, SIAM Multiscale Modeling and Simulation, Vol. 5, No. 3, pp.861-899, 2006, Also available at: http://math.mit.edu/icg/papers/FDCT.pdf

[17] S. Chaudhuri, S. Chatterjee, N. Katz, M. Nelson, M. Goldbaum, Detection of blood vessels in retina images using two- dimensional matched filters, IEEE Transactions on Medical Imaging, Vol. 8, No. 3, pp. 263-269, September 1989

[18] R. Cohen, Signal denoising using wavelets, Project Report, Department of Electrical Engineering, Technion, Israel Institute of Technology, Also available at:http://www.tx.technion.ac.il/~rc/SignalDenoisingUsing Wavelets_RamiCohen.pdf

[19] M. J. Cree, J. J. G. Leandro, J.V. B. Soares, R. M. J. Cesar Jr., H. F. Jelinek, D. Cornforth, Comparison of various methods to delineate blood vessels in retinal images, In Proceedings of the 16th Australian Institute of Physics Congress, Canberra, 30th January-4 February 2005.

[20] N. Das, A. Pal, S. Mazumder, S. Sarkar, D. Gangopadhyay, M. Nasipuri, An SVM based skin disease identification using local binary patterns, in Proceedings of Third International Conference on Advances in Computing and Communications (ICACC), pp.208-211, Cochin, India, 29-31 August 2013.

[21] J. G. Daugman, Complete discrete 2D gabor transforms by neural networks for image analysis and compression, IEEE Transactions on Acoustic, Speech and Signal Processing, Vol. 36, pp. 1169-1179, 1988

[22] M. N. Do, M. Vetterli, The contourlet transform: an efficient directional multiresolution image representation, IEEE Transactions on Image Processing, Vol. 14, No.12, pp. 2091-2106, December 2005

[23] M. N. Do, Directional multiresolution image representations, Ph.D. Dissertation, Department of Communication Systems, Swiss Federal Institute of Technology, Lausanne, Switzerland, November 2001. Also available at : http://www.ifp.illinois.edu/~minhdo/publications/thesis.pdf

[24] D. L. Donoho and M. R. Duncan, Digital curvelet transform: strategy, implementation and experiments, In Proceedings of Aerosense 2000, Wavelets Applications VII, vol. 4056, pp.12-29. SPIE, 2000 Also available at: http://www.curvelet.org/papers/DCvT99.pdf

[25] D. L. Donoho, Wedgelets: nearly minimax estimation of edges, Annals of Statistics, Vol. 27, No. 3, pp. 859-897, 1997

[26] S. Dua, U. R. Acharya, P. Chowriappa, S. V. Sree, Wavelet- based energy features for glaucomatous image classification, IEEE Transactions on Information Technology in Biomedicine, Vol. 16, No.1, November 2011

[27] R. O. Duda, P. E Hart and H.G. Stork, Pattern Classification, 2nd ed. New York: Wiley Interscience, 2001

[28] W. D. Ellis (ed), A Source book of Gestalt Psycology. The Gestalt Journal Press Inc. 2007, U.S

[29] I. El-Naqa, Y. Yang, M. N. Wernick, N. P. Galatsanos, R. M. Nishikawa, A support vector machine approach for detection of microcalcification, IEEE Transactions on Medical Imaging, Vol. 21, No. 12, pp. 1552-1563, 2002

[30] M. M. Eltoukhy, I. Faye, B. B. Samir, A comparison of wavelet and curvelet for breast cancer diagnosis in digital mammogram, Computers in Biology and Medicine, Vol. 40, No. 4, pp. 384-391, 2010.

[31] M. Esmaeili, H. Rabbani, A. Mehri, A. Dehghani, Extraction of retinal blood vessels by curvelet transform, in Proceedings of IEEE International Conference on Image Processing 2009, (ICIP'09), pp. 3353-3356, Cairo, 7-10 November 2009, doi://10.1109/ICIP.2009.5413909

[32] M. Esmaeili, H. Rabbani, A. M. Dehnavi, and A. Dehghani, Automatic optic disk detection by the use of curvelet transform, in Proceedings of 9th International Conference on Information Technology and Applications in Biomedicine 2009, (ITAB 2009), pp. 1–4, Larnaca, 4-7 November 2009, doi://10.1109/ITAB.2009.5394299

[33] B. Fang, W. Hsu, and M. Lee, Reconstruction of vasculature structures in retinal images, In proceedings of 2003 International Conference on Image Processing, (ICIP'03), Vol. 3, pp. II: 157-160, Barcelona, Catalonia, Spain, 14-17 September 2003, doi: 10.1109/ICIP.2003.1246640

[34] W. T. Freeman and E. H. Adelson, The design and use of steerable filters, IEEE Transactions on Pattern Analysis and Machine Intelligence, Vol.13, No. 9, pp.891-906, September 1991

[35] R. Garnavi, M. Aldeen, J. Bailey, Computer-aided diagnosis of melanoma using border and wavelet based texture analysis, IEEE Transactions on Information Technology in Biomedicine, Vol. 16, No. 6, November 2012

[36] R. C. Gonzalez, R. E. Woods, Digital Image Processing, Pearson Education India, Second Edition 2002

[37] C. Goresnsic, S. R. Rotman, Texture classification using the cortex transform, CVGIP: Graphical Models and Image Processing, Vol. 54, No. 4, pp. 329-339, July 1992

[38] P. Görgel, A. Sertbas, O. N. Ucan, Mammographical mass detection andclassification using local seed region growing- spherical wavelet transform(LSRG-SWT) hybrid scheme, Computers in Biology and Medicine, Vol. 43, No. 6, pp. 765-774, 2013

[39] P. Hall, G. Kerkyacharian, D. Picard, Block threshold rules for curve estimation using kernel and wavelet methods, The Annals of Statistics, Vol. 26, No. 3, pp.922-942, 1998

[40] P. Hall, G. Kerkyacharian, D. Picard, On the minimax optimality of block thresholded wavelet estimators, Statistica Sinica, Vol. 9, pp. 33-49, 1999

[41] B. Han, G. Kutyniok, Z. Shen, Adaptive multiresolution analysis structures and shearlet systems, SIAM Journal on Numeric Analysis, Vol. 49, pp. 1921-1946, 2011

[42] S. Haykin, Neural networks: a comprehensive foundation, 2nd Edition. Delhi, Pearson Education 2004

[43] A. Hoover, V. Kouznetsova, M. Goldbaum, Locating blood vessels in retina images by piece-wise threshold probing of a matched filter response, IEEE Transactions on Medical Imaging, Vol. 19, No. 3, pp. 203-210, March 2000

[44] A. Hoover and M. Goldbaum, Locating the optic nerve in a retinal image using the fuzzy convergence of the blood vessels, IEEE Transactions on Medical Imaging, Vol. 22, No. 8, pp. 951-958, August 2003

[45] Li Hua, S Wang, C. Deng, New image denoising method based wavelet and curvelet transform, In Proceedings of International Conference on Information Engineering, ICIE'09, Vol 1, pp. 136-139, Taiyuan, Shanxi, 10-11July 2009

[46] K. Huang, S. Aviyente, Wavelet feature selection for image classification, IEEE Transactions on Image Processing, Vol. 17, No. 9, pp. 1709-1720, 4th August 2008

[47] http://en.wikipedia.org/wiki/Cross-validation%28statistics%29

[48] http://en.wikipedia.org/wiki/Sensitivity%20and%20specificity?oldid=63623696

[49] http://fpcsonora.com/?page id=132

[50] http://ideas.health.vic.gov.au/bluebook/ringworm-info.asp

[51] http://in.mathworks.com/help/images/gray-level-co-occurrence-matrix-glcm.htm

[52] http://in.mathworks.com/help/nnet/ref/plotperform.html

[53] http://media.johnwiley.com.au/product_data/excerpt/19/04713491/0471349119.pdf

[54] https://nei.nih.gov/health/diabetic/retinopathy

[55] http://www.britishskinfoundation.org.uk/SkinInformation/AtoZofSkindisease/DariersDisease.aspx

[56] http://www.ces.clemson.edu/~ahoover/stare/

[57] http://www.cfsph.iastate.edu/FastFacts/pdfs/dermatophytosis_F.pdf

[58] http://www.curvelet.org./software.html

[59] http://www.dermis.net/dermisroot/en/41367/diagnose.htm

[60] http.//www.dermnet.com

[61] http.//www.dermnetnz.org

[62] http:// www.dermnetnz.org/scaly/darier.html

[63] http://www.en.wikipedia.org/wiki/Feedforward_neural_network

[64] http://www.healthcare.siemens.com/computed-tomographycase-studies/using-iris-and-x- care.html

[65] http://www. healthcare.siemens.com/magnetic-resonance-imaging/magnetom-

[66] http://www.icoph.org/downloads/Diabetic-Retinopathy-Scale.pdf

[67] http://www.mathworks.in/matlabcentral/fileexchange/8837-contourlet-toolbox

[68] http://www.mathworks.in/matlabcentral/fileexchange/31557-pure-let-for-poisson- image-denoising

[69] http://www.news-medical.net/health/What-is-ringworm.aspx

[70] http://www.olympusmicro.com/galleries/fluorescence/

[71] http://www.patient.co.uk/health/Ringworm

[72] http://www.qmedicine.co.in/top%20health%20topics/A/Angiography-Coronary.html

[73] http://www.webmd.boots.com/skin-problems-and-treatments/ss/slideshow-ringworm, "Copyright©2009 Boots UK Limited and WebMD UK Limited. All Rights reserved"

[74] http://www.willseye.org/health-library/diabetic-retinopathy

[75] M. Iwamuro, Y. Miyabe, H. Kai, Y. Kawai, K.Takata, T. Murakami, H. Mifune, K. Yamamoto, Regression of metastatic colon tumour from primary adenocarcinoma of the lung due to fistulisation to the bowel lumen, doi: 10.3332/ecancer.2014.412

[76] A. K. Jain and F. Farrokhnia, Unsupervised texture segmentation using gabor filters, Pattern Recognition, Vol. 24, No. 12, pp. 1167-1186, 1991

[77] S. M. H. Jamarani, G. Rezai-rad, H. Behnam, A novel method for breast cancer prognosis using wavelet packet based neural network, In Proceedings of 27th Annual Conference on IEEE Engineering in Medicine and Biology, pp. 3414-3417, Shanghai, China

[78] P. Kahai, K. R. Namuduri, H. Thompson, A decision support framework for automated screening of diabetic retinopathy, International Journal of Biomedical Imaging, Vol. 2006, No. 45806, 2006

[79] V. Kidsumran, W. Chiracharit, Contrast enhancement mammograms using denoising in wavelet coefficients, In Proceedings of 10th International Joint Conference on Computer Science and Software Engineering (JCSSE), pp. 82-86, Maha Sarakham, Thailand, 29-31 May 2013.

[80] E. Kolaczyk and R. Nowak, Multiscale likelihood analysis and complexitypenalized estimation, Annals of Statistics, Vol. 32, No. 2, pp.500-527, 2004

[81] R. Kumar, A. Indrayan, Receiver operating characteristic (ROC) curve for medical researchers, Indian Pediatrics, Vol. 48, pp. 277-287, April 2011

[82] S. Kundu, N. Das, M. Nasipuri, Automatic detection of ringworm using local binary pattern (LBP), In Proceedings of Seventh Indian Conference on Computer Vision, Graphics and Image Processing (ICVGIP-2010), Chennai, India, 9-10th December 2010.

[83] D. Labate, G. Kutyniok, W.Q. Lim, G. Weiss, Sparse multidimensional representation using shearlets. In Proceedings of SPIE, Wavelets XI, 59140U, September 17, 2005, doi:10.1117/12.613494

[84] A. Laine, J. Fan, Texture classification by wavelet packet signature, IEEE Transactions on Pattern Analysis and Machine Intelligence, Vol. 15, No. 11, pp.1186-1191, November 1993

[85] M. Larsen, J. Godt, N. Larsen, H. Lund-Andersen, A. K. Sjolie, E. Agardh, H.Kalm, M. Grunkin, D. R. Owens, Automated detection of fundus photographic red lesions in diabetic retinopathy, Investigative Opthalmology & Visual Science, Vol. 44, No.2, pp. 761-766, 2003

[86] R. V. Lichode, P.S. Kulkarni, Automatic diagnosis of diabetic retinopathy by hybrid multilayer feedforward neural network, International Journal of Science, Engineering and Technology, Vol 2, no.9, September 2013

[87] Z. Liu, K. Tsukada , K. Hanasaki, Y. K. Ho, Y. P. Dai, Image fusion by steerable pyramid, Pattern Recognition Letters, Vol. 22, No. 9, pp. 929-939, July 2001

[88] Y. Lu, M. N. Do, A new contourlet transform with sharp frequency localization, In Proceedings of IEEE International Conference on Image Processing, pp. 1629-1632, 8-11 October 2006.

[89] Y. M. Lu, M. N. Do, Multidimensional directional filter banks and surfacelets, IEEE Transactions on Image Processing, Vol. 16, pp. 918-931, April 2007

[90] Y. Lu, M. N. Do, 3-D Directional filter banks and surfacelets, In Proceedings of SPIE Conference on Wavelet Applications in Signal and Image Processing XI, San Diego, USA, July 2005

[91] F. Luisier, C. Vonesch, T. Blu, M. Unser, Fast interscale wavelet denoising ofPoisson–corrupted images, Signal processing, Vol. 90, pp.415-427, 2010

[92] F. Luiser, T. Blu, M. Unser, Image denoising in mixed Poisson–Gaussian noise, IEEE Transactions on Image Processing, Vol. 20, No. 3, pp. 696-708, 2011

[93] J. Ma, G. Plonka, The curvelet transform, IEEE Signal Processing Magazine, Vol. 27, No. 2, pp.118-133, March 2010, doi:10.1109/MSP.2009.935453

[94] J. Ma, G. Plonka, Computing with curvelets : from image processing to turbulent flows, Computing in Science and Engineering, Vol. 11, No. 2, pp.72-80, March– April 2009 doi:10.1109/MCSE.2009.26

[95] I. Maglogiannis, C. N. Doukas, Overview of advanced computer vision systems for skin lesion characterizations, IEEE Transactions on Information Technology in Biomedicine, Vol.13, No. 5, pp.721-733, 2009.

[96] E. Malar, A. Kandaswamy, S. S. Kirthana, D. Nivedhitha, A comparative study on mammographic image denoising technique using wavelet, curvelet and contourlet transforms, In Proceedings of International Conference on Machine Vision and Image Processing (MVIP), pp. 65-68, Taipei, Taiwan, 14-15 December 2012.

[97] E. Malar, A. Kandaswamy, S. S. Nivedhitha, M. Gauthaam, Curvelet image denoising of mammogram images, International Journal of Medical Engineering and Informatics, Vol. 5, No. 1, pp. 60-67, 2013

[98] S. Mallat, G. Peyre, A review of bandlet methods for geometrical image representation, Numerical Algorithm, Vol.44, No.3, pp.205-234, March 2007

[99] S. Mallat, Geometrical grouplets, Applied and Computational Harmonic Analysis, Vol. 26, No. 2, pp.161-180, 2009

[100] M. Mäkitalo, A. Foi, Optimal inversion of the Anscombe transformation in low– count poisson image denoising, IEEE Transactions on Image Processing, Vol. 20, No. 1, pp. 99-109, 2011

[101] M. Mäkitalo, A. Foi, Optimal inversion of the generalized Anscombe Transformation for Poisson-Gaussian noise, IEEE Transactions on Image Processing, Vol. 22, No.1, pp. 91-103, 2013

[102] A. M. Mendonca, A. Campilho, Segmentation of retinal blood vessels by combining the detection of centerlines and morphological reconstruction, IEEE Transactions on Medical Imaging, Vol. 25, No. 9, September 2006

[103] F. G. Meyer and R. R. Coifman, Brushlet: A tool for directional image analysis and image compression, Applied and Computational Harmonic Analysis, Vol.4, pp.147– 187, 1997

[104] A. K. Mitra, R. Parekh, Automated detection of skin diseases using texture features, International Journal of Engineering Science and Technology, Vol. 3, No.6, June 2011

[105] N. Naveed, A. Hussain, M. J. Arfan, TS Choi, Quantum and impulse noise filtering from breast mammogram images, Computer Methods and Programs in Biomedicine, Vol. 108, No.3, pp. 1062-1069, December 2012

[106] M. Niemeijer, J. J. Staal, B. V. Ginneken, M. Loog, and M. D. Abràmoff, Comparative study of retinal vessel segmentation methods on a new publicly available database, In Proceedings of SPIE 5370, Medical Imaging 2004: Image Processing, J. M. Fitzpatrick, M. Sonaka, Eds, San Diego, CA, 14 February 2004, Vol. 5370, pp. 648-656. doi: 10.1117/12.535349

[107] A. Nimunkar, A. P. Dhawan, P. A. Relue, S. V. Patwardhan, Wavelet and statistical analysis for melanoma classification, In Proceedings of SPIE 4684, Medical Imaging 2002: Image Processing, 1346, San Diego, CA, 15th May 2002, doi:10.1117/12.467098

[108] R. Parikh, A. Mathai, S. Parikh, G. C. Sekhar, R. Thomas, L.V. Prasad, Understanding and using sensitivity, specificity and predictive values, Indian Journal of Opthalmology, Vol.56, No.1, pp.45-50, January-February 2008

[109] S.V. Patwardhan, A. P. Dhawan, P. A. Relue, Classification of melanoma using tree structured wavelet transforms, Computer Methods and Programs in Biomedicine. Vol.72, pp. 223-239, 2003.

[110] E. L. Pennec and S. Mallat, Sparse geometric image representations with bandlets, IEEE Transactions on Image Processing, Vol. 14, No. 4, pp.423-438, April 2005

[111] G. Peyre, The Numerical Tours of Signal Processing-Advanced Computational Signal and Image Processing, IEEE Computing in Science and Engineering, Vol. 13, No. 4, pp. 94-97, 2011

[112] M. Saha, M. K. Naskar, B. N. Chatterji, Poisson noise removal from mammogram using Poisson Unbiased Risk Estimation Technique, In Proceedings of the Second International Conference on Information Systems Design and Intelligent Applications- 2015 (INDIA 2015), Kalyani, West Bengal, 8-9 January 2015, vol. 2, pp. 327-335, DOI 10.1007/978-81-322-2247-7_3

[113] M. Saha, M. K. Naskar, B. N. Chatterji, Mammogram denoising by curvelet transform based on the information of neighbouring coefficients, In Proceedings of the 2015 Third International Conference on Computer, Communication, Control and Information Technology (C3IT), Hoogly, West Bengal, 7-8 February 2015, pp.1-6. Also available at IEEE Xplore Digital Library, DOI 10.1109/C3IT.2015.7060180

[114] M. Saha, M. K. Naskar, B. N. Chatterji, Detection of diabetic retinopathy using the wavelet transform and feedforward neural network, In Proceedings of the 2nd International Doctoral Symposium on Applied Computation And Security Systems, Kolkata, 23-25 May 2015, DOI:10.1007/978-81-322-2650-5_7

[115] M. Saha, M. K. Naskar, B. N. Chatterji, Human Ringworm Detection using Wavelet Energy Signature, in Proceedings of the 2015 IEEE 2nd International Conference on Recent Trends in Information Systems (ReTIS-15), Jadavpur University, Kolkata, 9-11July 2015, pp. 178-182. Also available at IEEE Xplore Digital Library, DOI 10.1109/ReTIS.2015.7232874

[116] M. Saha, M. K. Naskar, B. N. Chatterji, Soft, hard and block thresholding techniques for denoising of mammogram images, IETE Journal of Research, vol.61, No.2, pp.186-191, February 2015

[117] M. Saha, M. K. Naskar, B. N. Chatterji, Darier Disease – A Genetic Disorder Detection in the Light of Computer Vision, International Journal of Enhanced Research in Science, Technology & Engineering, Vol. 5, No. 2, February 2016

[118] A. Salazar-Gonzalez, D. Kaba, Y. Li, X. Liu, Segmentation of the blood vessels and optic disc in retinal images, IEEE Journal of Biomedical and Health Informatics, Vol. 18, No.6, pp. 1874-1886, 27 January 2014

[119] C. L. Samuel, T.L. Elisa, W. Yiming, K. Ronald, M. K. Ronald, W. Ann, Computer classification of a nonproliferative diabetic retinopathy, Archives of Ophthalmology, Vol. 123, pp.759-764, 2005

[120] I. J. Schoenberg, Contribution to the problem of approximation of equidistant data by analytic functions, Part A: On the problem of smoothing or graduation, a first class of analytic approximation formulas, Quart. Appl. Math., vol.4, pp.45-99, 1946

[121] S. Sigurdsson, P. A. Philipsen, L. K. Hansen, J. Larsen, M. Gniadecka, H. C. Wulf, Detection of skin cancer by classification of Raman spectra, IEEE Transactions on Biomedical Engineering, Vol. 51, No. 10, pp.1784-93, 2004

[122] E. P. Simoncelli, W. T. Freeman, E. H. Adelson, and D. J. Heeger, Shiftable multiscale transforms, IEEE Transactions on Information Theory-Part 2, Vol. 38, No.2, pp. 587– 607, March 1992.

[123] E. P. Simoncelli and W. T. Freeman, The steerable pyramid: A flexible architecture for multi-scale derivative computation, in Proceedings of International Conference on Image Processing, Washington, DC, USA, 23-26 October 1995,vol. 3, pp.444-447

[124] C. Sinthanayothin, V. Kongbunkiat, S. Phoojaruenchanachai, A. Singalavanija, Automated screening system for diabetic retinopathy, In Proceedings of the 3rd International Symposium on Image and Signal Processing and Analysis, Vol. 44, No. 2, pp. 767-771, 2003.

[125] F. Smeraldi, Ranklets: orientation selective nonparametric features applied to face detection, in Proceedings of 16th International Conference on Pattern Recognition, vol. 3, pp. 379–382.Qubec, Qc, August 2002

[126] J. V. B. Soares, J. J. G. Leandro, R. M. Cesar Jr., H. F. Jelinek, M. J. Cree, Retinal vessel segmentation using the 2-D gabor wavelet and supervised classification, IEEE Transactions on Medical Imaging, Vol. 25, No. 9, September 2006

[127] S. Sridhar, Digital Image Processing, Oxford University Press, New Delhi, India, 2011

[128] J. J. Staal, M. D. Abràmoff, M. Niemeijer, M. A. Viergever, B. V. Ginneken, Ridge-based vessel segmentation in color images of the retina, IEEE Transactions on Medical Imaging, Vol. 23, No. 4, pp.501-509, April 2004

[129] J. L. Starck, E. J. Candes and D. L. Donoho, The curvelet transform for image denoising, IEEE Transactions on Image Processing, Vol.11, No.6, pp. 670-684, June 2002

[130] J. L. Starck, J. Fadili, F. Murtagh, The undecimated wavelet decomposition and its reconstruction, IEEE Transactions on Image processing, Vol. 16, No.2, pp. 297-309, February 2007

[131] R. Strickland, H. Hahn, Wavelet transforms for detecting microcalcifications in mammogram, IEEE Transactions on Medical Imaging, Vol. 15, No. 2, pp. 218-229, 1996

[132] J. Suckling, J. Parker, D. R. Dance, S. M. Astley, I. Hutt, C. R. M. Boggis, I. Ricketts, E. Stamatakis, N. Cerneaz, S. L. Kok, P. Taylor, D. Betal, J. Savage, The mammographic image analysis society digital mammogram database, In Proceedings of International Workshop on Digital Mammography, pp. 211-221,York, UK, 10-12 July 1994

[133] YA. Tolias, SM. Panas, A fuzzy vessel tracking algorithm for retinal images based on fuzzy clustering, IEEE Transactions on Medical Imaging , Vol. 17, No. 2, pp. 263-273, April 1998

[134] D-Y. Tsai, E. Matsuyama, H-M. Chen, Improving image quality in medical images using a combined method of undecimated wavelet transform and wavelet coefficient mapping, Vol. 2013, article id: 797924, 2013

[135] ED. Ubeyli, I. Guler, Automatic detection of erythemato-squamous diseases using adaptive neuro-fuzzy interference system, Computers in Biology and Medicine, Vol. 35, No.5, pp. 421-433, 2005.

[136] A. Unser, Splines: A perfect fit for signal and image processing, IEEE Signal Processing Magazine, Vol.16, No.6, pp. 22–38, November 1999

[137] M. Unser, Ten good reasons for using spline wavelets, In Proceedings of SPIE Conference Wavelet Applications in Signal and Image Processing V, Vol. Proc. SPIE 3169, pp. 422-431. San Diego, CA, 6-9 August 1997.

[138] D. Usher, M. Dumskyj, M. Himaga, T.H. Williamson, S. Nussey, J. Boyce, Automated detection of diabetic retinopathy in digital retinal images: a tool for diabetic retinopathy screening, Diabetic Medicine, Vol. 21, No. 1, pp. 84-90, 2004

[139] R. P. Walvick, K. Patel, S. V. Patwardhan, A. P. Dhawan, Classification of melanoma using wavelet-transform-based optimal feature set, In Proceedings of SPIE 5370, Medical Imaging 2004: Image processing, 944, San Diego, CA, May 12, 2004, doi:10.1117/12.536013

[140] C. T. Wang, B. N. Karayiannis, Detection of microcalcification in digital mammograms using wavelets, IEEE Transactions on Medical Imaging, Vol 17, No. 4, pp. 498-509, 1998.

[141] R. Willett and R. Nowak, Platelets: a multiscale approach for recovering edges and surfaces in photon limited medical imaging, IEEE Transactions on Medical Imaging, Vol. 22, No. 3, pp. 332-350, March 2003

[142] R.M. Willett and R. D. Nowak, Platelets for multiscale analysis in medical imaging, In Proceedings of 24th Annual Conference and the Annual Fall Meeting of the Biomedical Engineering Society EMBS/BMES Conference, Vol.2, pp.1023-1024, 2002

[143] S. Yang, Y. Lu, M. Wang, L. Jiao, Low bit rate SAR image coding based on adaptive multiscale bandlets and cooperative decision, Signal Processing, Vol.89, No.10, pp. 1910-1920, 2009

[144] L. Ying, L. Demanet, E. J. Candes, 3D Discrete Curvelet Transform, In SPIE, Vol. 5914, pp.351-361, 2005

[145] G. Zahlmann, B. Kochner, I. Ugi, D. Schuhmann, B. Liesenfield, A. Wegner, M. Obermaier, M. Metrz, Hybrid fuzzy image processing for situation assessment, IEEE in Medicine and Biology, Vol.19, No.1, pp. 76–83, 2000

[146] F. Zana, and J–C. Klein, Segmentation of vessel-like patterns using mathematical morphology and curvature evaluation, IEEE Transactions on Image Processing, Vol. 10, No. 7, pp. 1010-1019, July 2001

[147] B. Zhang, L. Zhang, L. Zhang, F. Karray, Retinal vessel extraction by matched filter with first order derivative of Gaussian, Computers in Biology and Medicine, Vol. 40, pp.438-445, April 2010

[148] G. Zhao, A. Hadid, M. M. Pietikäinen, T. Ahonen, Computer vision using local binary pattern, Computational Imaging and Vision 40, Springer-Verlag London Limited, 2011.